Development of a Microphysiological Model of the Kidney Proximal Tubule and Application in Predictive Toxicity Testing of Polymyxin Antibiotics

Elijah J. Weber

A dissertation

submitted in partial fulfillment of the

requirements for the degree of

Doctor of Philosophy

University of Washington

2018

Reading Committee:

Edward J. Kelly, Chair

Terrance J. Kavanagh

Benjamin Freedman

Program Authorized to Offer Degree:

Pharmaceutics

University of Washington

Abstract

Development of a Microphysiological Model of the Kidney Proximal Tubule and Application in Predictive Toxicity Testing of Polymyxin Antibiotics

Elijah J. Weber

Chair of the Supervisory Committee:
Associate Professor Edward J. Kelly
Department of Pharmaceutics

Late-stage attrition of investigational new drugs can be extremely devastating to both the drug developer as well as the patient in regard to money lost and disease left untreated, respectively. A primary reason for a compound's development to be suspended, if not terminated, can be attributed to the preclinical underestimation of unforeseen toxic events surfacing in human subjects during clinical trials. Existing preclinical models that lack accuracy for predicting toxicity demonstrate the dire need for improving and developing more robust physiologically relevant models. Our goal was to develop an *ex vivo* 3D microphysiological system (MPS) capable of recapitulating, both structurally and functionally, the microenvironment of the kidney proximal tubule. Using the MPS, we have demonstrated native functions of the human proximal tubule including expression of appropriate marker proteins, biochemical and synthetic activities, as well as secretory and reabsorptive processes. Through concentrative facilitated transport, via secretory and reabsorptive processes, the renal proximal tubule becomes a primary site of drug accumulation and thus drug-induced injury. Our goal was to show that the MPS can now be an accurate preclinical model of nephrotoxicity. Using the

MPS, drug-induced nephrotoxicity and sensitivity to prototypical nephrotoxins was assessed using the classic and developing polymyxin antibiotics, Polymyxin B (PMB) and Northern Antibiotics-739/741 (NAB739/NAB741). Polymyxins are highly effective for treating gram-negative bacterial infections yet there remains a high frequency of nephrotoxicity (~30%) which has limited their applications in the clinic and deemed them a last-line therapeutic. Because current mechanisms of polymyxin-induced nephrotoxicity are unclear, we have used the MPS, coupled with global transcriptomics, to elucidate the underlying mechanisms. Furthermore, we have shown that polymyxin-derivatives (NAB739/741), containing a reduced polycationic nature compared to PMB, have markedly reduced indications of injury relative to polymyxin exposure. The experimental approach used was to model and establish a safety profile of polymyxin-induced nephrotoxicity, for both PMB and the NAB compounds, using the MPS via a multiplex assessment of cell-associated biomarker induction, urinary biomarkers induction, and the transcriptional response to exposure. Results of these studies will advance the development of innovative antibiotics and validate the utility of the 3D MPS as a platform for preclinical safety assessment of new molecular entities.

Table of Contents

List of Figures and Tables

Abbreviations

SLC: solute carrier transporter

OAT: organic anion transporter

OCT: organic cation transporter

OATP: organic anion transport polypeptide

MATE: multidrug and toxin extrusion protein

ABC: ATP-binding cassette

MDR: multidrug resistant protein

BCRP: breast cancer resistance protein

MRP: multidrug resistance associated protein

ROS: reactive oxygen species

MPS: microphysiological system

PMB: polymyxin B

PTECs: proximal tubule epithelial cells

NAB: Northern Antibiotics

SPR: Spero Therapeutics

CYPs: cytochrome P450

KIM-1: kidney injury molecule-1

HMOX1/HO-1: heme oxygenase-1

GGT: gamma glutamyl transpeptidase

SGLT2: sodium glucose cotransporter-2

2-NBDG: (2-deoxy-2-[7-nitro-2, 1, 3-benzoxadiazol-4-yl) amino]-D-glucose

PAH: paraaminohippurate

AKI: acute kidney injury

miR: micro RNA

CKD: chronic kidney disease

ESRD: end-stage renal disease

sCr: serum creatinine

BUN: blood urea nitrogen

IL-18: interleukin 18

NGAL: neutrophil gelatinase-associated lipocalin

L-FABP: liver-type fatty acid-binding protein

MIOX: myo-inositol oxygenase

TIMP-2: tissue inhibitor of metalloproteinase 2

IGFBP7: insulin-like growth factor binding protein 7

Acknowledgements

I would like to acknowledge and thank Dr. Edward Kelly for continually pushing me to think critically while fostering and supporting my passions in the lab. I would also like to thank Dr. Jonathan Himmelfarb and the doctoral thesis committee of Drs. Danny Shen, Terrance Kavanagh, and Benjamin Freedman for their invaluable expertise and guidance throughout the development of the doctoral thesis. Lastly, I would like to thank my friends, family, and colleagues for their continued support and motivation throughout this journey.

Dedication

The work in this dissertation is dedicated to every preclinical test model that has been used to advance the understanding of newly developed compounds in the human body. With every experiment, we further our learning and move closer to test systems that are more sensitive than the previous, ultimately preserving life.

Chapter 1

Introduction: Renal proximal tubule and polymyxin B exposure

Some parts of the work presented in this chapter was published:

Clin Pharmacol Ther. 2016 Nov; 100(5): 464–478.

DOI: http://dx.doi.org/ 10.1002/cpt.436

1.1 Introduction: Renal Nephron Microenvironment – Proximal Tubule

The nephron is the functional unit of the kidney responsible for maintaining both the homeostasis of electrolytes as well as fluid volume(*1*). However, from a drug-development perspective the nephron is the primary site of renal handling involving any combination of filtration and phase III mediated-secretion/reabsorption. Structurally, the nephron is a series of segmented tubules that individually play a critical role in its overall function. The proximal tubule, found in juxtaposition to the glomerulus, has been shown to be the primary site of transport-mediated reabsorption/secretion xenobiotics. Active vectorial transport of xenobiotics are achieved given the polarized configuration of the proximal tubule epithelial cells involving both transporters found on the brush-border containing apical side (facing urine) and the basolateral side (facing systemic circulation) (Figure 1.1: modified from Figure 1(*2*)).

1.1.1 Basolateral Transporters:

The solute carrier (SLC) transporters are the major family of multi-specific transporters that mediate the proximal tubule uptake of both xenobiotic and endogenous substrates that are circulating within the blood. SLC transporters include the Organic Anion Transporters (OAT1/2/3), Organic Cation Transporters (OCT2/3), and the Organic Anion Transporter Polypeptide (OATP4C1).

1.1.2 Apical Efflux Transporters:

The SLC transporters are also found on the apical side of the proximal tubule and are responsible for the removal of exogenous and endogenous substrates that have accumulated within the cell via diffusion, reabsorption, and/or uptake from the circulatory side. SLC transporters found on the apical side of the proximal tubule include the Organic Anion Transporter (OAT4), Multidrug

and Toxin Extrusion Protein (MATE1/2-K), Urate Anion Exchanger (URAT1), and Organic Cation/Carnitine Transporter (OCTN1/2). Additionally, another superfamily of multispecific transporters found on the apical side includes the ATP-binding cassette (ABC) transporters, which use ATP hydrolysis to drive molecules across cell membranes. The ABC transporters on the apical side include Multidrug Resistance Protein (MDR1 or Pgp), Breast Cancer Resistance Protein (BCRP), and Multidrug Resistance Associated Protein (MRP2/4).

1.2 Proximal Tubule Transport Model – Historical perspective and current status.

In recent studies, there has been a vast improvement of the modeling capabilities of xenobiotic transport using models and cell types that accurately recapitulate human physiology. Traditionally, researchers have used established immortalized cell lines from animals, including canine (MDCK), opossum (OK), and porcine cells (LLC-PK1), as a cell source to optimize models(*3-5*). Transwell studies, using cells grown in monolayers on a permeable scaffold, are utilized to investigate the facilitated transport from one compartment to the other resembling the apical-basolateral relationship seen *in vivo*(*6*).

While established immortalized cell lines have remained as the gold standard for *in vitro* transport studies, there are drawbacks associated with their use, particularly the poor expression and/or absence of human-specific transporters (*7*). To combat this problem, investigators have used molecular techniques to transfect the established animal cell lines with specific human transporters(*8*). Additionally, investigators have immortalized primary renal cortex cells from human kidney (HK-2) and have shown that not only do they retain proximal tubule cell phenotypes; they also possess the functional aspect of transport and sensitivity to toxin(*9*). However, as demands increase to resemble the *in vivo* phenotype to its highest extent, there are

shortcomings with the immortalized human cell lines that research groups have addressed(*10*). As models continue to become more advanced, there has been a widespread shift from immortalized cells to primary renal cells to more accurately represent the native *in vivo* microenvironment(*11*). Brown et al. has shown, using primary human proximal tubule cells grown on permeable filter supports, differentiated cells expressing a wide array of transporters as well as functional transport activity of OAT1/3, MRP2/4, OCT2, MDR1, and MRP2 (*12*).

1.3 Polymyxin Nephrotoxicity

Stemming from the discovery of the first antimicrobial therapeutic in the early 1900s, antibiotics have vastly improved human health. While this improvement to human health has been invaluable, the misuse of these "magic bullet" antibiotics have caused an emergence of multidrug-resistance (MDR) bacteria that have not only threatened patients, but puzzled clinicians and drug developers in regard to potential treatment options. Because of their ability to "escape" the lethal action of available antibiotics, the "ESKAPE" pathogens (*Enterococcus faecium, Staphylococcus aureus, Klebsiella pneumoniae, Acinetobacter baumanni, Pseudomonas aeruginosa,* and *Enterobacter species*) are reported to cause a majority of infection in hospitals in both the developed and developing world (*13*). To address "ESKAPE" pathogens on the influence of the antibiotic pipeline, the Infectious Diseases Society of America (IDSA) has released multiple reports aiming to create a sustainable research and development infrastructure that can respond to current antimicrobial resistance and anticipate evolving resistance. While efforts continue to raise awareness, progress in the clinic has been slow, with the approval of only 2 antibacterials since the last IDSA report in 2009 (*14, 15*). The war against resistance is evidenced by a lack of therapeutic innovation and increasing mortality rates. According to a report in 2013 from the Centers for Disease Control and Prevention, at least 2 million Americans

each year become infected with antibiotic resistant bacteria and at least 23,000 people die each year as a direct result of these infections. Furthermore, in 2014 the World Health Organization incorporated data from 114 countries and released its first global report on antibiotic resistance. This comprehensive report revealed the true potential of a global health crisis and called for a harmonized urgency amongst the community, healthcare professionals, and industry policymakers. To combat resistance, the report particularly identified a push towards innovative research and development of novel tools.

1.3.1 Evidence of polymyxin-induced nephrotoxicity

In response to the rising development of antibiotic resistant bacterial strains, there have been increasing efforts toward improving existing antibiotics to combat multidrug-resistance. The rationale behind these efforts is driven in part by the cost and difficulty of identifying novel antibiotic classes, although emerging technologies may prove useful(*16*). Of the known antibiotics drug developers are refining, the polymyxins are of particular interest. Specifically targeting gram-negative bacilli, the two clinically used polymyxins, polymyxin B (PMB) and colistin (polymyxin E), are cyclic polycationic decapeptides that contain a heptapeptide ring, a linear tripeptide portion, and a fatty acyl tail bound to the N-terminus of the linear peptide portion (*17*, *18*). In a global assessment of antimicrobial activity against approximately 55,000 clinical isolates of gram-negative bacilli (year 2001 – 2004), PMB displayed excellent potency against “ESKAPE” pathogens with low resistance rates ranging from 3% or less around the world (*19*). Despite these positive findings, their uses in the clinics have remained as a last resort against MDR bacilli due to the numerous reports of primarily dose-limiting nephrotoxicity and less frequent neurotoxicity. From a retrospective analysis (year 1999 – 2000) by Ouderkirk et al., the authors observed a 14% incidence of polymyxin-induced renal failure accompanied with a

20% mortality rate and 88% microbiologically cure rate in the 60 patients being treated for nosocomial gram-negative infections(*20*). Additionally, a retrospective analysis (year 2001 – 2007) by Mostardeiro et al., showed that while 92 patients were 100% microbiologically cured, the nephrotoxicity rate was 32.6% and that there was a statistically significant association between duration of polymyxin exposure and renal impairment (defined by a serum creatinine levels exceeding 2 mg/dl (healthy individual range 0.7-1.2 mg/dl))(*21*). While there is a clear observation of polymyxin-induced nephrotoxicity in the clinic, pharmacological understanding of the mechanism still remains unknown.

1.3.2 Traditional models of polymyxin-induced nephrotoxicity

Historically, polymyxin-induced nephrotoxicity has been investigated using traditional toxicological approaches and techniques utilizing immortalized cell lines and animal models. Neiva et al. used LLCPK-1 cells, immortalized porcine proximal tubule epithelial cells, to characterize polymyxin B and observed a time (24, 48, 72 h) and dose (0, 75, 375 μM) dependent association with cytotoxicity, particularly through apoptotic activation (*22*). Additionally, Azad et al. has demonstrated polymyxin-induced nephrotoxicity using NRK-52E cells, immortalized rat proximal tubule epithelial cells, and observed apoptotic activation, via caspase stimulation, mitochondrial fragmentation, and mitochondrial membrane potential loss, in a dose-dependent (0, 1, 2 mM) manner(*23*). Polymyxin-induced nephrotoxicity has also been demonstrated using animal models. Dai et al. investigated the nephrotoxic potential of colistin in mice using both biochemical analyses of injury biomarkers and apoptotic activation. The group observed, over 7 days of 7.5 or 15 mg/kg/day administration, significant histological renal injury in a dose-dependent manner as well as dose-dependent biomarker injury response(*24*). In addition to mice, Magee et al. investigated novel polymyxin analogues in rats and dogs. The research group

showed the novel polymyxin analogues ability to retain *in vitro* potency against gram-negative bacilli while at the same time reporting a lower incidence of forming necrotic kidney lesions. Surprisingly, the group revealed species-specific sensitivity to polymyxin exposure, particularly in dogs relative to rats. A polymyxin derivative, 5x, showed a favorable safety profile *in vitro* yet poor translation from *in vivo* safety studies in dogs while being well tolerated in the rat(*25*). Preclinical models have sufficiently observed polymyxin-induced nephrotoxicity; however, physiological species-relevant 3D systems can improve *in vitro - in vivo* predictions as well as aid in toxicological understanding(*26*).

1.4 Hypothesis and Specific Aims

Hypothesis 1: Mitochondrial membrane destabilization induces apoptosis via ROS formation from PMB exposure.

Aim 1.1: Establish the dose-response relationships of PMB-induced nephrotoxicity.

Aim 1.2: Determine the ROS species and subcellular production sites induced by PMB exposure.

Aim 1.3: Measure transcriptional changes as a means to define the adverse outcomes pathways associated with PMB-induced apoptosis.

Hypothesis 2: Polycationic properties of polymyxins are responsible for their induced-nephrotoxicity.

Aim 2.1: Identify dose response relationship of NAB-induced nephrotoxicity relative to polymyxin toxicity.

Aim 2.2: Measure transcriptional changes associated with NAB exposure for comparative adverse outcome pathways identification in response to polymyxin toxicity.

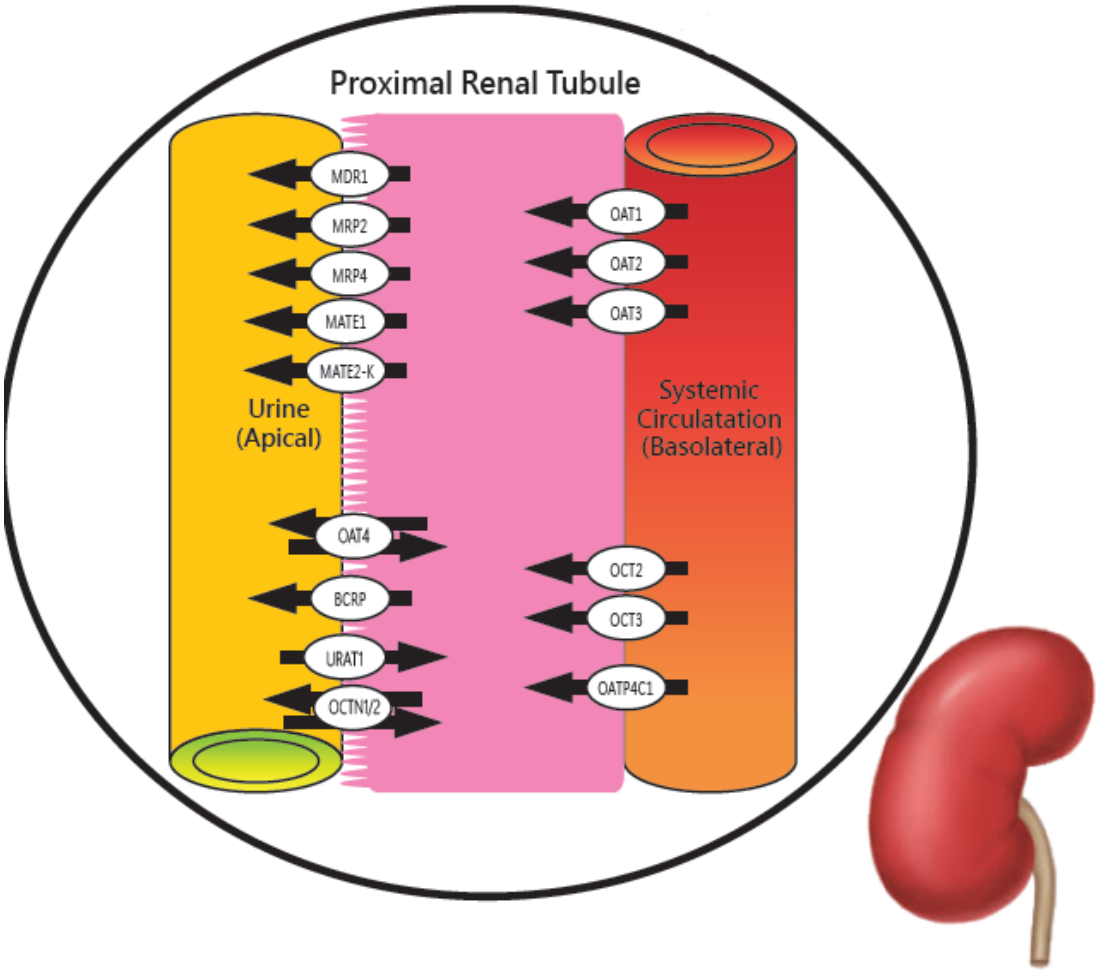

Figure 1.1 - Renal Transporters.

Graphic illustration of the relationship between subcellular localization of transporters in the kidney as well as the preferential flux directionality for each individual transporter (arrows).

Chapter 2

Development of a Microphysiological Model of Human Kidney Proximal Tubule Function

The work presented in this chapter was published:

Kidney International 2016, Volume 90, Issue 3, 627 - 637

DOI: http://dx.doi.org/10.1016/j.kint.2016.06.011

Development of a microphysiological model of human kidney proximal tubule function

Elijah J. Weber[1,7], Alenka Chapron [1,7], Brian D. Chapron [1,7], Jenna L. Voellinger[1], Kevin A. Lidberg[1], Catherine K. Yeung [2,6], Zhican Wang [1,8], Yoshiyuki Yamaura [1,9], Dale W. Hailey[3], Thomas Neumann[4], Danny D. Shen [1,2], Kenneth E. Thummel[1], Kimberly A. Muczynski[5], Jonathan Himmelfarb [5,6] and Edward J. Kelly[1]

[1]Department of Pharmaceutics, University of Washington, Seattle, Washington, USA; [2]Department of Pharmacy, University of Washington, Seattle, Washington, USA; [3]Department of Biological Structure, University of Washington, Seattle, Washington, USA; [4]Nortis Inc., Seattle, Washington, USA; [5]Department of Medicine, University of Washington, Seattle, Washington, USA; and [6]Kidney Research Institute, University of Washington, Seattle, Washington, USA

Correspondence: Edward J. Kelly, 1959 NE Pacific Street, HSB Room H272, Seattle, WA 98195, USA. E-mail: edkelly@uw.edu ; or Jonathan Himmelfarb, 325 Ninth Avenue, Seattle, WA 98104, USA. E-mail: himmej@u.washington.edu

[7]EJW, AC, and BDC contributed equally to this work.
[8]Current address: Amgen Inc., South San Francisco, California, USA.
[9]Current address: Ono Pharmaceutical Co. Ltd., Chuo-ku, Osaka, Japan.

Received 21 October 2015; revised 31 May 2016; accepted 2 June 2016

2.1 Abstract

The kidney proximal tubule is the primary site in the nephron for excretion of waste products through a combination of active uptake and secretory processes and is also a primary target of drug-induced nephrotoxicity. Here, we describe the development and functional characterization of a 3-dimensional flow-directed human kidney proximal tubule microphysiological system. The system replicates the polarity of the proximal tubule, expresses appropriate marker proteins, exhibits biochemical and synthetic activities, as well as secretory and reabsorptive processes associated with proximal tubule function *in vivo*. This microphysiological system can serve as an ideal platform for *ex vivo* modeling of renal drug clearance and drug-induced nephrotoxicity. Additionally, this novel system can be used for preclinical screening of new chemical compounds prior to initiating human clinical trials.

2.2 Introduction

Several publicly funded initiatives now seek to drive the development of innovative, human cell-derived preclinical models that would accelerate the drug development process, shorten the time it takes to move a new molecular entity into early clinical trials, and reduce the excessively high failure rate of clinical trials. Our goal is to apply flow directed microphysiological technologies to model the physiological functions of the human kidney proximal tubule, as it plays a vital role in active secretory and reabsorptive transport of drug molecules and is a primary site of drug-induced nephrotoxicity due to these concentrative processes (*27*). Whereas existing cell culture and animal models of proximal tubular function have utility, there are serious limitations stemming from functional deficits of conventional cell culture systems and differing physiology between animal models and humans.

In this report, we describe the development of a 3-dimensional (3D) microphysiological system (MPS) of the human proximal tubule. The kidney tubule MPS exhibits long-term viability, retains polarized expression and function of proteins essential for reabsorptive and secretory transport, responds to physiological stimuli, and performs critical biochemical synthetic activities.

2.3 Materials and Methods

2.3.1 Cell Isolation, Culture, and Seeding in MPS Platform

Human kidney tissue was obtained from specimens obtained during surgical resection of renal cell carcinoma performed at the University of Washington Medical Center. The human subject protocol was approved by the University of Washington Institutional Review Board. Healthy portions of the surgical specimen were dissected, stored at 4 °C in Hanks balanced salt solution buffer containing penicillin-streptomycin, and processed for isolation of proximal tubule epithelial cells within 24 hours as described previously (*28*). Cells with passage numbers 1 through 4 were used in the subsequent 3D culture experiments—please refer to Supplementary Figure S4 for consistency of morphological appearance of cells across donors and passage numbers. The 3D MPS platform used in these studies was developed by Nortis Inc. (Seattle, WA) and details of its construction have been reported by Tourovskaia et al (*29*). For cell seeding, MPS platforms were filled with ECM of 6 mg/ml rat tail collagen type I (Ibidi, Madison, WI) at 4 °C. MPS platforms were left for 30 minutes at 4 °C for matrix settling, and then stored at room temperature overnight. Microfibers inserts were removed from the device and the channel was coated with collagen type IV (5 mg/ml; BD Biosciences, Bedford, MA) over 1 hour. Confluent monolayer cultures of proximal tubule epithelial cells (PTECs) were treated with 0.05% Trypsin-ethylenediamine tetra-acetic acid to obtain single-cell suspensions.

PTECs were washed, counted, and resuspended at a concentration of 15 to 20 x 10^6 cells/ml and ~0.5 µl of cell suspension was injected into the collagen IV–coated lumen of the MPS. Cells adhered for 24 hours before initiating media flow at 0.5 ml/min. Cell coverage and integrity of the tubule structure were assessed under light microscopy on a weekly basis. Additionally, cell viability was assessed using a LIVE/DEAD Viability/Cytotoxicity assay (Invitrogen, Carlsbad, CA). For all of the experiments conducted, MPS platforms contained PTECs grown for 2 to 3 weeks after initial cell seeding.

2.3.2 Immunocytochemistry and Imaging

Proximal tubule epithelial cells in MPS platforms were fixed with 10% Buffered Formalin Acetate (Fisher Scientific, Pittsburg, PA) for 1 hour, permeabilized with 0.5% Triton X-100 (Sigma-Aldrich, St. Louis, MO), and blocked with 0.1% bovine serum albumin for 40 minutes. Primary antibodies were then applied overnight at 4 °C and fluorescently labeled secondary antibodies were applied for 1 hour at room temperature. Cells were mounted using SlowFade gold (Invitrogen, Carlsbad, CA) medium. Phase contrast and fluorescent images were acquired as described in Supplementary Materials and Methods. For analysis of MPS ultrastructure by transmission electron microscopy, devices were fixed in 1/2 Karnovsky fixative (2.5% glutaraldehyde with 2% formaldehyde in 0.1 M buffer). Samples were postfixed in osmium tetroxide and processed, sectioned, and examined according to protocols described previously (*30*).

2.3.3 GGT Activity

The presence and functioning of GGT was demonstrated by metabolism of GSSG or the oxidized form of glutathione in MPS cultured with PTECs grown to >50% confluency. To test for GGT

activity, proximal tubule MPSs were perfused with culture media at 1 µl/min containing 4 µM of GSSG; effluent samples were collected at hourly intervals for a total of 4 hours. After the first phase of collection, the platforms were perfused overnight using fresh media to ensure sufficient washout of GSSG. To verify specificity of GSSG processing by GGT, platforms were re-perfused with 4 µM GSSG in the presence of GGT inhibitor–acivicin (1 µM), and effluent samples were collected hourly for a total of 4 hours. GSSG concentration in the effluent perfusate was measured by liquid chromatography–tandem mass spectrometry (LC-MS/MS). Results are presented as recovery of GSSG expressed as a percentage of nominal input in the presence and absence of GGT inhibitor. Additional analytical details are presented in Supplementary Materials and Methods.

2.3.4 ATP assay

Generation of ATP via cellular respiration by PTECs was tested. MPS-cultured PTECs were treated with 1 µM antimycin A (Abcam, Cambridge, MA) or 0.01% dimethylsulfoxide for 24 hours followed by measurement of ATP using a luminescent ATP detection kit (Abcam) with slight modification. Briefly, cells were removed from the devices by injecting approximately 50 ml of detergent (Abcam luminescent kit, part 8206000) into the injection port allowing cells to be collected at the luminal outflow port. Cell lysates were transferred to a white opaque 96-well plate (Corning Costar, Corning, NY) to complete the kit procedure and luminescence was quantified using a PlateLumino luminometer (Stratec Biomedical Systems AG, Gewerbestr, Germany). A 5-point ATP standard curve (10 µM – 1 mM) was generated and used to convert relative luminescence units to ATP concentration.

2.3.5 Ammoniagenesis

The ability to secrete ammonia in response to acidification was evaluated in MPS platforms cultured with PTECs grown to >50% confluency. The MPSs were initially perfused with phosphate-buffered saline (pH 7.4) at a flow rate of 1 ml/min for 4 hours; effluent was collected at 2-hour intervals. After 4 hours, the perfusate was switched to phosphate-buffered saline buffered to an acidic pH of 6.9, and 2-hourly collection of effluent was continued for another 4 hours. Samples at hour 4 were analyzed for ammonia concentration using a colorimetric ammonia assay kit (Abcam). Effluent ammonia concentrations at acidic and physiological pH conditions were compared.

2.3.6 Glucose reabsorption

Glucose reabsorption via SGLT2 was demonstrated in the MPS. Platforms were perfused with media for at least 2 weeks prior to being tested for glucose reabsorption. Glucose uptake was assessed using a fluorescent glucose analog 2-NBDG (2-deoxy-2-[7-nitro-2, 1, 3-benzoxadiazol-4-yl) amino]-D-glucose; Cayman Chemicals, Ann Arbor, MI). Twelve hours prior to testing, PTEC perfusion was switched to culture media with a lower, physiological glucose concentration (100 mg/dl). After 12 hours of pretreatment, MPS platforms were perfused with media containing 200 mg/ml (0.6 mM) of 2-NBDG either in the absence or presence of inhibitors apigenin (50 µM) or dapagliflozin (0.5 µM) for 2 hours at 37 °C. Platforms were then washed and imaged using a Nikon Eclipse Ti-S (Tokyo, Japan) and inverted spinning disk microscope in phase contrast and fluorescent modes and fluorescent signal quantified using ImageJ software (National Institutes of Health, Bethesda, MD).

2.3.7 25-$(OH)_2$ Vitamin D_3 metabolism

Conversion of 25-OH vitamin D_3 to its physiologically active and inactive metabolites was assessed in the MPS. Cells cultured from 3 separate donors were evaluated in triplicate for a total of 9 MPS platforms. PTECs were cultured for 2 to 3 weeks prior to the addition of 1 µM 25-OH vitamin D_3 (Toronto Research Chemicals, Toronto, Canada) to the cell culture media containing 2% fetal bovine serum to minimize adsorption of vitamin D_3 metabolites. Inflow rate of 25-OH vitamin D_3-containing media was set at 0.5 ml/ min and outflow was collected daily for 3 days and stored at -80 °C. LC-MS/MS analysis of 25-OH vitamin D_3 and its primary metabolites was conducted using a previously established method14 with modifications described in the Supplementary Materials and Methods. Formation clearance for the 3 dihydroxy-vitamin D_3 metabolites (1α,25-$(OH)_2$ vitamin D_3, 4β,25-(OH)2 vitamin D_3, and 24,25-(OH)2 vitamin D_3) was plotted over time. The method for calculating the formation clearance is described in Supplementary Materials and Methods.

2.3.8 Vitamin D receptor-mediated regulation

To evaluate the inductive effects of 1α,25-$(OH)_2$ vitamin D_3 (calcitriol) on the 24-hydroxylation of 25-OH vitamin D_3 (calcidiol), a group of MPS devices (n = 5) were exposed to 1 µM calcidiol in the presence or absence of 0.5 µM exogenous calcitriol. Effluent was collected for 3 days and stored at -80 °C until LC-MS/MS analysis of 24,25-$(OH)_2$ vitamin D_3 and calcidiol concentrations. Following treatment, RNA was extracted using Tri-reagent. In order to assess the more rapid effects of calcitriol co-administration on gene expression, additional MPSs were treated for 5 hours prior to collection in Tri-reagent. Total RNA was reverse transcribed to cDNA using reverse transcription kit (Life Technologies, Carlsbad, CA). Assessment of the

effects of calcitriol on the expression of genes relevant to calcidiol metabolism (CYP24A1, CYP27B1, and vitamin D receptor) was conducted using TaqMan Gene expression assays (Life Technologies) on a CFX Connect Real-Time PCR Detection System (Bio-Rad Laboratories, Hercules, CA). Relative quantification of mRNA was determined using glyceraldehyde-3-phosphate dehydrogenase as the housekeeping gene.

2.3.9 Secretory transport of organic solutes

Secretory transport of solutes was assessed using dual-channel MPS platforms as depicted in Supplementary Figure S3; 1 channel was populated with PTECs with an average of 85% confluent cell coverage, the other channel remained cell-free and served as a pseudo-vascular channel for delivery of substrates to the basolateral aspect of the tubular epithelium. Substrate solute was added to the media flowing through the cell-free channel. Competitive inhibitors were introduced into the media flowing through both channels. The rate of flow through both channels was set at 1 µl/min. Effluent from both channels was collected hourly. To assess secretory transport of PAH, 1 µCi/ml ^{14}C-PAH or 2 µM equivalent of PAH or 10 µM indoxyl sulfate (Sigma-Aldrich, St. Louis, MO) was introduced into the cell-free channel. Appearance of solute in the PTEC channel effluent was measured in the presence or absence of 2 mM probenecid. Interaction in secretory transport between PAH and indoxyl sulfate was assessed by examining 1 µCi/mL ^{14}C-PAH transport in the presence of 2 µM indoxyl sulfate. The appearance of radiolabeled PAH in the effluent was measured by liquid scintillation counting. Concentration of indoxyl sulfate in the effluent was measured by a previously established LC-MS assay with modifications (*31*). Details on the LC-MS assay are presented in Supplementary Materials and Methods. The MPS experiments depicted in Figures 2.8b, 2.9a, and 2.9b used 9, 8, and 7 MPSs, respectively. A minimum of 3 MPSs were assigned to each inhibitor treatment and control group.

Hourly time points were aggregated and presented as a mean ratio of the amount of test substrate appearing in the PTEC channel effluent relative to its nominal input amount into basolateral channel inhibitor. Error bars reflect the SEM of the aggregated time points for each experiment. For comparative purposes, transport of PAH was measured in Transwell as described elsewhere (*32*). Details on the protocol and modifications are available in Supplementary Materials and Methods.

2.3.10 Statistical Analysis

Data are reported as means ± standard errors. For comparison of means, statistical tests were applied using GraphPad software (La Jolla, CA).

2.4 Results

2.4.1 Structural Recapitulation of the Proximal Tubule Microenvironment.

The stepwise construction of a microphysiological model of human proximal tubule is presented in Figure 2.1ai to iv. Human primary proximal tubular epithelial cells (PTECs) were grown in monolayer cultures following isolation from renal cortical tissue. After about 7 days in culture, the cell monolayers displayed a uniform cobblestone-like appearance with dome formation that is characteristic of PTECs (Figure 2.1aii). (*8, 33*). Following seeding into the MPS, PTECs adhered to the channel surface and grew to form a tubule-like structure (Figure 2.1aiv); its physical dimension is close to that reported for the proximal portion of the renal tubule in the human kidney (i.e., 6 mm long x 120 mm thick in the MPS compared with 14 mm long x 40 mm thick *in vivo*). (*34*). In its present format, the MPS holds approximately 5000 PTECs. Microfluidic technology allowed media perfusion, which exposed PTECs to fluid shear force at the apical surface and delivered nutrients continuously under normoxic conditions (Figure 2.1aiii). (*29, 35*). PTEC in 3D culture exhibited excellent viability (>95%) for up to 4 weeks, as demonstrated by extensive green fluorescent calcein acetoxymethyl signal in live cells with minimal red fluorescent signal indicative of dead cells (Figure 2.1aiv). Cell surfaces showed fairly even expression of CD13 (aminopeptidase-N) and E-cadherin, markers of epithelial origin, for at least 28 days (Figure 2.1b B1 to B4). Proximal tubule origin of the final culture was verified by consistent immunohistochemistry staining for aquaporin-1 (Figure 2.1bB5 and B6) and lotus lectin (Supplementary Figure S1), whereas the signal for aquaporin-2, prominin 2, and uromodulin, markers of distal tubule or collecting duct cells or both, was absent in both 2-dimensional (2D) cultures and MPS (Supplementary Figure S1). It is interesting to note that KIM-1, a marker of acute kidney injury, is expressed in PTECs cultured in 2D, but is absent in

MPS devices (Supplementary Figure S1). This suggests that flow-directed culture coupled with 3D architecture confers a less injured, more quiescent phenotype within the MPS. Transmission electron microscopy images of PTEC ultrastructure showed representative density of mitochondria, Golgi apparatus, and rough endoplasmic reticulum. Tight junctions and short microvilli at the apical surface were also observed, as well as basolateral interdigitations between neighboring cells, the latter being characteristic of proximal tubules *in vivo* (Figure 2.2a1 and 2 and Supplementary Figure S2).(*36*). Polarization of PTECs was shown by localization of the tight junction protein ZO-1 to the luminal (apical) aspect of the PTEC tubule, and localization of Na^+/K^+–adenosine triphosphatase (ATPase) to the lateral interface between neighboring cells and the basal border between PTECs and collagen substrate (Figure 2.1c). Cilia formation in response to fluid shear stress was evidenced by positive staining of acetylated tubulin in rod-like structures that originate close to the cell nucleus; the ciliary process averaged 10 ± 3.5 μm in length (Figure 2.2b1 and 2).

2.4.2 Recapitulation of Proximal Tubule Physiological Functions.

Reclamation of glutathione is an essential biochemical function of renal proximal tubule *in vivo* (*11*). The reclamation process is mediated by g-glutamyl transpeptidase (GGT), which normally mediates the transfer of glutamyl moiety from glutathione to an acceptor amino acid as part of the g-glutamyl cycle, a pathway for the synthesis and degradation of glutathione. Selective immunohistochemistry staining for GGT in the MPS revealed enriched localization of the enzyme at the luminal aspect of the PTEC structure (Figure 2.3a). GGT mediates a comparable reaction for the oxidized form of glutathione, glutathione disulfide (GSSG) (Figure 2.3b) (*37*), which is a more chemically stable substrate for assessing the activity of g-glutamyl transpeptidase in proximal tubule MPS. PTECs within the MPS were perfused with media

containing 4 mM GSSG in the presence or absence of the irreversible GGT inhibitor acivicin (1 µM). The recovery of GSSG in the effluent was low (<1.5%), demonstrating extensive catalytic activity of GGT; in the presence of acivicin, an approximate 2- fold increase in GSSG recovery was observed over 2 to 4 hours (Figure 2.3c).

The proximal tubule is responsible for nearly 90% of glucose reabsorption in the kidney, which is mediated primarily by glucose transporters, including SGLT2 (*38*). Selective immunohistochemistry staining for SGLT2 in the proximal tubule revealed its expression and localization at the apical surface (Figure 2.4a). To confirm functioning of SGLT2 in the PTEC tubule microenvironment, glucose reabsorption was demonstrated by perfusing the proximal tubule in the MPS with a fluorescent glucose analog, 2-NBDG (200 mg/ml) in the presence or absence of either a SGLT2/glucose transporter inhibitor (apigenin 50 µM) or a SGLT2-specific inhibitor (dapagliflozin 0.5 µM). PTEC layer showed strong green fluorescent signal demonstrating avid cellular uptake and accumulation of 2-NBDG. Fluorescent signal intensity of 2-NBDG decreased significantly in the presence of both inhibitors, indicating blockade in uptake of the fluorescent glucose analog into epithelial cells (Figure 2.4b to f). It is worth noting that the magnitude of effect for both inhibitors (25% – 30%) is similar to the clinical efficacy of SGLT2 inhibitors (30% – 50%) despite *in vitro* predictions of 90% inhibition (*32*).

To demonstrate that the primary cells we use to populate the MPS generate their ATP energy source from mitochondrial oxidative phosphorylation as opposed to aerobic glycolysis (i.e., the Warburg effect) (*39*), we measured cellular ATP levels in the presence and absence of antimycin A. As seen in Figure 2.5, exposure to 1 µM antimycin A for 24 hours resulted in a 2-fold drop in ATP content. A similar magnitude decrease was also observed in PTECs cultured in monolayer (data not shown).

Renal proximal tubules respond *in vivo* to a drop in either blood or luminal filtrate pH with an increased generation and secretion of ammonia (Figure 2.6a). To demonstrate this physiological response, PTECs were exposed to a decrease in MPS luminal perfusate pH from 7.4 to 6.9. PTEC cells in the MPS responded with an approximate 3-fold increase in effluent ammonia concentration (pH 7.4–0.55 mM NH3, pH 6.9–1.56 mM NH3) (Figure 2.6b).

The proximal tubule epithelium is known to be a critical site for bioactivation of vitamin D. Systemically available 25-OH vitamin D3 (calcidiol) is converted to bioactive 1a,25-(OH)2 vitamin D3 (calcitriol) through the action of cytochrome P450 27B1 (CYP27B1). Metabolism of calcidiol to relatively inactive metabolites also occurs in the kidney via cytochrome P450 24A1 (CYP24A1). When seeded into the MPS, PTECs demonstrated the ability to metabolize calcidiol to quantifiable levels of bioactive calcitriol, inactive 24,25-(OH)2 vitamin D3 and 4b,25-(OH)2 vitamin D3 (Figure 2.7a) (*40*). Overall, the formation clearance (i.e., formation rate normalized by substrate concentration) for 24,25-(OH)2 vitamin D3 was significantly greater than that of calcitriol and 4b,25-(OH)2 vitamin D3. This finding is consistent with metabolism of calcidiol *in vivo*, where circulating concentrations of 24,25-(OH)2 vitamin D3 are known to be higher than those of both calcitriol and 4b,25-(OH)2 vitamin D3 (*41*). In order to further explore vitamin D homeostasis, MPS-seeded PTECs were challenged with additional exogenous calcitriol (500 nM), a vitamin D receptor ligand. Induction of the vitamin D receptor–regulated 24-hydroxylation pathway was observed (Figure 2.7b). This increase in 24,25-(OH)2 vitamin D3 formation was accompanied by a rapid (5 hours) and sustained (72 hours) accumulation of mRNA transcripts for CYP24A1 (Figure 2.7c). No apparent changes in gene expression of CYP27B1 (Figure 2.7d) or vitamin D receptor (Figure 2.7e) were observed.

2.4.3 Secretory Transport of Organic Solutes

Circulating organic solutes, including drugs and xenobiotics, can undergo secretion into the tubular lumen by means of active transport across the renal tubule epithelium. Secretory transport of the prototypical organic anion, paraaminohippurate (PAH) across PTEC monolayers was evaluated in both conventional Transwell (Corning Corp., Corning, NY) permeable cell culture inserts and the MPS, in the presence and absence of a competitive inhibitor, probenecid. No change in apparent permeability was observed in the 2D Transwell system upon addition of probenecid (Figure 2.8a). However, within the MPS the relative appearance of PAH in the effluent from the PTEC lumen was reduced approximately 4-fold in the presence of probenecid (Figure 8b). These data support the involvement of basolateral uptake (OAT1/3) or apical efflux (MRP2/4) transporters or both in the observed vectorial transport of PAH in the MPS (*42*). We further evaluated transport in the MPS using the endogenous anionic uremic solute, indoxyl sulfate (Figure 2.9a). As compared to PAH, indoxyl sulfate output in the PTEC channel effluent was approximately 20% lower but exhibited a similar degree of inhibition by probenecid. In addition, an interaction between PAH and indoxyl sulfate was demonstrated; coperfusion with indoxyl sulfate decreased secretory transport of PAH by 1.8-fold, suggesting a competition of the 2 solutes for the same organic anion transporters (Figure 2.9b).

2.5 Discussion

We have demonstrated that in a flow-directed MPS, human PTECs attach to supportive collagen extracellular matrix (ECM) and self-assemble to form a 3D tubular structure (*29, 35*). Furthermore, cells maintain renal epithelial differentiation and characteristic morphology in this microenvironment for an extended period of time. In contrast, PTECs grown in conventional 2D monolayer cultures often show limited longevity and loss of distinctive epithelial phenotype due to lack of fluidic mechanosensory input (*43*) and other stimulus elements present in the native microenvironment *in vivo*. Also, in contrast to conventional 2D culture, PTECs grown in the MPS polarize with proteins selectively localized to the basolateral and apical aspects of the tubular epithelium and exhibit expected morphological and functional phenotypes of proximal tubule epithelium *in vivo* out to 28+ days (*36, 44*).

We also demonstrated proximal tubular origin for the majority of epithelial cells in culture by immunohistochemistry staining of differential markers of kidney epithelial cells (viz., aquaporin 1, aquaporin 2, and SGLT2). Structurally, PTECs in the MPS exhibited polarized structure based on localization of domain-marker proteins. Assessment of ultrastructure by transmission electron microscopy revealed the hallmarks of a competent epithelial barrier, as well as healthy mitochondria and characteristic basolateral membrane interdigitations. The apical brush border expressed functionally active SGLT2 transporter (Figure 2.4) and GGT enzyme (Figure 2.3). Although brush border microvilli on the cultured PTECs were not as abundant as in freshly isolated cells (*29, 44*), this is consistent with literature reports of low microvilli density in traditional PTEC monolayer cultures (*33, 45*). Metabolic competence of the cultured PTECs was confirmed by their capability for ammoniagenesis and vitamin D biotransformation. In the case

of vitamin D, this metabolic competence was accompanied by retention of some of the machinery critical to maintaining vitamin D homeostasis *in vivo*.

The human kidney tubule MPS recapitulates the perfusion delivery and transport pathway of a secreted solute *in vivo* in that the test solute is perfused into a surrogate vascular channel, diffuses through the pseudo-interstitial space, and undergoes uptake and efflux across the epithelial barrier into the flowing perfusate in the tubular luminal channel. We demonstrated robust transepithelial transport of organic anionic (PAH, indoxyl sulfate) solutes that were sensitive to selective transport inhibitors. The results showed some inter-MPS and intra-MPS variability, which can be attributed to (i) interindividual variability in expression of proximal tubule transporters, and (ii) instability in effluent flow as a result of the porous and pliable collagen ECM. Nonetheless, the human proximal tubule MPS demonstrates applicability for assessing renal tubular secretion of drugs that was not observable using PTECs in a Transwell system. Our work lays a foundation for further investigation of the complex, coordinated uptake and efflux transport processes at the tubular epithelium.

A number of 3D tissue engineering models have been developed that attempt to mimic the proximal tubule structure and function (*11, 43, 46, 47*) (for reviews see Kelly et al. (*35*) and Kim and Takayama (*48*). A number of these systems utilize a monolayer of cells adhered to a microporous membrane coated with a thin layer of an ECM protein component, often collagen IV or laminin. The importance of 3D tubular architecture is reinforced by the observation that transplantation of 2D sheets of porcine renal proximal tubule cells onto dorsal subcutaneous tissue of nude rats results in increasingly complicated tubular structures with altered expression of surface markers as the 2D sheets convert to their native structure *in vivo* (*26*). It has become increasingly evident that the composition (*49*), microtopography (*50, 51*), and rigidity/elasticity

(*52*, *53*) of the ECM substrate on which a cell adheres can dictate the cells' morphology, phenotype, proliferation, and even fate. Unlike systems using microporous membranes, the tubular structures formed in our microphysiological system are surrounded by ECM whose composition and rigidity/elasticity can be modified to best recapitulate *in vivo*-like cellular function. Additionally, our microfluidic system enables coculture of a variety of cell types in the matrix compartment and the proximal tubule channel, permitting critical cell-cell and cell-matrix interactions, without interference from artificial scaffold materials.

The system described herein represents a milestone in cell culture modeling of human kidney in that it is possible to achieve a functional 3D construct of human proximal tubule *in vitro* in a microfluidic device that more faithfully reflects the native microenvironment of the renal tubulo-interstitium. There have been earlier attempts in recapitulating a functioning 3D proximal tubule. DesRochers et al. (*26*) constructed a static 3D culture of proximal tubular cells by culturing immortalized human renal cortical epithelial cells (NKi-2) suspended in an ECM consisting of a 50:50 mixture of rat tail collagen I and Matrigel (BD Bioscience, Billerica, MA). Maschmeyer et al. (*54*) cultured immortalized cell line renal proximal tubular epithelial cell/telomerase reverse transcriptase 1 (RPTEC/TERT-1) on a polyester track etched membrane within a 4-organ-chip device under continuous flow. Although longevity in culture and reproducible sourcing are practical advantages, the altered biology of immortalized cell lines is a serious drawback. The observation that the PTECs in our MPS self-assemble into 3D tubular structure may help to recapitulate proximal tubular functionality more effectively than previous monolayer or dispersed culture systems have done.

More recently, Jang et al. (*43*) reported development of a "kidney on a chip" with similar goals to our project. The MPS reported by Jang et al. (*43*) consisted of a PTEC epithelial monolayer

exposed to an apical fluid shear stress that was capable of reabsorbing glucose in the range of approximately 2% of the nominal input. Notably, our kidney tubule MPS achieves approximately 10-fold higher glucose reabsorption than that noted by Jang et al. (*43*) which is responsive to SGLT-2 specific inhibition and thus more closely replicates expected physiological functions. Efficient apical glucose uptake is among the key functions of proximal tubules *in vivo*. In addition, our proximal tubule MPS also exhibits organic solute transport functions that will permit its application in the study of renal drug clearance mechanisms. In contrast to the work of Jang et al. (*43*) we are also able to demonstrate physiologically regulated PTEC CYP-450 function in the biosynthesis of vitamin D sterols. Finally, our system demonstrates maintenance *in vitro* of an epithelial cell phenotype for up to 28 days, whereas the system employed by Jang et al. (*43*) was tested for only up to 4 days.

In pioneering work by Humes et al. (*11*) the development of a renal tubule assist device (RAD) also recapitulated multiple aspects of proximal tubular physiological function *ex vivo*. Similar to what we observe in our MPS, the RAD also demonstrated glucose reabsorption, glutathione metabolism, and PAH secretion (*11*). The RAD, as the name implies, was developed for the purpose of providing proximal tubule replacement therapy in the setting of kidney failure, whereas our kidney on a chip was designed for the specific purpose of improving the drug development as part of the National Institutes of Health Organs on Chips Consortium. Thus the RAD was designed to support renal function *in vivo* on a macroscale, whereas our MPS is primarily designed for predictive toxicity testing on a microscale. Given the divergent goals for development of the RAD and our proximal tubule on a chip, it is not surprising that each system has both comparative strengths and weaknesses. In the RAD system, media is perfused across a flat cell sheet in a 1-mm wide channel that attempts to mimic luminal shear stress. In contrast,

our microphysiological system enables the creation of a 120-μm diameter tubular tissue that is in direct contact with the surrounding 3D ECM, which more closely replicates human anatomy. Additionally species specificity for individual transporters may be a concern, given the use of primary porcine cells in the RAD device, although the RAD tested in clinical trials did make use of human cells (*12*). Because of the thickness of the hollow fiber dialysis membrane, the RAD may be less efficient for assessing basolateral secretory organic solute clearance, which is the major mechanism for proximal tubule drug and metabolite elimination. Conversely, because the hollow fiber design of the RAD allows facile abluminal flow and creation of an interstitial oncotic gradient favoring apical reabsorption, the RAD is superior to the current kidney on a chip design for detecting apical water and electrolyte reabsorption. Despite attempts to measure ion flux in our MPS using lithium as a marker of sodium transport in the presence and absence of inhibitors targeting either Na^+H^+ exchanger or Na^+K^+ ATPase, we were unable to recapitulate this function (data not shown). Although this is not a major limitation of the MPS for assessing organic drug elimination by the kidney as there is limited active apical reabsorption of organic xenobiotics, nonetheless we are currently developing a 2-channel microfluidic kidney MPS, with the second channel allowing a peritubular microvascular endothelial (*55*) to be grown within the matrix compartment. This design should provide a biomimetic for a more complex *in vivo*-like microenvironment that may facilitate assessment of electrolyte and water reabsorption in the proximal tubule. In addition, several studies have shown that coculturing endothelial cells with proximal tubule epithelial cells enhances *in vivo*-like epithelial function (*26*, *52*, *54*).

In summary, for the first time, we have a high-fidelity system *in vitro* that allows reliable investigation of the fundamental biology of the renal tubule epithelium; the potential applications include tubular secretion of drugs, xenobiotics, and uremic toxins, as well as the ability to assess

toxic injury response. To our knowledge, this is the first demonstration of a human proximal tubular cell *in vitro* system that can effectively model basolateral solute transport, apical solute uptake, and intracellular enzymatic function in a physiologically relevant manner. Moreover, our human kidney proximal tubule microphysiological system has the potential for integration of multiple cell types — epithelial cells, pericytes, and microvascular endothelial cells (*29*) — in a spatial alignment that would fully reconstitute a tubulointerstitial environment. In time, we envision the MPS will be extended to investigation into pathophysiological processes at the tubule-interstitium that underlie acute kidney injury and chronic kidney diseases, as well as transport and metabolic processes governing the renal handling of drugs and environmental toxicants in healthy and disease states.

2.6 Disclosure

All authors declared no competing interests.

2.7 Acknowledgements

We gratefully acknowledge Dr. Richard D. Palmiter for critical reading of the manuscript. We would like to acknowledge the technical assistance with LC-MS data acquisition from Brian Phillips at the University of Washington and Rick Newitt at the Kidney Research Institute. We would also like to acknowledge Julio Vazquez-Lopez from the Fred Hutchinson Cancer Research Center and Ron Seifert from the Institute for Stem Cell and Regenerative Medicine for the assistance with confocal microscope imaging. We are also grateful to Maria Lopez for her contribution with conducting experiments, and Catherine Lockhart for preparations of graphic illustrations in the manuscript. We would like to thank Kelly Hudkins for transmission electron microscopy processing of kidney MPS devices and Dr. H. Denny Liggitt for analysis and

interpretation of transmission electron microscopy images. Research reported in this publication was supported by the National Center for Advancing Translational Sciences of the National Institutes of Health under awards TL1TR000422 (BDC, JLV), KL2 TR000421 (CKY), and UH2/UH3 TR000504 (JH). This work was also supported in part by funding from the University of Washington Drug Metabolism, Transport, and Pharmacogenomic Research program (EJK). This research was also supported by an unrestricted gift from the Northwest Kidney Centers to the Kidney Research Institute. This publication was developed in part under Assistance Agreement 83573801 awarded by the U.S. Environmental Protection Agency to Elaine M. Faustman. It has not been formally reviewed by Environmental Protection Agency. The views expressed in this document are solely those of the authors and do not necessarily reflect those of the agency. The Environmental Protection Agency does not endorse any products or commercial services mentioned in this publication. CKY was supported by a grant from the Norman S. Coplon Extramural Grant Program by Satellite Healthcare, a not-for-profit renal care provider. AC was a recipient of the Warren G. Magnuson Scholarship at the University of Washington.

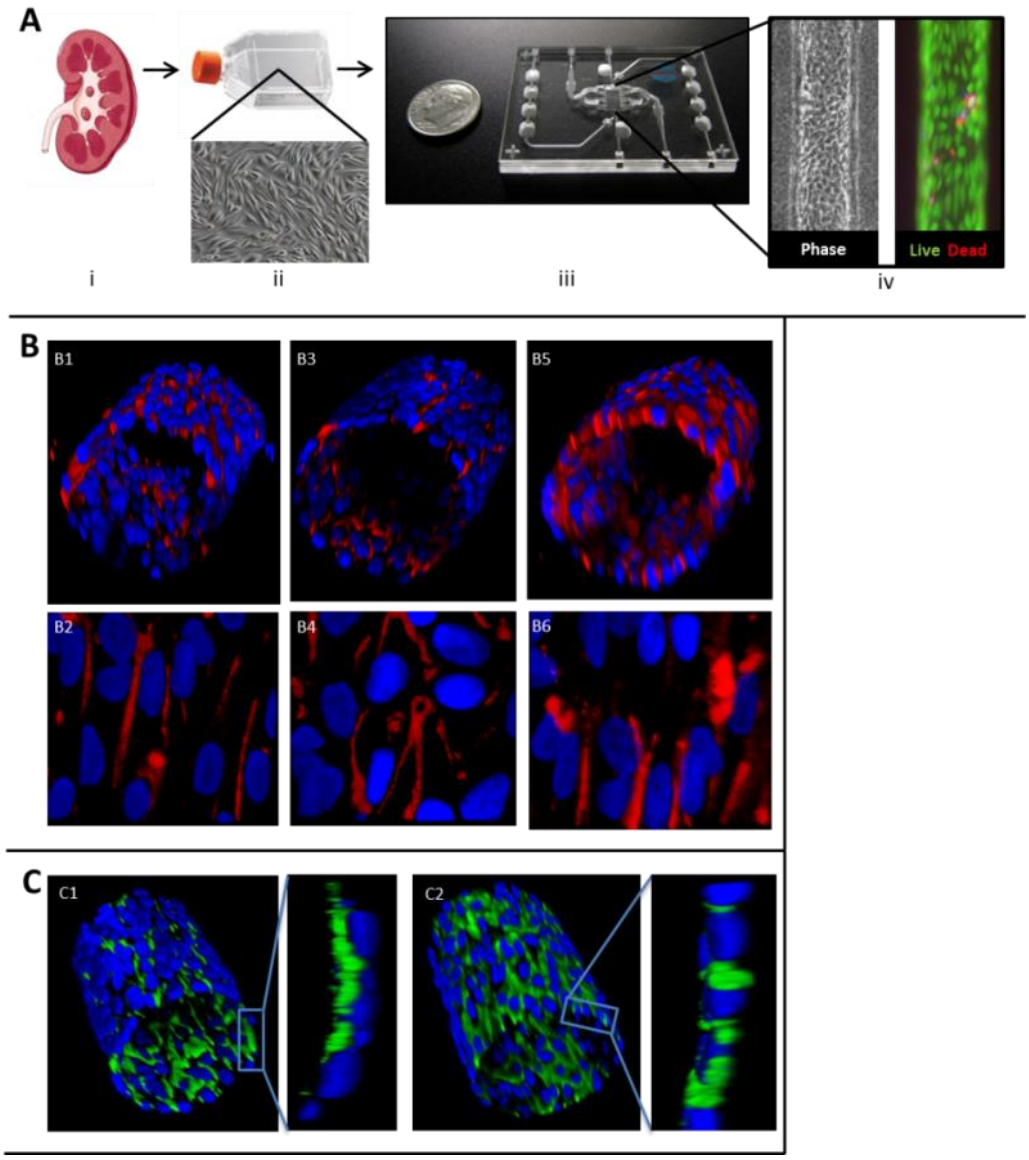

Figure 2.1 - PTEC viability and basic functionality in human kidney 3D MPS

(a) Scheme depicting construction of human proximal tubular epithelial cells (PTECs) in a microphysiological system (MPS). (A1) Cell isolation from human kidney cortex. (A2) Cell culture in 2 dimensions. (A3) Cell seeding and culture in 3-dimensional (3D) MPS. (A4) Phase contrast and viability of PTECs in MPS at day 28. (b) A 3D projection of MPS matrix shows PTEC tubule structure: (B1, 2) surface expression of epithelial cell marker CD13 (red) (original magnification x 400); (B3, 4) cell self-assembly confirmed by E-cadherin expression (red)

(original magnification x 400); (B5, 6) proximal tubule origin confirmed by expression of aquaporin 1 (red) (original magnification x 400). (c) Polarization confirmed by (C1) tight junction formation via apical localization of ZO-1 (green) and (C2) basolateral expression of Na+/K+ adenosine triphosphatase (green). Tubule diameter is ~120 µm. Bars = (aii) 200 µM; (aiv) 50 µM; (b,c) 20 µM.

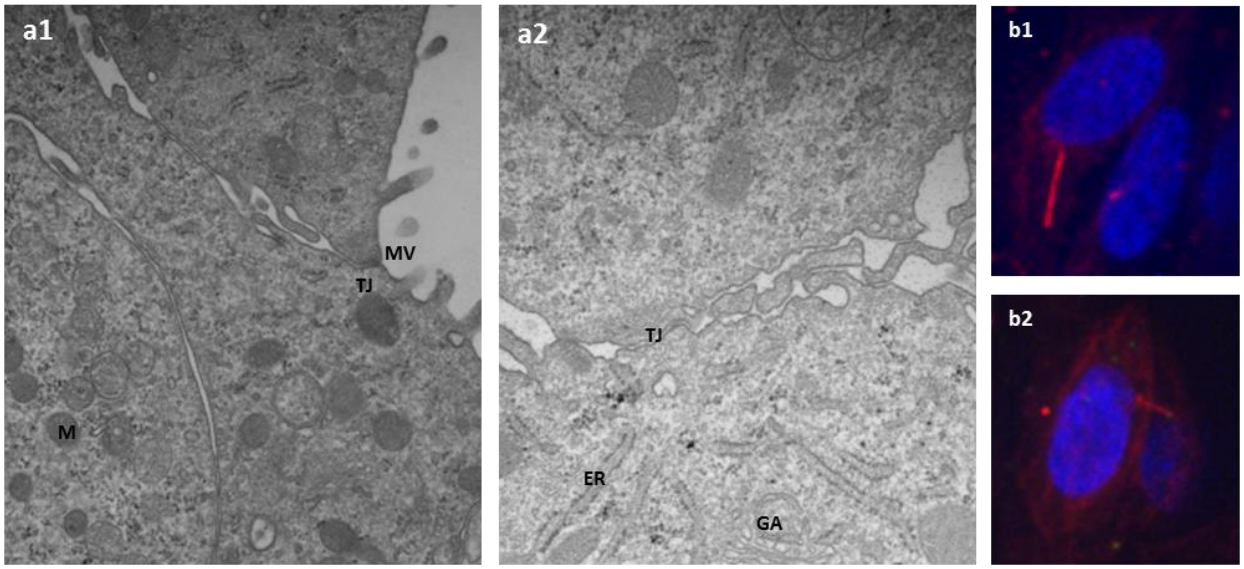

Figure 2.2 - Ultrastructure of human PTECs in human kidney 3D MPS.

(a1, 2) Transmission electron microscopy depicting ultrastructure of proximal tubular epithelial cells (PTECs) cultured in a microphysiological system (MPS) device. The following cellular structures are identified: microvilli (MV), mitochondria (M), tight junction (TJ), endoplasmic reticulum (ER), and Golgi apparatus (GA). Original magnifications (a1) x 10,000 and (a2) x 30,000. (b1, 2) PTECs in MPS form cilia as seen from 2 representative images of single cells stained for acetylated tubulin in red. Bars = (a1, 2) 500 nm and (b1) 5 µm). 3D, 3-dimensional.

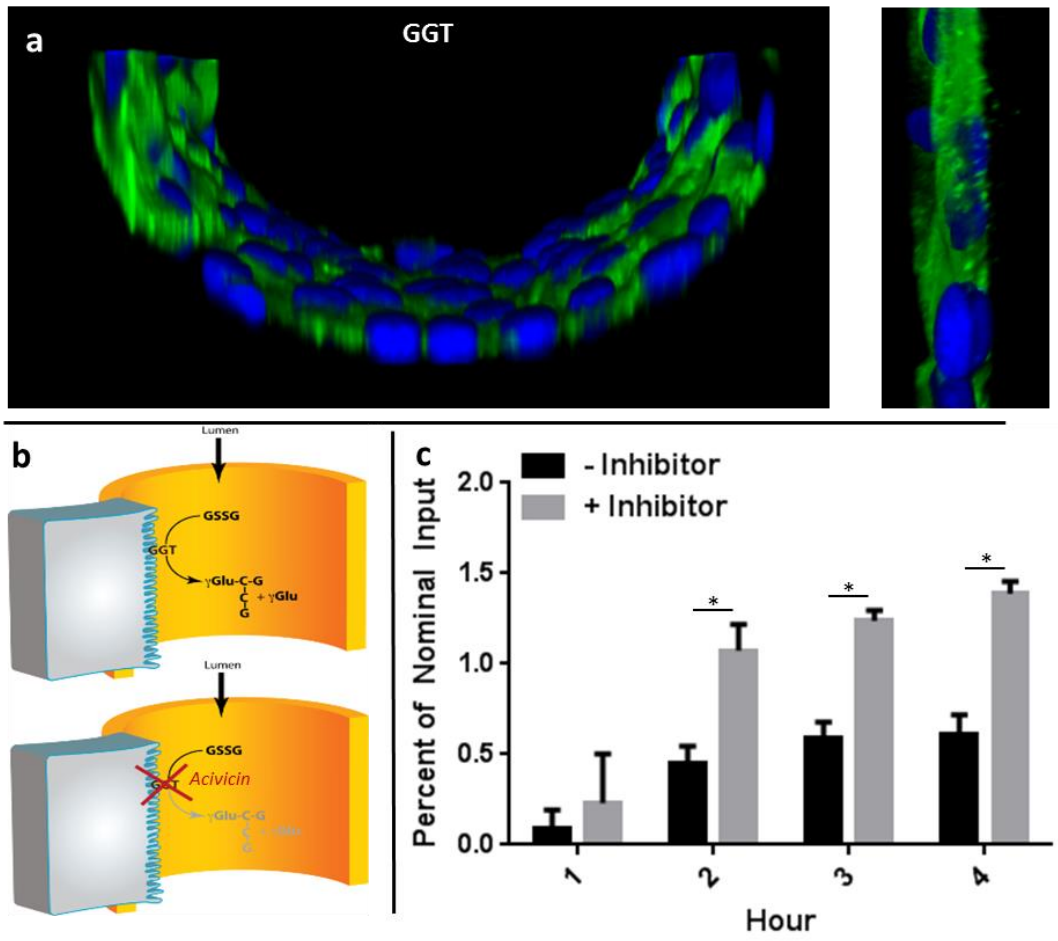

Figure 2.3 - GGT activity in human kidney 3D MPS.

(a) Immunocytochemistry reveals proper apical localization of γ-glutamyl transpeptidase (GGT) (green) in juxtaposition to nuclei (blue) within the proximal tubular epithelial cell tubule. (b) GGT is functionally essential to cleaving the γ-glutamyl moiety from oxidized glutathione and can be inhibited by acivicin. (c) GGT activity as determined by oxidized glutathione abundance in the presence and absence of inhibitor, acivicin (n = 4 microphysiological system [MPS] devices) *P < 0.001, 2-tailed t-test. Bars = 20 μm for the tubule and 10 μm for the wall. 3D, 3-dimensional; GSSG, glutathione disulfide.

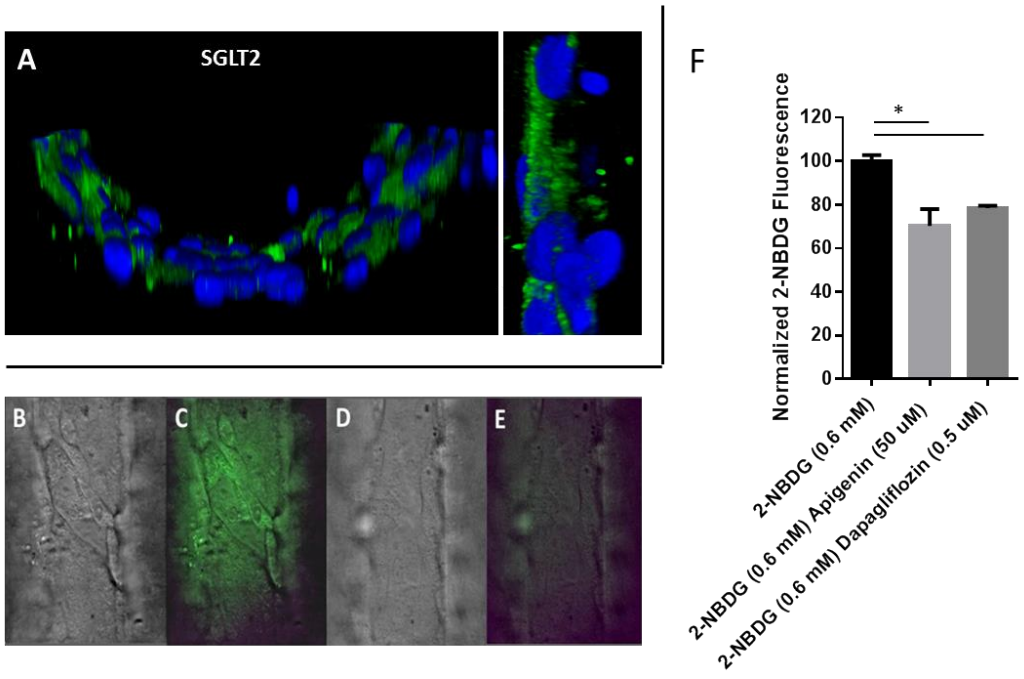

Figure 2.4 - Glucose reabsorption in human kidney 3D MPS.

(a) Glucose is actively reabsorbed from the urine via sodium glucose cotransporter-2 (SGLT2) located on the apical membrane in the proximal tubular epithelial cell tubule. Immunocytochemistry reveals proper apical localization of SGLT2 (green) in juxtaposition to nuclei (blue). (b,d) Differential interference contrast images showing the structure of proximal tubular epithelial cells in the microphysiological system (MPS) in the presence and absence of SGLT2 inhibitor, apigenin. (c,e) Fluorescent images showing the distribution of the fluorescent glucose analog, NBDG. (c) NBDG, a fluorescent glucose analog, was actively reabsorbed in the absence of inhibitor and (e) was not absorbed in the presence of inhibitor. (f) Quantification of a cell-associated fluorescent signal following subtraction of autofluorescence, demonstrating significant reduction of glucose uptake in the presence of inhibitors apigenin and dapagliflozin (n = 3 MPS devices/group) *P < 0.001, unpaired t-test. Bars = (a) 20 µM for the tubule and 10 µM for the wall and (e) 50 µM. 3D, 3 dimensional.

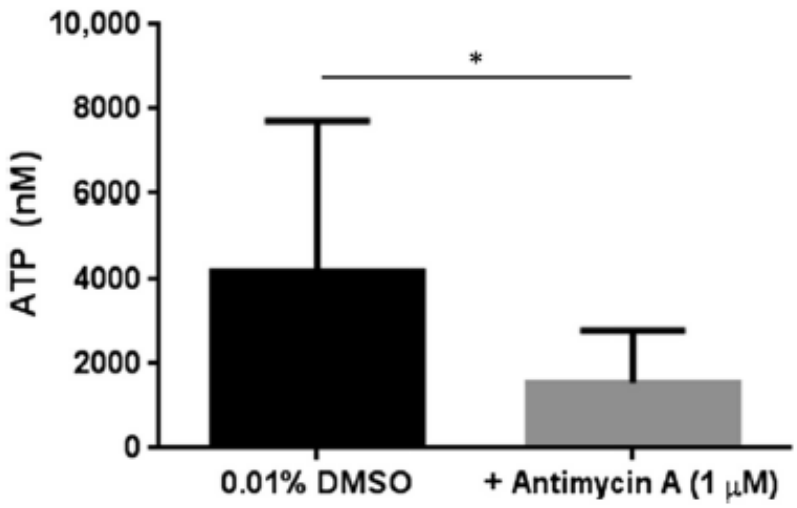

Figure 2.5 - Cellular ATP content in control and antimycin A–treated (1 μM, 24 hours) MPS.

(n = 3 microphysiological system [MPS] devices/group.) *P =0.05, 2-tailed t-test. ATP, adenosine triphosphate; DMSO, dimethylsulfoxide.

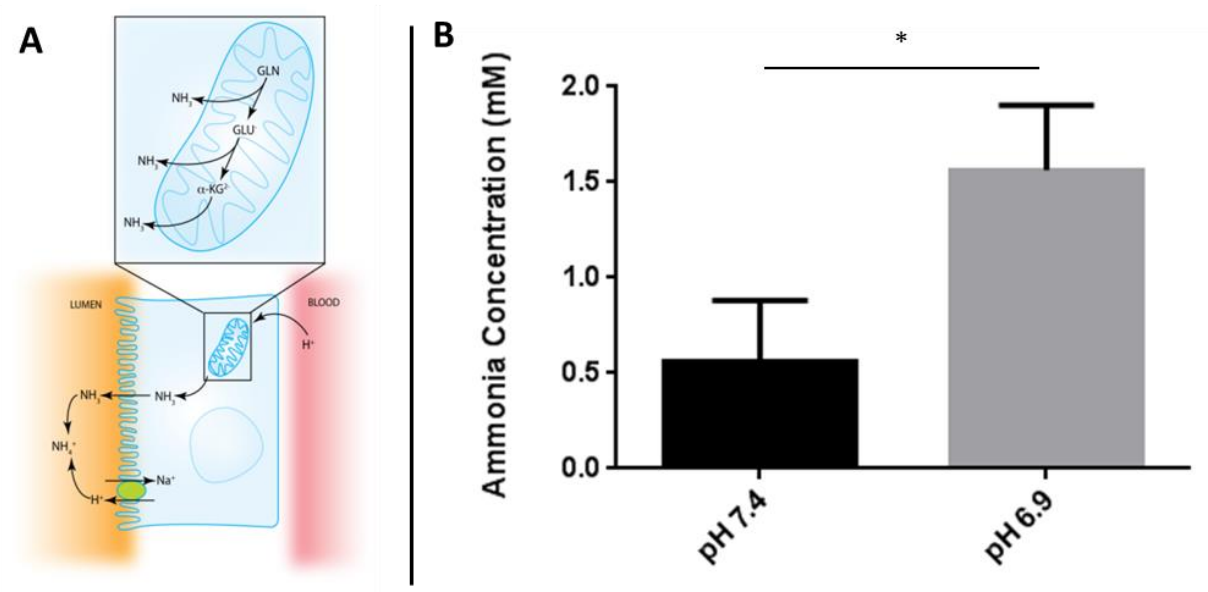

Figure 2.6 - Ammoniagenesis in human kidney 3D MPS.

(a) The physiological response to a drop in either blood or luminal pH resulting in the generation and secretion of ammonia in the tubular outflow. (b) With the microphysiological system (MPS), luminal media was initially at pH 7.4 and then switched to pH 6.9. Secreted ammonia in the outflow was quantified spectrophotometrically from 4 separate devices after 4 hours and was significantly different when exposed to acidic conditions. *P = 0.05, 2-tailed t-test. 3D, 3-dimensional; α-KG2, alpha ketoglutarate; GLN, glutamine; GLU, glutamic acid.

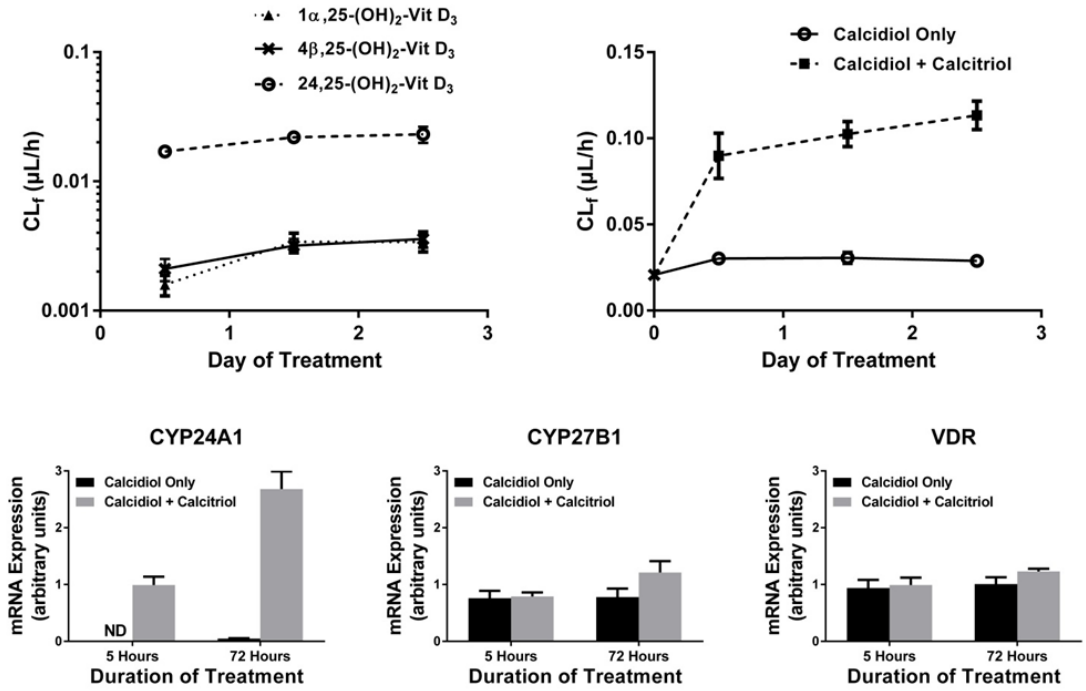

Figure 2.7 - VDR-mediated regulation of vitamin D metabolism in human kidney 3D MPS.

(a) Formation clearance of the 1α,25-$(OH)_2$-vitamin (Vit) D_3 (calcitriol), 4β,25-$(OH)_2$-Vit D_3, and 24,25-$(OH)_2$-Vit D_3 over 3 days exposure of proximal tubular epithelial cells (PTECs) cultured in microphysiological system (MPS) to 1 µM 25-OH-Vit D_3 (calcidiol). Clearance values are plotted at midpoint of collection interval. Sequential metabolism was assumed to be negligible. (b) Formation clearance of the 24,25-$(OH)_2$-Vit D_3 was greater in MPS-seeded PTEC cultured in media with both 0.5 µM 1α,25-$(OH)_2$-Vit D_3 (calcitriol) and 1 µM 25-OH-Vit D_3 (calcidiol) than those exposed to 1 µM calcidiol alone. Clearance values were plotted at the midpoint of the collection interval. Sequential metabolism was assumed to be negligible. Baseline data point (x) for formation clearance (CL_f) was determined from the experiment presented in (a). Effect of calcitriol on gene expression of (c) CYP24A1, (d) CYP27B1, and (e) vitamin D receptor (VDR) in MPS-seeded PTEC. Relative accumulation of CYP24A1 mRNA

transcripts was greater in MPS-seeded PTEC cultured in media with both 1α,25-$(OH)_2$-Vit D_3 (calcitriol) and 25-OH-Vit D_3 (calcidiol) than those exposed to calcidiol alone. Induction of CYP24A1 mRNA occurred rapidly (5 hours) and persisted for the duration of treatment (3 days). No detectable (ND) transcripts of CYP24A1 were observed in the 5-hour calcidiol-only group. There were no substantial changes in CYP27B1 and VDR mRNA expression over the duration of treatment. All genes of interest were standardized to glyceraldehyde-3-phosphate dehydrogenase. CYP, cytochrome P450.

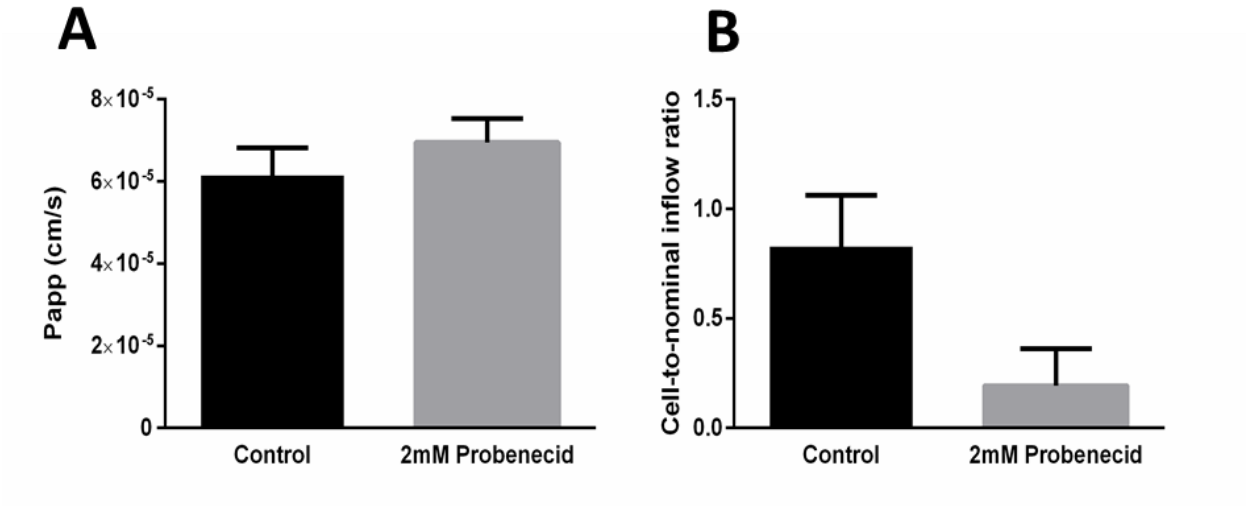

Figure 2.8 - Comparison of transepithelial transport of PAH across PTEC monolayers in a conventional 2D Transwell and a flow-directed 3D MPS.

(a) In a Transwell monolayer, probenecid had no effect as depicted by no change in the mean para-aminohippurate (PAH) apparent permeability (Papp) values between inhibitor and control group. Papp values were derived as explained in Supplementary Materials and Methods. (b) In a flow-directed 3-dimensional (3D) microphysiological system (MPS), probenecid reduced the secretion of PAH by approximately 4-fold. 2D, 2-dimensional; PTEC, proximal tubular epithelial cell.

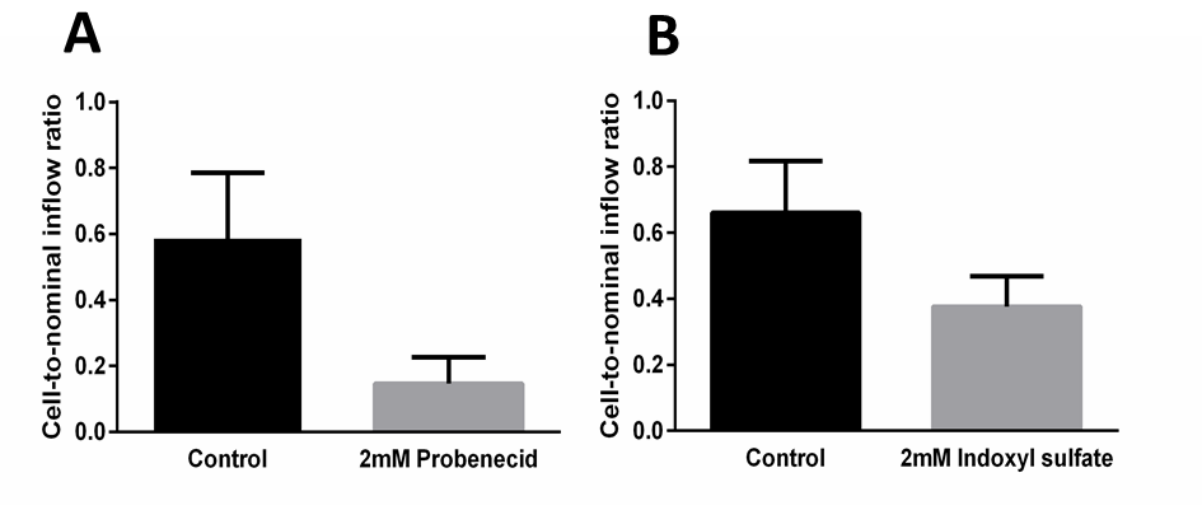

Figure 2.9 - Transepithelial transport of uremic solute indoxyl sulfate in a flow-directed human PTEC 3D MPS.

(a) Indoxyl sulfate secretion in microphysiological system (MPS) device, inhibitable by probenecid. (b) Para-aminohippurate (PAH)-indoxyl sulfate interaction as demonstrated by inhibition of PAH secretion by 2 mM indoxyl sulfate. 3D, 3-dimensional; PTEC, proximal tubular epithelial cell.

Chapter 3

Nonclinical safety assessment of polymyxin antibiotics utilizing 3D kidney microphysiological system

The work presented in this chapter will be submitted for publication:

Nature Medicine

Authors:

Elijah J. Weber[1], Kevin A. Lidberg[1], Lu Wang[3], Theo K. Bammler[3], James W. MacDonald[3], Cecilia Tran[4], Kelly M. Hines[4], Josi Herron[4], Libin Xu[4], Maria Beatriz Monteiro[5] , Susanne Ramm[5] ,Vishal Vaidya[5] Martii Vaara[6,7,8], Timo Vaara[6] , Jonathan Himmelfarb[2*], Edward Kelly[1*]

Affiliations:

[1]Department of Pharmaceutics, University of Washington, Seattle, WA
[2]Department of Medicine, Division of Nephrology, Kidney Research Institute
University of Washington, Seattle, WA, 98195, USA
[3]Department of Environmental and Occupational Health Sciences, University of Washington, Seattle, WA, USA.
[4]Department of Medicinal Chemistry, University of Washington, Seattle, WA
[5]Laboratory of Systems Pharmacology, Harvard Program in Therapeutic Sciences, Harvard Medical School, Boston, Massachusetts
[6]Northern Antibiotics Ltd, Technopolis, Tekniikantie 14, FI-02150 Espoo, Finland.
[7]Division of Clinical Microbiology, Helsinki University Hospital, FI-00029 Helsinki, Finland.
[8]Department of Bacteriology and Immunology, Helsinki University Medical School, FI-00014 Helsinki, Finland.

*Co-Corresponding Authors:

Edward J. Kelly: edkelly@uw.edu

Jonathan Himmelfarb: jhimmelfarb@nephrology.washington.edu

3.1 Abstract

Polymyxins are potent antibiotics but their use is restricted because of nephrotoxicity. To mitigate nephrotoxicity, structural analogues of polymyxins are being developed. Using a microphysiological model of the human kidney proximal tubule, we assessed the safety of polymyxin B and its analogues NAB739 and 741. Following polymyxin B treatment, the urinary biomarker kidney injury molecule-1 and a panel of injury-associated microRNAs were significantly increased in device effluents. Transcriptional profiling identified cholesterol biosynthesis as the primary pathway induced by polymyxin B. In contrast, we observed minimal changes in gene expression and no significant upregulation of urinary biomarkers in response to the NABs. Our findings demonstrate the improved safety of NAB739 and 741, reveal cholesterol biosynthesis as a novel pathway affected by polymyxin B, and support the use of microphysiological models for safety assessment.

3.2 Introduction

Discovered in the late 1940's from *Paenibacillus polymyxa* (*Bacillus polymyxa)*, polymyxin B (PMB) has been prescribed alone or in combination with other antimicrobials to treat life-threatening gram-negative bacterial infections(*56*, *57*). PMB belongs to the cyclic lipopeptide class of antibiotics and is comprised of a decapeptide sequence that contains a polycationic heptapeptide ring and a fatty acyl tail (**Supplemental Figure 1**). The amphipathic chemistry of PMB is essential for antibacterial activity. Electrostatic interaction between the cationic residues of PMB with negatively charged lipid A phosphates at the outer membrane of gram-negative bacteria displaces divalent cations (e.g. Mg^{2+} and Ca^{2+}) that are necessary for lipopolysaccharide leaflet stability and allows the hydrophobic tail of PMB to be inserted into the outer

membrane(*58*). This stimulates 'self-uptake' through the exchange of lipids between the inner and outer membranes(*59*). Together, these events disrupt lipid homeostasis and promote permeabilization of the membrane to produce bactericidal effects(*58, 59*). Importantly, multidrug resistant bacteria are susceptible to PMB. And even though resistance can be acquired through polymorphisms which reduce the negative charge of the lipopolysaccharide layer, it remains rare(*60*).

The rise in multidrug resistant bacterial infections has renewed interest in the polymyxin antibiotics, yet PMB continues to only be used as a last-resort treatment because of dose-limiting nephrotoxicity(*61*). In a retrospective study of 73 patients receiving PMB, close to 60% developed acute kidney injury (AKI)(*62*). In mice and rats treated with PMB, the primary site of accumulation and injury within the kidney was found to be the proximal tubule (*63, 64*). These data are in agreement with the pharmacokinetics of PMB in humans where the renal clearance of PMB is only a small fraction of the expected filtration clearance, indicating that PMB undergoes extensive tubular reabsorption(*65*). Accumulation of PMB in proximal tubule epithelial cells (PTECs) can likely be attributed to the negative charge of the brush border, the high expression of transporters and receptors involved in reabsorption of solutes from the ultrafiltrate, or a combination of the two (*66, 67*). Consequently, the toxicity of PMB towards PTECs may be driven by its polycationic nature. Indeed, analogues of PMB (**Supplemental Figure 1**: *NAB739, NAB741*) are currently being developed by Spero Therapeutics with fewer cationic charges that exhibit improved renal safety profiles in both *in vitro* and *in vivo* models (*18, 68-74*).

New biomarkers, particularly those of tubular origin, show excellent promise for detecting and reporting the severity of acute kidney injury (AKI). Elevations in traditional biomarkers like serum creatinine and blood urea nitrogen are often temporally delayed from the incident of AKI

or require a significant loss of renal function before changes are detectable (*75*). This is a major issue as early detection of AKI could alter therapeutic care or prompt the initiation of renoprotective measures. One alternative that has demonstrated excellent utility in preclinical and clinical settings is kidney injury molecule 1 (KIM-1). KIM-1 is a transmembrane glycoprotein that is absent from non-proliferative PTECs, but becomes highly upregulated during AKI and is proteolytically cleaved at the plasma membrane to produce a soluble form that is detectable in urine (*65, 76, 77*). Surface expression of KIM-1 enables clearance of apoptotic bodies and necrotic debris, which is proposed to be a protective mechanism of tubular cells to resolve injury and prevent inflammation(*28, 78*). Most importantly, KIM-1 is more sensitive and specific than traditional biomarkers for informing on the site and degree of renal injury, even across different forms of insults (drug-induced, ischemia reperfusion, etc.)(*79, 80*). Other promising biomarkers of AKI include heme oxygenase 1 (HMOX1) and various microRNAs (miRs) such as miR-16, 21, 24, 30, 132, 155, 192, and 200 (*79-86*).

Despite knowledge of their existence for 6 decades, the definitive mechanisms of polymyxin nephrotoxicity remain poorly understood. *In vitro* studies have implicated death receptor activation and perturbation of the mitochondrial membrane along with a loss of membrane potential and generation of reactive oxygen species as potential pathways responsible for polymyxin-induced injury. However, these findings are based primarily on transformed cell lines that were exposed to supra-physiologic drug concentrations(*23, 87, 88*). Therefore, we cultured primary human PTECs in a 3-dimensional microfluidic device to create a kidney tubule microphysiological system (MPS) and used it to 1) probe the mechanism of PMB nephrotoxicity and 2) compare the safety of PMB to its NAB analogues. The kidney tubule MPS performs normal physiological functions of the proximal tubule and displays appropriate injury responses,

such as induction of HMOX-1 and shedding of KIM-1(*81*, *89*). These properties, along with the ease of sampling, imaging, and harvesting of cells, make the kidney tubule MPS well suited for mechanistic studies. Furthermore, we chose to couple analysis of protein and miRNA biomarkers of AKI with whole-transcriptome sequencing to ensure an unbiased, holistic assessment. To our knowledge, this is the first demonstration of a human MPS platform for both safety testing of new chemical entities as well as defining unique toxicological pathway responses of the FDA-approved parent molecule.

3.3 Methods

3.3.1 Tissue Acquisition and Cell Isolation

Human kidney tissues were collected at the University of Washington Medical Center under a UW Institutional Review Board approved Human Subjects protocol. Tissue was processed within 12 hours as previously described (J Clin Invest. 2008 May;118(5):1657-68) (*28*). In brief, tissue was finely minced under sterile conditions, subjected to collagenase digestion with shaking at 37°C for 30 min, mixed 1:1 with horse serum, vortexed, allowed to briefly settle and supernatant harvested. The cell suspension was centrifuged, washed and plated inT25 flasks containing DMEM/F12 media supplemented with insulin, transferrin, selenium and hydrocortisone.

3.3.2 Cell Seeding in Nortis Device

The Nortis devices were constructed with an extracellular matrix of type I collagen, and the cell chamber was coated with type IV collagen to facilitate cell adhesion. Cultures of primary renal epithelial cells, upon reaching >80% confluency, were subjected to trypsin digestion and manual cell scraping to obtain single cell suspensions. The cells were counted, washed and resuspended

at a concentration of 20 x 10^6 cells/mL and 1-2 μL were injected into the Nortis device. Cells were incubated to allow matrix adhering for 12 hours before initiating flow at a rate of 0.5 μL/min. The integrity of the tubule cell structure was assessed grossly by light microscopy on a weekly basis.

3.3.3 PMB-dosimetry in 2D cell culture

Primary proximal tubule epithelial cells (PTEC) and transformed cell lines (LLCPK-1, MDCK, HK-2) were seeded at a density of approximately 10,000 cells/well in a 96-well plate and allowed to culture overnight before dosing. Polymyxin B (NDC 39822-0170-2, X-Gen Pharmaceuticals, Horseheads, NY) dosimetry was assessed across 10 different concentrations starting at concentration 1 mM and serial diluted down 1:1 with cell medium. Cells were exposed to PMB for 48 hours before cell cytotoxicity was measured using the Abcam ab112118 Cell Cytotoxicity Assay Kit (Abcam, USA). EC50s across multiple human donor PTECs and transformed cell lines were defined and plotted using *Prism GraphPad*.

3.3.4 Viability demonstrated using Live/Dead staining

The LIVE/DEAD® viability/cytotoxicity kit and Hoechst 33342 (Life Technologies) were used to distinguish viable cells from dead cells according to manufacturer's specifications. Briefly, calcein AM (final conc. 2 μM), EthD-1 (final conc. 4 μM) and Hoechst 33342 (final conc.0.1 μg/ml) were diluted in pre-warmed D-PBS. MPS chips were perfused at 5 μl/min via a luminal port of kidney MPS for 20 minutes and then incubated for 10 minutes at 37 ºC. After the staining procedure, chips were imaged using fluorescent microscopy to visualize live (green stained cells) and dead cells (red stained cells) with nuclei marker Hoechst 33342 (blue stained cells).

3.3.5 Analysis of ROS Generation

Primary human PTECs were grown to approximately 75% confluency in a multi-chamber culture slide. Upon 75% confluency, PTECs were individually exposed to increasing concentrations of PMB (0, 50, 100, 250 μM) for 48 hours then stained for ROS generation using both CellROX (C10444, ThermoFisher, Waltham, MA) for 30 minutes and MitoSOX (M36008, ThermoFisher, Waltham, MA) for 10 minutes. After staining, PTECs were imaged using fluorescent microscopy with a Nikon (Melville, NY) Ti-S microscope and both red and green intensity was quantified with Nikon Eclipse software. PMB-treated cell's ROS intensity was normalized to the control chamber and the results were expressed graphically (per nuclei).

3.3.6 Analysis of Kidney Injury Molecule-1 (KIM-1)

Effluents of kidney MPS exposed to either 50μM PMB, 50 μM NAB739 / NAB741 (Northern Antibiotics Ltd – Helsinki, Finland), or control at both 24 and 48 hours were analyzed for human KIM-1 using the Mesoscale Diagnostics Human KIM-1 Kit (K141JHD-2).

3.3.7 Analysis of miRNA

200ul of effluents were collected after 48 hours of exposure to PMB (dose-escalation study) and used for miRNA isolation using miRNeasy kit (Qiagen). miRNAs 21, -200c, -432, -132, -155, -16, -192, -24, -30e were quantified with custom miScript miRNA PCR Array. miRNA Ct (threshold cycle) values were normalized using the geometric mean of technical controls (miRNA reverse transcription control and positive PCR control) for each sample. The 2-ddCt was calculated compared to the control group.

3.3.8 Isolation of mRNA / RNA-Sequencing

Cells cultured within the kidney MPS were isolated after 48 hours of treatment and RNA was isolated using the Qiagen mRNeasy micro kit (74004, Qiagen USA). RNA library was prepared using Clontech SMARTer Stranded Total RNA Sample Prep Kit - Low Input Mammalian (634861, Takara Bio USA) and RNA-sequencing was performed at 300 cycles in 2 lanes using the Illumina NextSeq 500 High Output v2 Kit.

3.3.9 Immunocytochemistry Analysis of Heme Oxygenase-1 (HO-1)

Anti-HMOX-1 antibody (rabbit polyclonal, Abcam, Cambridge, MA) was used. Cells were fixed with 4% formaldehyde in PBS. Samples were permeabilized with PBST (PBS plus 0.1% Tween 20) and blocked with 1% bovine serum albumin (BSA) for 1 hour. The samples were then incubated with primary (1:100) and secondary (1:1000) antibodies followed by washing, using a standard ICC protocol. Secondary antibodies were goat anti-rabbit IgG (H+L) Secondary Antibody, Alexa Fluor® 594 conjugate (Abcam, Cambridge, MA). Diluted ProLong Gold Antifade Mountant with DAPI reagents (ThermoFisher Scientific) were used in the final step of staining. Cells were imaged using fluorescent microscopy with a Nikon (Melville, NY) Ti-S microscope and red (Fluor® 594) intensity was quantified with Nikon Eclipse software.

3.3.10 Quantification of cholesterol in the effluent

Optima LC/MS grade solvents (water, methylene chloride, chloroform, formic acid, and methanol) and sodium chloride (ACS certified) were purchased from ThermoFisher Scientific (Grand Island, NY, USA). Materials and supplies used for lipid extraction and UHPLC-MS were purchased from ThermoFisher Scientific.

Deuterated (d_7 = [25, 26, 26, 26, 27, 27, 27-^{2}H]) 7-dehydrocholesterol was prepared as reported previously (*90*). $^{13}C_3$-desmosterol was a gift from Drs. Ned Porter and Keri Tallman and were

prepared as reported (*90*). All other sterol standards and internal standards were purchased from Avanti Polar Lipids (Alabaster, AL, USA). 4-phenyl-1,2,4-triazoline-3,5-dione (PTAD) was purchased from Sigma-Aldrich.

3.3.11 Lipid extraction from kidney chip effluents

Prior to lipid extraction, internal isotopically labeled sterol standards [d7-cholesterol (50 ng), d7-7-dehydrocholesterol (50 ng) and $^{13}C_3$-Desmosterol (10 ng)] were added to each sample. Folch solution (2 mL, chloroform:methanol = 2:1 v/v) was added directly to each kidney chip effluent sample (100 µL). NaCl aqueous solution (0.5 mL, 0.9% w/v) was then added and the resulting mixture was briefly vortexed and then centrifuged for 5 min in a clinical tabletop centrifuge (at ambient temperature). The lower (organic) phase was recovered, transferred to a 15 mL polypropylene conical centrifuge tube and the solvent was removed in vacuo using a Speed Vac® (Thermo Fisher Savant). Finally, the resulting dried extracts were re-dissolved in methylene chloride (300 µL) before further processing.

3.3.12 UHPLC -MS/MS analyses of cholesterol in kidney chip effluents

Analysis of cholesterol was performed by UHPLC-MS/MS using a triple quadrupole mass spectrometer (API 4000 ™; SCIEX, Ontario, Canada) equipped with atmospheric pressure chemical ionization (APCI). For analysis, 100 µL of re-constituted cholesterol was transferred to an LC vial, dried under a stream of argon, and reconstituted in 20 µL of 90% methanol with 0.1% formic acid. Reverse-phase chromatography was performed with the following conditions: C18 column (Kinetex ®, 100 mm x 2.1 mm, 1.7 µm particle dia.; Phenomenex, Torrence, CA, USA); flow rate, 0.4 mL/min; elution solvent, 90% MeOH with 0.1% formic acid.

MS conditions: nebulizer current, 3 mA; curtain gas, 10 psi ion source gas, 20 psi; collision gas, high; entrance potential, 10 V; collision energy, 25 V; declustering potential, 80 V; temperature, 300° C. For MS analysis, selective reaction monitoring (SRM) was employed to monitor the dehydration process of the ion [M+H]+ or [M+H-H2O]+ as described previously (*91-93*). Cholesterol was quantified relative to the d7-cholesterol internal standard.

3.3.13 PTAD Derivatization and UHPLC -MS/MS analyses of 7-dehydrocholesterol, lanosterol, and desmosterol in kidney chip effluents

Analysis of 7-dehydrocholesterol, desmosterol, and lanosterol was performed by UHPLC-MS/MS using a triple quadrupole mass spectrometer (API 4000 ™; SCIEX, Ontario, Canada) equipped with electrospray ionization (ESI). The analytes were derivatized using the PTAD derivatization method (*94*). 90 µL of each sample was dried under a stream of argon and reconstituted in 25 µL methanol. 5 µL of a 10 mg/mL PTAD stock solution in methylene chloride was added to the sample solution in methanol. The reaction was allowed to proceed for 10 minutes at ambient temperature before analysis. Reverse-phase chromatography was performed with the following conditions: C18 column (Kinetex ®, 100 mm x 2.1 mm, 1.7 µm particle dia.; Phenomenex, Torrence, CA, USA); flow rate, 0.3 mL/min; elution solvent, MeOH with 0.1% formic acid.

MS conditions: spray voltage, 4500 V; curtain gas, 10 psi ion source gas, 20 psi; collision gas, high; entrance potential, 10 V; collision energy, 23 V (for 7-DHC-PTAD adduct, 27 V); declustering potential, 94 V; temperature, 300° C. The PTAD adducts of 7-DHC, desmosterol, and lanosterol, were analyzed by selective reaction monitoring (SRM). For 7-DHC and d7-7-DHC, the loss of the PTAD derivative from the sodium adduct produced the ion [M+Na-PTAD]+, which was monitored (7-DHC/d7-7DHC, m/z 582.6/589.6 → 407.6/414.5). The

predominant precursor ions for the PTAD derivatives of desmosterol and lanosterol were solvent addition products in which methanol was added covalently (5). In these cases, the loss of MeOH from the PTAD derivative resulted in the ion [M+H-MeOH]+, which was monitored ($^{12}C/^{13}C_3$-desmosterol, m/z 592.6/595.6 → 560.5/563.6; $^{12}C/^{13}C_3$-lanosterol, m/z 634.4/637.4 → 602.5/605.3).

3.3.16 Statistical analysis

Data are reported as means ± SE. For comparison of means, statistical tests (Student's t-tests, 1-way and 2-way ANOVA with multiple comparisons test) were applied using GraphPad software (La Jolla, CA) with $P < 0.05$ as the statistical significance threshold.

Statistical analysis for global transcriptomics was carried out using R (version 3.4.0). Prior to fitting any models, we first excluded any genes that are expressed at consistently low levels across all samples. Since not all donors received all the treatments, we used linear mixed models, with the treatment as the fixed effect and the donor as the random effect, where the intra-donor correlation was incorporated into the covariance(*95*). In order to use linear mixed models, we first converted the gene counts to log counts/million using the trimmed mean of M-values (TMM) normalization(*96*) and then estimated both observation level and sample-specific weights using the voomWithQualityWeights function from the Bioconductor limma package (*97-99*). The observation-level weights allow us to use a linear mixed model (by accounting for the dependence between mean and variance), and the sample-specific weights enable us to up or down-weight individual samples. We selected genes based on a 1.25-fold or greater difference in expression and a false discovery rate (FDR) of 5%, meaning that we estimate at most that 5% of the significant genes are false positives. Rather than using a *post hoc* fold change filtering criterion, we used the treat function from limma, which incorporates the fold change into the statistic,

meaning that instead of testing for genes which have fold-changes different from zero, we test whether the fold-change is greater than a 1.25-fold in absolute value (*95*).

3.4 Results

3.4.1 PMB-dose escalation in 2D culture and 3D kidney MPS.

To detect differences in sensitivity to PMB, we first investigated PMB-induced cytotoxicity in 2D culture to define dose-response relationships between PTECs and transformed cell lines (LLCPK-1, MDCK & HK-2) as the latter group have been traditionally used to model PMB-induced cytotoxicity (*6*, *100*). Following 48 hours of treatment, PTECs displayed increased sensitivity to PMB-induced cytotoxicity (PTEC EC_{50} Range: 45.7 to 123 μM, LLCPK-1 EC_{50}: 246 μM, MDCK EC_{50}: 389.1 μM, HK-2 EC_{50}: 48.5 μM) as indicated in **Supplemental Table 1**. Comparing the average EC_{50} value of PTECs (94.6 μM), cytotoxicity sensitivity was 4-fold higher compared to MDCK, 2.6-fold higher compared to LLCPK-1, and approximately 50 percent lower compared to HK-2.

ROS generation was measured in response to increasing concentrations of PMB exposure using both CellROX (a free radical sensor that fluoresces when oxidized by ROS) and MitoSOX (a fluorogenic dye that detects intracellular mitochondrial superoxide). In response to PMB exposure, cell morphology and density significantly changed in a dose-dependent relationship. CellROX and MitoSOX levels were minimal in controls and increased in response to PMB (50 - 250 μM) (**Figure 1A**). Quantifying fluorescence intensity (relative to control) showed significant production of both cellular ROS (at 100 and 250 μM PMB) and 2.5-fold higher mitochondrial ROS at 100 μM PMB (**Figure 1B**).

Using PTECs cultured within the 3D kidney MPS, PMB dose-escalation was investigated over a period of 48 hours (**Supplemental Figure 2A**). After 48 hours of treatment, concentrations that exceeded 250 μM resulted in severe cytotoxicity, as demonstrated by loss of 3D tubular integrity and high percentage of dead/dying cells. Additionally, AKI sensitive urinary microRNA (miR-21, -200c, -423), were analyzed in MPS effluent and showed observable increases with PMB dose-dependency (**Supplemental Figure 2B**). Subsequent experiments at 50 μM PMB resulted in no overt toxicity while concomitantly retaining a high degree of viability. Thus, subsequent experiments to investigate mechanism(s) of PMB toxicity utilized 50 μM drug concentrations.

3.4.2 Polymyxin-induced biomarker response

3.4.2.1 Kidney Injury Molecule-1 (KIM-1)

The MPS response to toxicant exposure was assessed by measuring KIM-1. KIM-1 levels were quantified in MPS effluents after treatment with 50 μM PMB, 50 μM NAB-739, or 50 μM NAB-741 after 24 and 48 hours of exposure. Results of the KIM-1 response amongst eight different human donor cell lines are summarized in **Figure 2**. In response to 50 μM PMB exposure at both 24 and 48 hours, the concentration of KIM-1 was significantly higher ($P < 0.001$) in the effluent of the MPS and was approximately 4-fold higher relative to control levels of KIM-1. Furthermore, a multiplex analysis of kidney injury biomarkers (Calbindin, Clusterin, Osteoactivin, KIM-1, VEGF, and αGST) was assessed using PMB treated samples, which resulted in significant differences for Osteoactivin, KIM-1, VEGF, and αGST relative to the control group (**Supplemental Figure 3**).

The safety of two structural analogues of PMB, NAB739 or NAB741, was demonstrated by the lack of "urinary" biomarker response via KIM-1 induction (**Figure 2**). After treatment with NAB

compounds, there was no statistically significant change at 24 hours for NAB739 (P =0.38) or NAB741 (P =0.31). This was also the case at 48 hours of treatment for both NAB739 (P =1.0) and NAB741 (P =0.96). However, there was a modest (2-fold) increase at both 24 and 48 hours of treatment for NAB739. Collectively, these results demonstrate the utility of the 3D kidney MPS to detect urinary biomarker injury at early time points as well to distinguish degrees of safety across structural variants of PMB.

3.4.2.2. Urinary microRNA (miRNA)

In addition to measuring KIM-1 as a biomarker of AKI, we also tested for the presence of several miRNAs associated with AKI (*82, 83*). After 48 hours of 50 μM PMB exposure, the miRNAs miR-21, 200c, 132, 155, 16, 24, and 30e were significantly higher in the MPS effluents (**Figure 3**). This observation was consistent amongst multiple donors with average miRNA induction being 250-fold higher than control 3D kidney MPS.

3.4.2.3 Heme Oxygenase-1(HO-1)

Cell-associated response to PMB exposure was assessed by quantifying HMOX-1 expression using immunocytochemistry. After 48 hours of 50 μM PMB exposure, cell-associated HMOX-1 was approximately 5-fold higher relative to control across multiple donors (**Figure 4**). In contrast, exposure to NAB739 and NAB741 resulted in HMOX-1 levels similar with the control group (data not shown) indicating lack of HMOX-1 induction, in agreement with observed lack of other PMB injury responses.

3.4.2.4 Transcriptional response to polymyxin-exposure

Global transcriptional changes were assessed via RNA-seq, using RNA isolated from PTECs in 3D kidney MPS exposed to either 50 μM PMB or structural analogues NAB739 or NAB-741 for 48 hours. Based on the principal component analysis (PCA) plot (principal component 1 – treatment group, principal component 2 – donor), principal component 1 noticeably separated groups based on treatment into two distinct clustered sections, Control and PMB, indicating transcriptional differences in response to drug treatment (**Figure 5**). With this approach, we identified 808 genes that were significantly different between control and PMB treatment groups. Furthermore, structural analogues NAB-739/741clustered tightly with the control group (data not shown) which was supported by the transcriptional response to the structural analogues NAB-739/741 that identified only 18 genes and 1 gene relative to the control group, respectively.

In particular, we observed the transcriptional upregulation of the Metallothionein Family (MT1G, 1H, 1M, 1X, 2A, 1E, 1F), Unfolded Protein Response (5/32 genes), NRF-2 Mediated Antioxidant response (8/56), and Superpathway of Cholesterol Biosynthesis (16/25 genes) described in **Supplemental Table II**. Relative to control, PMB exposure caused a 1.31 $\log_2$ fold-change for HMOX-1, a 2.62 $\log_2$ fold-change for MT1G, a 2.58 $\log_2$ fold-change for MT1H, a 2.23 $\log_2$ fold-change for MT1M, a 2.21 $\log_2$ fold-change for MT1X, a 1.82 $\log_2$ fold-change for MT2A, a 1.51 $\log_2$ fold-change for MT1E, and a 1.47 $\log_2$ fold-change for MT1F. Additionally, canonical genes in the antioxidant NRF-2 Mediated Antioxidant response pathway were investigated including NQO1, GCLM, FTH1, GPX6, KEAP1, and SOD1 but were unaffected in response to PMB exposure, in concordance with the lack of an increase in ROS production at 50 μM PMB (**Figure 1B**).

To identify the specific pathways significantly perturbed at the transcriptional level, we used Qiagen Ingenuity® Pathway Analysis (IPA®) software which summarizes the canonical

pathways affected in response to PMB exposure (data not shown). The superpathway of Cholesterol Biosynthesis was the most significantly upregulated pathway (*P* -value: 1.22E-16) followed by Cholesterol Biosynthesis I, II, and III (*P* -value: 8.26E-13).

3.4.2.5 Quantification of cholesterol and cholesterol precursors in effluent of MPS.

In response to the upregulation of cholesterol biosynthesis from exposure to PMB, we quantified the concentration of cholesterol, 7-dehydrocholesterol, and desmosterol in the effluents of MPS. In **Figure 6**, MPS exposed to 50 μM PMB showed a significant increase ($P < 0.01$) in desmosterol at 48 hours and an observable increase in cholesterol accumulation ($P = 0.73$) in the effluent after 24 hours of exposure. When a single outlier was removed in the cholesterol data analysis, a trend towards significant difference between the control and PMB levels of effluent cholesterol was achieved (from $P = 0.73$ to $P = 0.07$). 7-dehydrocholesterol levels were unaffected upon PMB exposure indicating its potential lack of sensitivity to toxicant response compared to other precursors such as desmosterol.

3.5 Discussion

The nephrotoxicity of polymyxin antibiotics limits their use in patients and is a significant concern to drug developers seeking to identify safer alternatives. To address these challenges, we used a human kidney MPS to investigate PMB-induced nephrotoxicity at drug concentrations within the physiological range(*65*). In this study, we recapitulated PMB-induced nephrotoxicity *ex vivo* and assessed the safety of structural PMB analogues through analysis of multiple biomarkers associated with acute kidney injury.

As compared to traditional culture in 2D, PTECs cultured in the 3D kidney MPS exhibit both functional and structural aspects of the kidney proximal tubule(*89*). Transformed cell lines in

toxicity screens are typically used as a standardized cell type because of their ease of use and robust growth characteristics. However, in this study we found that they are less sensitive than primary PTECs, providing evidence to reconsider their relevance in toxicological screens. Furthermore, at the transcriptional level, 2D culture (**Supplemental Figure 4**) in the PCA plot clustered distinctly from 3D kidney MPS culture, indicating culture conditions play a significant role in gene expression.

Utilizing transformed cell lines, prior proposed mechanisms of PMB-induced toxicity were identified via a direct pathway to apoptosis from mitochondrial perturbation (with resultant ROS production) or an indirect pathway from death receptor activation in response to treatment with ≥ 1mM PMB (*23, 87*). To address these findings, we exposed PTECs to increasing concentrations of PMB (50 – 1000 μM) and identified a distinct response compared to high dose 2D culture systems. At 50 μM PMB, there was no significant mitochondrial perturbation, via ROS generation, until higher concentrations were reached (100 μM and 250 μM). Furthermore, interrogation of the global transcriptome (for PTECs grown in the 3D kidney MPS) revealed a significant upregulation of HMOX1 and MT gene family members when cells were exposed to 50 μM PMB. However, the primary pathways significantly affected involved upregulation of cholesterol biosynthesis. Interestingly, recognized Nrf2-antioxidant response genes (e.g. NQO1, GCLM, FTH1, GPX6, KEAP1, and SOD1) were unaffected despite significant induction of HMOX1 and MT genes. This lack of induction of an antioxidant response is supported by the lack of increased ROS production in response to 50μM PMB treatment (**Figure 1B**). Thus, the induction of HMOX1 and MT genes represent a "generalized" stress response in the kidney MPS. In support of this, treatment of kidney MPS with the nephrotoxic heavy metal cadmium

chloride (25 μM) also induces HMOX1 and MT genes without affecting genes associated with cholesterol biosynthesis (data not shown).

Upregulation of cholesterol biosynthesis is a unique pathway of PMB nephrotoxicity, which has never been reported. We have shown that in response to PMB exposure, both the cholesterol precursor (desmosterol) and cholesterol accumulate to higher levels in the effluent of the MPS. A recent study has shown how PMB-induced membrane damage can be significantly reduced when kidney membrane analogs were loaded with cholesterol (*101*). These findings are in agreement with our observations showing PMB-exposed cells generating cholesterol (via upregulation of cholesterol biosynthesis) and attempting to load cellular membranes. Interestingly, clinical findings from Johnson et al. show, in a cohort of patients with AKI, induction of HMG-CoA reductase (HMGCR) resulting in cholesterol loading within the proximal tubule causing an increase in urinary cholesterol levels (*102*). In our study, we also observed a significant induction of HMGCR mRNA in response to toxicant, which likely explains the effluent measurements. Furthermore, transcripts for ABCA1, an apical cholesterol efflux transport protein, were significantly down regulated in PMB-treated MPS (**Supplemental Table II**). Upregulation of HMGCR and downregulation of ABCA1 transcripts indicate that the cholesterol effluent response was likely not the result of transport-mediated sterol excretion, but rather the result of membrane-associated sterols being shed from the tubular lumen. Urinary cholesterol levels (including precursors) in response to acute kidney injury has the potential to be a sensitive biomarker of injury that, when detected early on, could provide guidance on patient care utilizing a commonly measured analyte.

The mechanisms of cellular uptake of PMB have been proposed to be primarily driven by megalin-mediated endocytosis (*103, 104*). However, it was recently shown that human

oligopeptide transporter 2 (PEPT2) mediates cellular uptake of polymyxins in renal tubular cells (HEK293) that overexpressed 15 essential solute carrier transporters(*66*). In our study, PEPT2 was significantly down regulated in response to PMB exposure (data not shown) which can indicate the transcriptional response to decrease cellular uptake of PMB via PEPT2. From our findings, targeting the inhibition of PEPT2-mediated transport may reduce the overall nephrotoxic effects of PMB accumulation.

Compared to a recent study observing increases of KIM-1/urinary creatinine levels in patients after 72 hours of PMB exposure, we observed significant accumulation of KIM-1 at both 24 and 48 hours of exposure, demonstrating the sensitivity of the 3D kidney MPS to detect early injury (*75*). Classical clinical biomarkers of acute kidney injury are continuously criticized for their lack of sensitivity (defined by receiver operating characteristic or ROC curves) highlighting the need to develop and identify new biomarkers of renal injury (*105*). Our results demonstrate the potential of KIM-1 as well as select miRNAs (miR-21, 200c, 132, 155, 16, 24, and 30e) to be significantly induced for detection of acute kidney injury in a sensitive and timely manner.

In summary, we have taken an organ-on-a-chip technology (human kidney 3D MPS) and applied it to toxicological investigation of a known class of nephrotoxic antibiotics (PMB) and defined the underlying unique mechanistic responses. In addition, we have evaluated the safety of two structural variants of PMB (NAB-739/741). NAB-741, now being developed by Spero Therapeutics as SPR741, has recently completed a Phase I clinical trial reporting, “data from our Phase 1 SAD/MAD clinical trial of SPR741 demonstrate SPR741 was well tolerated at single doses up to and including 800 mg and multiple daily doses up to and including 600 mg every eight hours for 14 consecutive days.”(*106*) The clinical trial results are in concordance with our MPS assessment of NAB-741, validating the utility of organs on chips technologies for drug

safety assessment. Furthermore, sensitive detection of urinary biomarkers (KIM-1 and miRNAs) using the human kidney 3D MPS highlights the implementation of new technologies for detection of acute kidney injury.

The human kidney 3D MPS has demonstrated its robust ability towards multiple preclinical development applications including toxicological investigations (*107*, *108*). New chemical entity advancement through the preclinical development pipeline is extremely costly when potential candidates are triaged based on inaccurate safety data. Preclinical test systems can often be the culprit behind false-positive results based off poor *in vitro* to *in vivo* predictions. The human kidney 3D MPS bridges the *in vitro* to *in vivo* gap providing a reliable system to detect human toxicity within 24 hours of exposure. Furthermore, implementation of organ-on-a-chip technologies, emphasizing the 3 R's of toxicology (reduce, refine, replace), will make a positive impact on the lives of preclinical species by reducing the overall number of animals tested, the utilization of only relevant species for predictive toxicity testing and the ultimate goal of replacing animals in preclinical safety assessment (e.g. human-on-a-chip)(*54*, *109*).

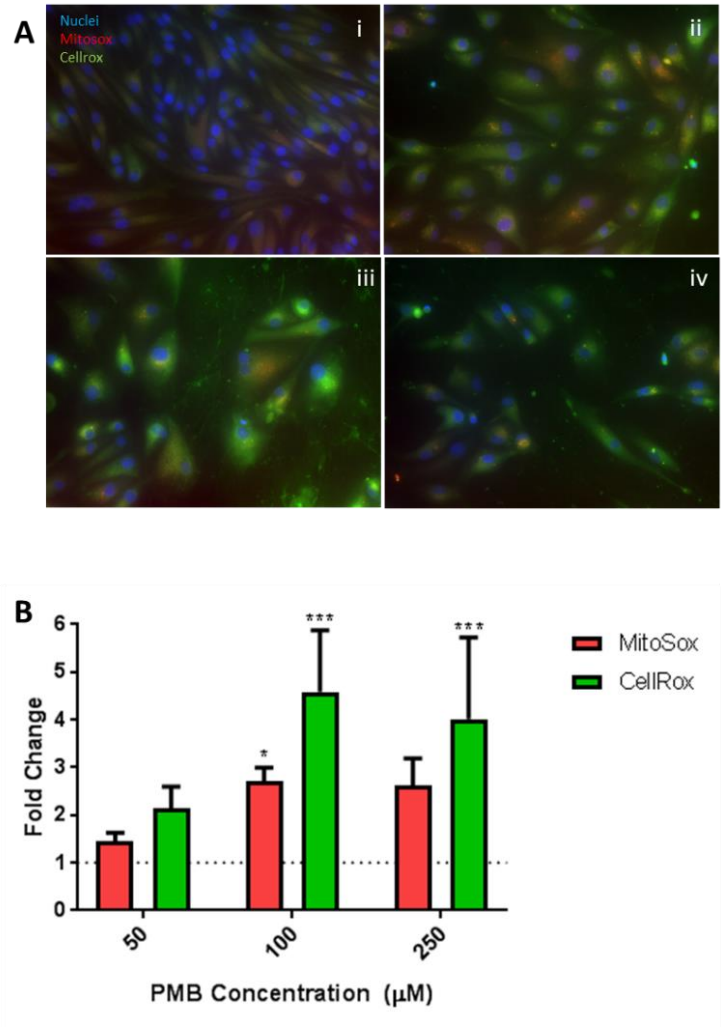

Figure 3. 1 Generation of intracellular reactive oxygen species from PMB exposure as evidenced by CellROX and MitoSOX fluorogenic stainin.

PTECs cultured in 2D for 72 hours were exposed to increasing concentrations (**Figure 1A: i.** 0 µM, **ii.** 50 µM, **iii.** 100 µM, **iv.** 250 µM) of PMB for 24 hours. Using cellular stains, MitoSOX (red) and CellROX (green), generation of ROS was dose-dependent with the highest concentration of PMB (100µM and 250µM) resulting in the most severe cell loss. Fluorescence intensity was quantified (**Figure 1B**) and normalized to control intensity values. A significant abundance of cellular ROS was generated at 100µM and 250µM PMB. Additionally, MitoSOX, an indicator of mitochondrial specific ROS, when quantified, showed a significant increase at doses higher than 50 µM PMB (100µM).

Group	Time (h)	Concentration (pg/mL)							
		Donor 1	2	3	4	5	6	7	8
Control (0 µM)	24	59.8 ± 3.5	92.7 ± 18.3	198.5 ± 19	116.2 ± 16.7	144.6 ± 23.9	89.1 ± 9.8	409.9 ± 51	73.8 ± 7.3
Polymyxin B (50 µM)		250.5 ± 34.9	307 ± 37.2	628.1 ± 54	291.2 ± 35.2	806.3 ± 39.9	325.9 ± 20	2625.4 ± 430.4	441.9 ± 33.2
NAB739 (50 µM)		132.8 ± 15.3	---	---	212.8 ± 26.3	---	---	702.8 ± 18.1	---
NAB741 (50 µM)		---	85.7 ± 5.2	---	---	---	88.7 ± 9.2	362.5 ± 72.9	---
Control (0 µM)	48	58.3 ± 13.5	32.3 ± 2.2	139.3 ± 9.3	157.5 ± 18.9	229.9 ± 49.7	125.3 ± 16.9	358.2 ± 50.5	108.9 ± 16.1
Polymyxin B (50 µM)		379.4 ± 56.7	193.4 ± 16.9	483.5 ± 71.9	338 ± 51.8	557.7 ± 33.5	385.7 ± 28.7	852.7 ± 140.3	341.7 ± 23.2
NAB739 (50 µM)		117.8 ± 13.2	---	---	294.2 ± 22.9	---	---	769.6 ± 18.2	---
NAB741 (50 µM)		---	44.7 ± 3.3	---	---	---	122.5 ± 19.1	500.5 ± 85	---

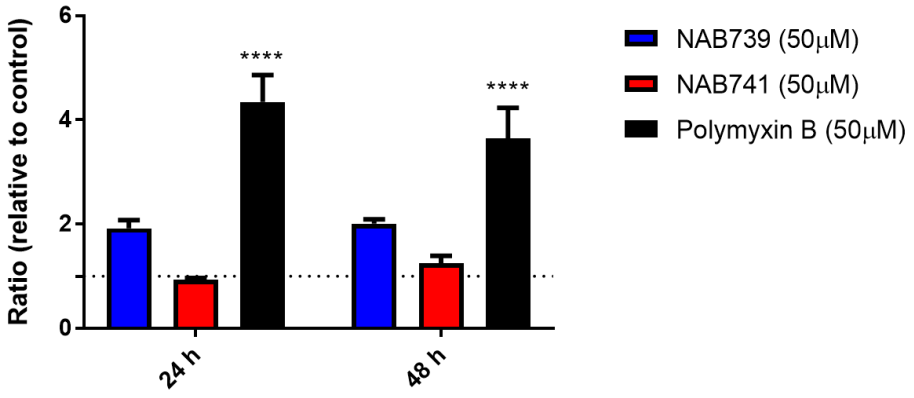

Figure 3. 2 - Kidney injury molecule-1 (KIM-1) significantly accumulates in the effluent of 3D kidney MPS in response to PMB exposure.

Effluent of the 3D kidney MPS was collected at both 24 and 48 hours of treatment (Control, PMB, NAB739, or NAB741) and analyzed for KIM-1 levels (pg/mL). Across multiple human donors (n = 8), significant accumulation of KIM-1 in the effluent was observed only in the PMB group. Furthermore, mean ratio of accumulation (relative to control) ±SEM indicated the relative safety of the NAB739/741 compounds compared to significantly toxic, PMB. * $P < 0.05$ ** $P < 0.01$ *** $P < 0.001$ **** $P < 0.0001$

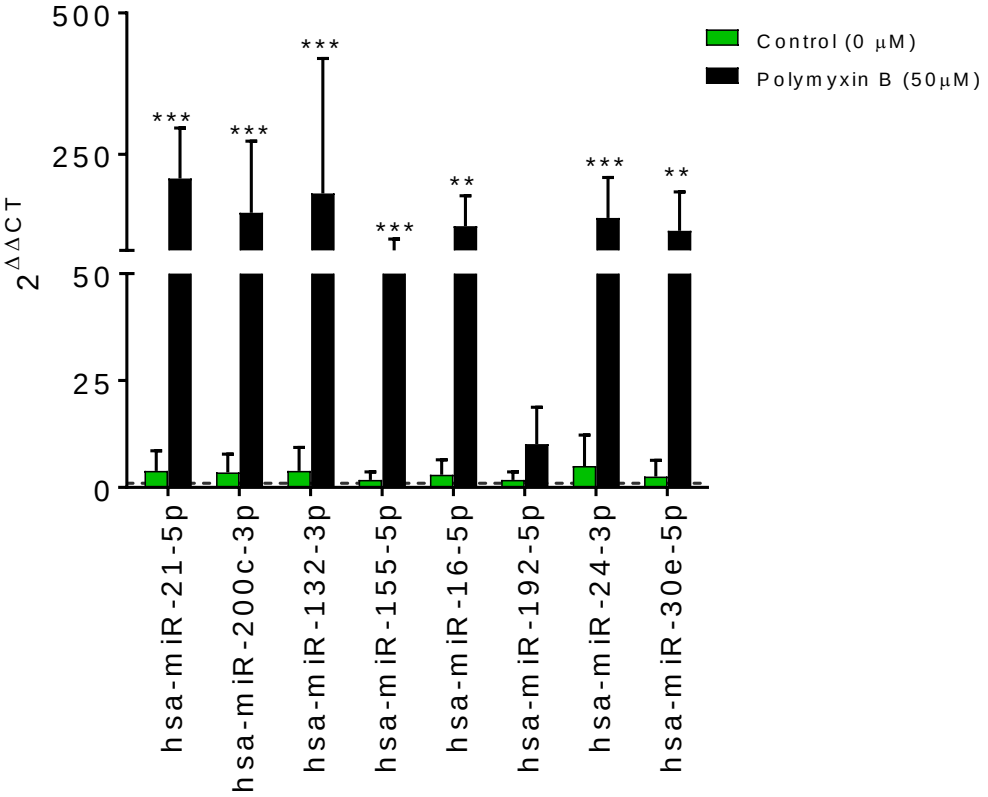

Figure 3. 3 - Urinary miRNA (-21, -200, -132, -155, -16, -24, -30e) significantly accumulate in the effluent of 3D kidney MPS across multiple donors in response to PMB exposure.

Quantifying the microRNA (miR) content in the effluent at 48 hours of exposure to either control or 50 μM PMB showed significant accumulation of miR (-21, -200c, -132, -155, -16, -24, -30e) across multiple human donor cells (n = 3) cultured within the 3D kidney MPS. Values are reported as the mean ± SEM. (* $P < 0.05$ ** $P < 0.01$ *** $P < 0.001$).

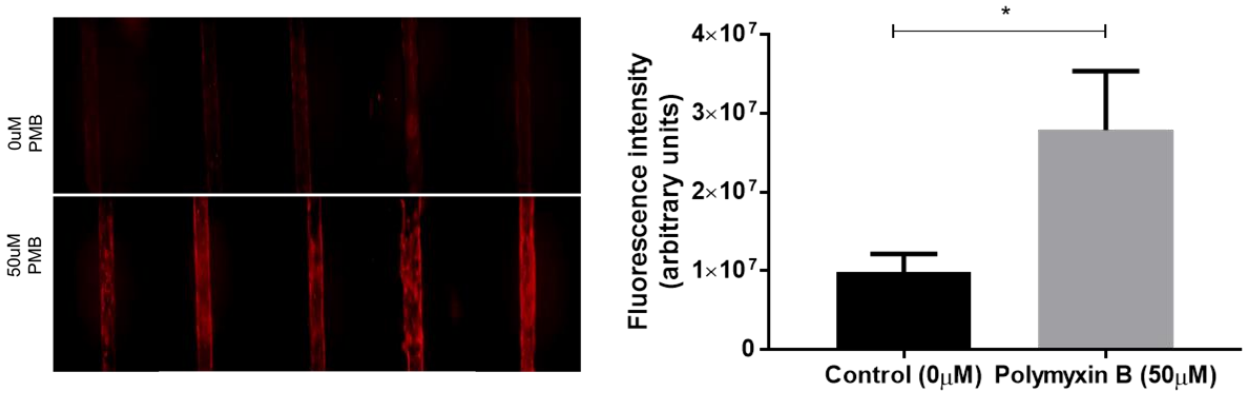

Figure 3. 4 - Quantification of cell-associated HMOX-1 displays significant induction in response to PMB exposure.

Using immunocytochemistry techniques, cell-associated HMOX-1 was quantified and compared across several donors revealing a significant induction ($P < 0.05$) for devices treated with 50 μM PMB relative to control. Values are reported as mean fluorescence intensity ± SD (* $P < 0.05$ ** $P < 0.01$ *** $P < 0.001$).

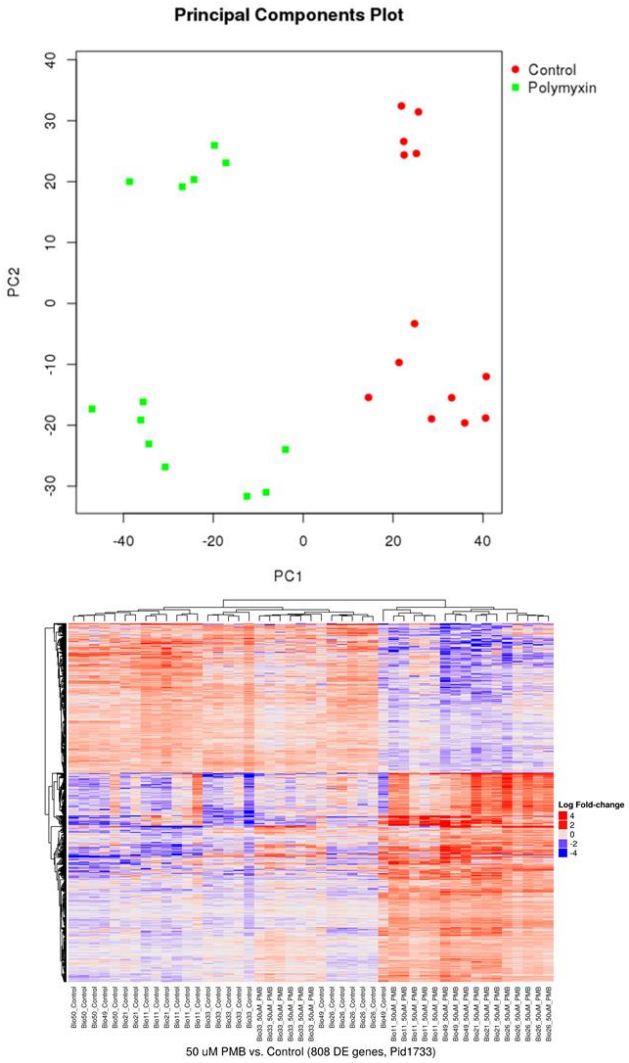

Figure 3. 5 - Principal component analysis (PCA) reveals observable transcriptional differences in response to PMB exposure, relative to control.

Using RNA-seq to observe the transcriptional response to PMB exposure, principal component analysis reveals tight clustering within respective groups of treatment (Control versus 50 µM PMB, lending evidence of high reproducibility between 3D kidney MPS systems, as well as a clear distinction between the treated and control (PC1) and between the individual donors (PC2). The heatmap visualizes the 808 differentially expressed genes in 50 uM PMB vs. Control, where genes are in rows and samples in columns, both of which are grouped according to the clustering results. Colors can be interpreted as the fold change from the mean expression of each gene.

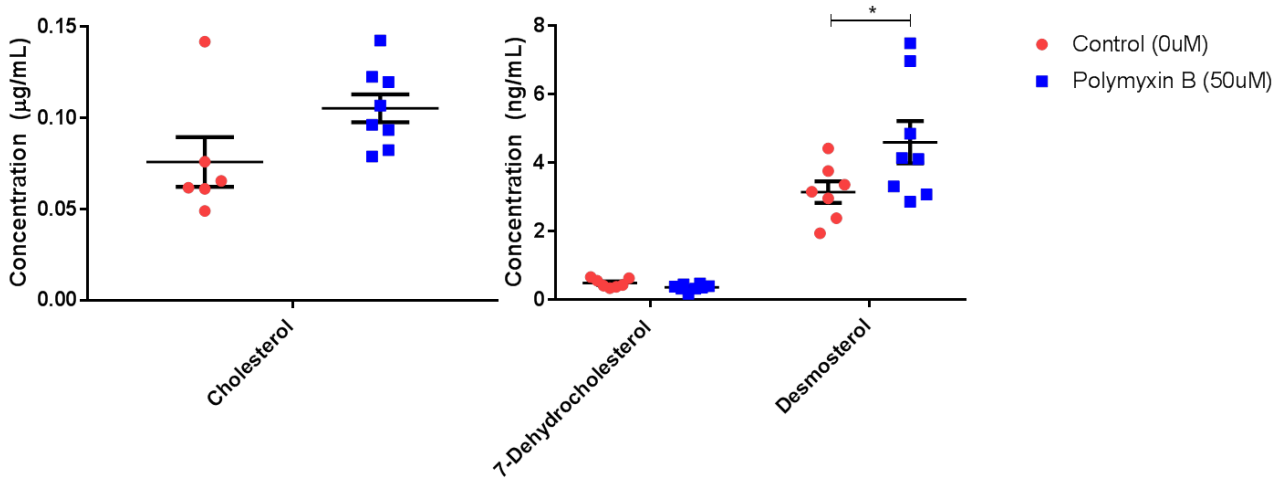

Figure 3. 6 - Quantification of cholesterol and cholesterol precursors in effluent of MPS.

Effluent from MPS, untreated (control) or exposed to PMB (50 µM) for 48 hours, was analyzed for cholesterol and cholesterol precursors including 7-dehydrocholesterol and desmosterol. While 7-dehydrocholesterol showed no apparent increase in effluent concentrations at 48 hours, desmosterol significantly increased at 48 hours ($P < 0.05$). In response to PMB exposure, cholesterol levels showed an observable increased at 48 hours and trended towards a significant difference ($P < 0.05$) when the high concentration outlier was not factored into the analysis (from $P = 0.73$ to $P = 0.07$). Values are reported as the mean ± SEM (* $P < 0.05$ ** $P < 0.01$ *** $P < 0.001$).

Group	EC_{50} [(95% confidence limits), μM]
Human Donor	
1	116.6 (83.8 – 162.2)
2	123 (99.3 –152.4)
3	93.1 (69.7 – 124.4)
4	45.7 (41.3 – 50.5)
Cell Line	
MDCK	389.1 (277.7 – 545.1)
LLCPK-1	246 (191.9 – 315.5)
HK-2	48.5 (42.3 –55.5)

Supplemental Table 3. 1 - PMB dosimetry reveals primary human PTECs to exhibit increased sensitivity to PMB-induced cytotoxicity relative to immortalized animal renal cell lines.

Comparing the sensitivity of primary human PTECs to immortalized animal/human cell lines, PMB dosimetry was investigated using 1:1 dilutions across ten different concentrations ranging from 0 μM to 1mM. After 48 hours of exposure, cell viability was measured for each concentration tested and EC_{50} values were reported as the concentration (μM) that decreased 50% of viable cells. Values in the parenthesis are lower and upper limits of the 95% confidence interval; n = 3.

Metallothionein Family

Gene	Gene Name	logFC	P. Value	False Discovery Rate
MT1G	Metallothionein 1G	2.62	1.19E-10	4.66E-08
MT1H	Metallothionein 1H	2.58	4.87E-08	7.12E-06
MT1M	Metallothionein 1M	2.23	1.18E-07	1.44E-05
MT1X	Metallothionein 1X	2.21	2.64E-11	1.25E-08
MT2A	Metallothionein 2A	1.82	1.38E-12	1.26E-09
MT1E	Metallothionein 1E	1.51	2.41E-11	1.18E-08
MT1F	Metallothionein 1F	1.47	1.85E-09	4.09E-07

Unfolded Protein Response

Gene	Gene Name	logFC	P. Value	False Discovery Rate
AMFR	autocrine motility factor receptor	-0.20	9.94E-01	1.00
ASK1	mitogen-activated protein kinase kinase kinase 5	0.27	8.11E-01	1.00
ATF4	activating transcription factor 4	0.22	9.67E-01	1.00
ATF6	activating transcription factor 6	0.01	1.00	1.00
BCL2	BCL2, apoptosis regulator	-0.43	4.80E-02	4.24E-01
BIP	heat shock protein family A (Hsp70) member 5	0.13	1.00	1.00
CALR	calreticulin	0.12	1.00	1.00
CANX	calnexin	0.12	1.00	1.00
CHOP	DNA damage inducible transcript 3	0.25	7.99E-01	1.00
EDEM	ER degradation enhancing alpha-mannosidase like protein 1	0.37	1.88E-01	1.00
EIF2α	eukaryotic translation initiation factor 2A	0.06	1.00	1.00
ERO1-Lβ	endoplasmic reticulum oxidoreductase 1 beta	-0.29	5.69E-01	1.00
GADD34	protein phosphatase 1 regulatory subunit 15A	1.18	3.66E-11	1.62E-08
GRP94	heat shock protein 90 beta family member 1	0.16	9.98E-01	1.00
HSPH1	heat shock protein family H (Hsp110) member 1	0.62	9.70E-06	5.12E-04
INSIG1	insulin induced gene 1	1.69	8.47E-18	3.88E-14
IRE1	endoplasmic reticulum to nucleus signaling 1	0.26	8.13E-01	1.00
JNK1	mitogen-activated protein kinase 8	-0.08	1.00	1.00
KAI1	CD82 molecule	0.60	8.87E-04	1.90E-02
MKK7	mitogen-activated protein kinase kinase 7	-0.08	1.00	1.00
NRF2	nuclear factor, erythroid 2 like 2	-0.03	1.00	1.00
OS9	OS9, endoplasmic reticulum lectin	-0.08	1.00	1.00
P58IPK	DnaJ heat shock protein family (Hsp40) member C3	0.05	1.00	1.00
PERK	eukaryotic translation initiation factor 2 alpha kinase 3	0.11	1.00	1.00
PPARγ	peroxisome proliferator activated receptor gamma	0.19	9.57E-01	1.00
SCAP	SREBF chaperone	-0.04	1.00	1.00
SEL1L	SEL1L ERAD E3 ligase adaptor subunit	-0.12	1.00	1.00
SYVN1	synoviolin 1	0.07	1.00	1.00

TRAF2	TNF receptor associated factor 2	0.26	7.99E-01	1.00
UBX	UBX domain protein 4	-0.12	1.00	1.00
VCP	valosin containing protein	0.22	9.97E-01	1.00
XBP1	X-box binding protein 1	0.26	9.19E-01	1.00

NRF2-mediated Oxidative Stress Response

Gene	Gene Name	logFC	P. Value	False Discovery Rate
AKR	aldo-keto reductase family 1 member A1	0.09	1.00	1.0
AKT	AKT serine/threonine kinase 1	0.23	9.91E-01	1.0
AOX1	aldehyde oxidase 1	0.32	5.17E-01	1.0
ASK1	mitogen-activated protein kinase kinase kinase 5	0.27	8.11E-01	1.0
ATF4	activating transcription factor 4	0.22	9.67E-01	1.0
BACH1	BTB domain and CNC homolog 1	0.05	1.00	1.0
c-Fos	Fos proto-oncogene, AP-1 transcription factor subunit	1.12	2.10E-04	6.04E-03
c-MAF	MAF bZIP transcription factor	-0.61	1.42E-02	1.68E-01
c-Raf	Raf-1 proto-oncogene, serine/threonine kinase	0.04	1.00	1.0
CAT	catalase	-0.38	2.13E-01	1.0
CBR1	carbonyl reductase 1	-0.08	1.00	1.0
CCT7	chaperonin containing TCP1 subunit 7	0.30	6.54E-01	1.0
CLPP	caseinolytic mitochondrial matrix peptidase proteolytic subunit	0.15	9.90E-01	1.0
CUL3	cullin 3	-0.04	1.00	1.0
EPHX1	epoxide hydrolase 1	-0.29	6.84E-01	1.0
ERK5	mitogen-activated protein kinase 7	0.03	1.00	1.0
ERP29	endoplasmic reticulum protein 29	0.02	1.00	1.0
FKBP5	FK506 binding protein 5	-0.06	9.96E-01	1.0
FRA1	FOS like 1, AP-1 transcription factor subunit	0.90	3.16E-05	1.35E-03
FTH1	ferritin heavy chain 1	0.32	5.06E-01	1.0
FTL	ferritin light chain	-0.25	8.51E-01	1.0
GCLC	glutamate-cysteine ligase catalytic subunit	0.13	1.00	1.0
GCLM	glutamate-cysteine ligase modifier subunit	0.21	9.59E-01	1.0
GSK3β	glycogen synthase kinase 3 beta	0.24	9.78E-01	1.0
GSR	glutathione-disulfide reductase	0.07	1.00	1.0
HERPUD 1	homocysteine inducible ER protein with ubiquitin like domain 1	0.02	1.00	1.0
HIP2	ubiquitin conjugating enzyme E2 K	0.03	1.00	1.0
HMOX-1	heme oxygenase 1	1.31	1.81E-18	1.82E-14
Jun	Jun proto-oncogene, AP-1 transcription factor subunit	0.71	4.12E-08	6.21E-06
KEAP1	kelch like ECH associated protein 1	0.09	1.00	1.0
MEK5	mitogen-activated protein kinase kinase 5	-0.33	4.80E-01	1.0
MEKK	mitogen-activated protein kinase kinase kinase 1	-0.25	9.52E-01	1.0
MRP1	ATP binding cassette subfamily C member 1	-0.18	1.00	1.0

MRP2	ATP binding cassette subfamily C member 2	0.25	6.32E-01	1.0
MRP4	ATP binding cassette subfamily C member 4	-0.27	8.92E-01	1.0
NRF2	nuclear factor, erythroid 2 like 2	-0.03	1.00	1.0
NRPB	ectodermal-neural cortex 1	0.42	1.32E-01	8.70E-01
p38MAPK	mitogen-activated protein kinase 14	0.08	1.00	1.0
PERK	eukaryotic translation initiation factor 2 alpha kinase 3	0.11	1.00	1.0
PMF-1	polyamine modulated factor 1	-0.46	2.92E-01	1.0
PPIB	peptidylprolyl isomerase B	0.22	9.73E-01	1.0
PRDX1	peroxiredoxin 1	0.51	6.38E-04	1.46E-02
PTPLAD1	3-hydroxyacyl-CoA dehydratase 3	0.00	1.00	1.0
Roc1	ring-box 1	0.09	9.96E-01	1.0
SQSTM1	sequestosome 1	0.51	3.77E-04	9.77E-03
SR-BI	scavenger receptor class B member 1	0.23	8.23E-01	1.0
STIP1	stress induced phosphoprotein 1	0.40	7.80E-02	6.08E-01
TAK1	mitogen-activated protein kinase kinase kinase 7	-0.11	1.00	1.0
TRXR1	thioredoxin reductase 1	0.73	2.90E-09	5.94E-07
TXN	thioredoxin	0.54	1.16E-03	2.37E-02
UB2R1	cell division cycle 34	0.11	1.00	1.0
UBB	ubiquitin B	0.25	9.51E-01	1.0
UbcM2	ubiquitin conjugating enzyme E2 E3	-0.09	1.00	1.0
UGT	solute carrier family 35 member A2	0.19	9.58E-01	1.0
USP14	ubiquitin specific peptidase 14	0.30	6.39E-01	1.0
VCP	valosin containing protein	0.22	9.97E-01	1.0

Superpathway of Cholesterol Biosynthesis

Gene	Gene Name	logFC	P. Value	False Discovery Rate
ABCA1	ATP binding cassette subfamily A member 1	-0.71	1.92E-04	5.7E-03
ACAT1	acetyl-CoA acetyltransferase 1	-0.265	8.04E-01	1.0
ACAT2	acetyl-CoA acetyltransferase 2	1.08	3.06E-11	1E-08
CYP51A1	cytochrome P450 family 51 subfamily A member 1	0.86	2.92E-12	2E-09
DHCR7	7-dehydrocholesterol reductase	0.94	6.29E-10	2E-07
DHCR24	24-dehydrocholesterol reductase	0.456	1.00E-02	1E-01
EBP	emopamil binding protein (sterol isomerase)	0.96	1.92E-09	4E-07
FDFT1	farnesyl-diphosphate farnesyltransferase 1	0.93	9.9E-13	1E-09
FDPS	farnesyl diphosphate synthase	1.14	2.16E-13	2E-10
GGPS1	geranylgeranyl diphosphate synthase 1	-0.021	1.0	1.0
HADHA	hydroxyacyl-CoA dehydrogenase trifunctional multienzyme complex subunit alpha	-0.019	1.0	1.0
HADHB	hydroxyacyl-CoA dehydrogenase trifunctional multienzyme complex subunit beta	-0.203	9.89E-01	1.0
HMGCR	3-hydroxy-3-methylglutaryl-CoA reductase	0.88	6.6E-12	4E-09

HMGCS1	3-hydroxy-3-methylglutaryl-CoA synthase 1	1.48	2.65E-18	2E-14
HSD17B7	hydroxysteroid 17-beta dehydrogenase 7	0.62	0.000279	8E-03
IDI1	isopentenyl-diphosphate delta isomerase 1	1.07	1.65E-12	1E-09
LBR	lamin B receptor	-0.154	9.96E-01	1.0
LSS	lanosterol synthase	0.60	8.02E-06	4E-04
MSMO1	methylsterol monooxygenase 1	1.24	2.39E-15	5E-12
MVD	mevalonate diphosphate decarboxylase	1.18	7.85E-11	3E-08
MVK	mevalonate kinase	0.252	8.18E-01	1.0
NSDHL	NAD(P) dependent steroid dehydrogenase-like	0.79	3.03E-06	2E-04
PMVK	phosphomevalonate kinase	0.291	6.52E-01	1.0
SC5D	sterol-C5-desaturase	0.50	0.00187	3E-02
SQLE	squalene epoxidase	0.93	2.07E-11	1E-08
TM7SF2	transmembrane 7 superfamily member 2	0.175	9.75E-01	1.0

Supplemental Table 3. 2 - Global transcriptional response to PMB exposure, relative to control, results in significant induction of injury response genes.

The following genes (blue shaded) were significantly different when cells were exposed to 50 µM PMB, relative to control, as indicated by $\log_2$-Fold Change (logFC) between the two treatment groups being compared, *P* value, and False Discovery Rate (FDR) which was the p-value adjusted for multiple testing (Benjamini & Hochberg's method). Specific pathways of interest included the metallothionein family, Unfolded protein response, NRF2-mediated Oxidative Stress Response, and Superpathway of Cholesterol Biosynthesis. The following genes (yellow shaded) are recognized genes that are associated with the NRF-2 Antioxidant Response.

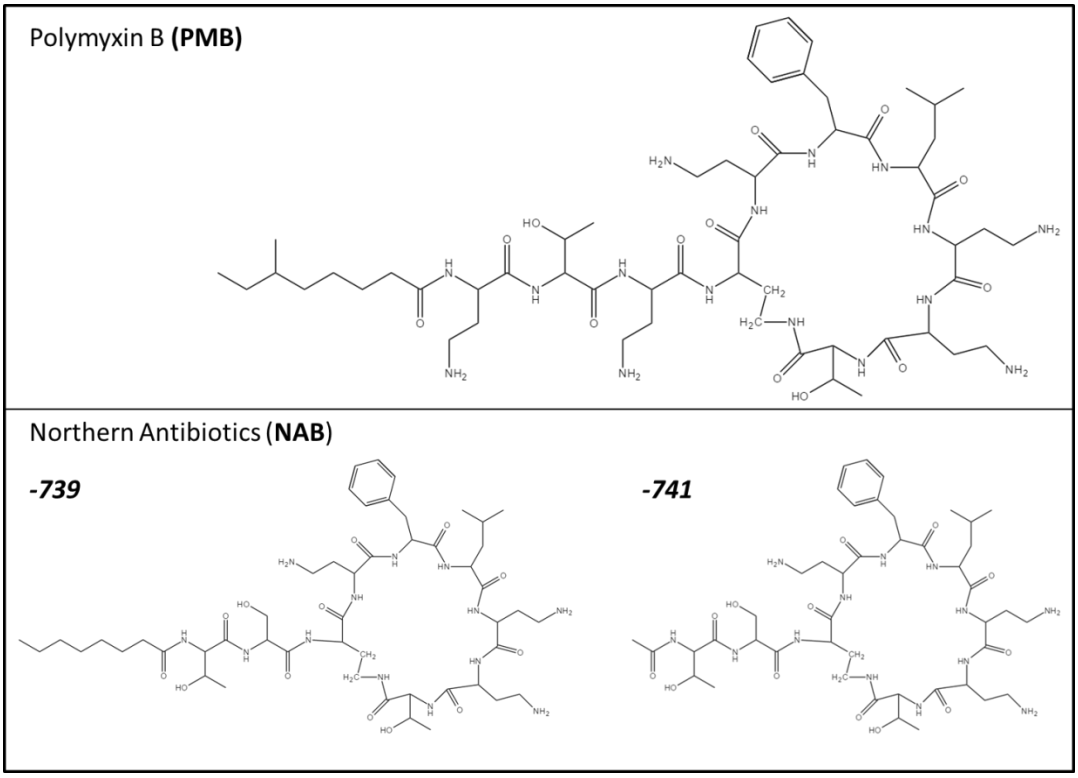

Supplemental Figure 3. 1 - Chemical structures of Polymyxin B (PMB) and Northern Antibiotics analogues (NAB739/741).

PMB is a polycationic decapeptide containing a heptapeptide ring, a linear tripeptide, and a fatty acid tail. Northern Antibiotics have developed polymyxin-analogues (NAB-739/-741), containing fewer cationic groups, that demonstrate retained biological activity and an improved safety profile.

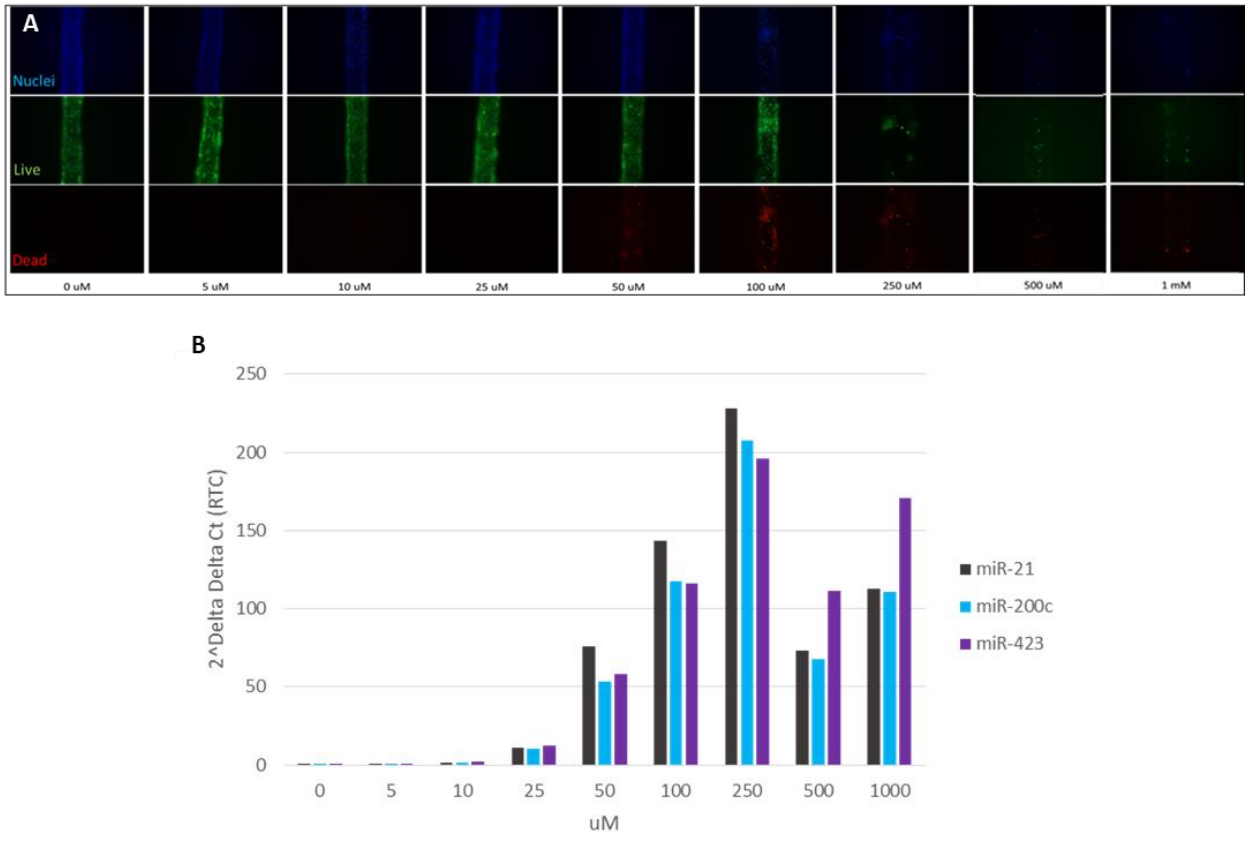

Supplemental Figure 3. 2 - PMB dosimetry in the 3D kidney MPS.

(A) PMB dosimetry was achieved in the 3D kidney MPS after 48 hours by dose-escalation from 0 µM to 1mM PMB. To visualize PMB-induced cytotoxicity, a Live/Dead cellular stain was used to show observable differences in viability (Green) and toxicity (red) with increasing concentrations to PMB. Any devices that were exposed to 250 M or higher resulted in severe cell death (as indicated by the red stain) and loss of tubule integrity. 50 µM PMB appeared to not only cause injury but retained an observable degree of viability to which 50 µM PMB was the fixed concentration to use in further experiments. **(B)** MPS effluents from the PMB-dosimetry experiment were analyzed for urinary miRNAs (miR-21, -200c, and -423) and showed observable accumulation in the effluent with increasing concentrations of PMB.

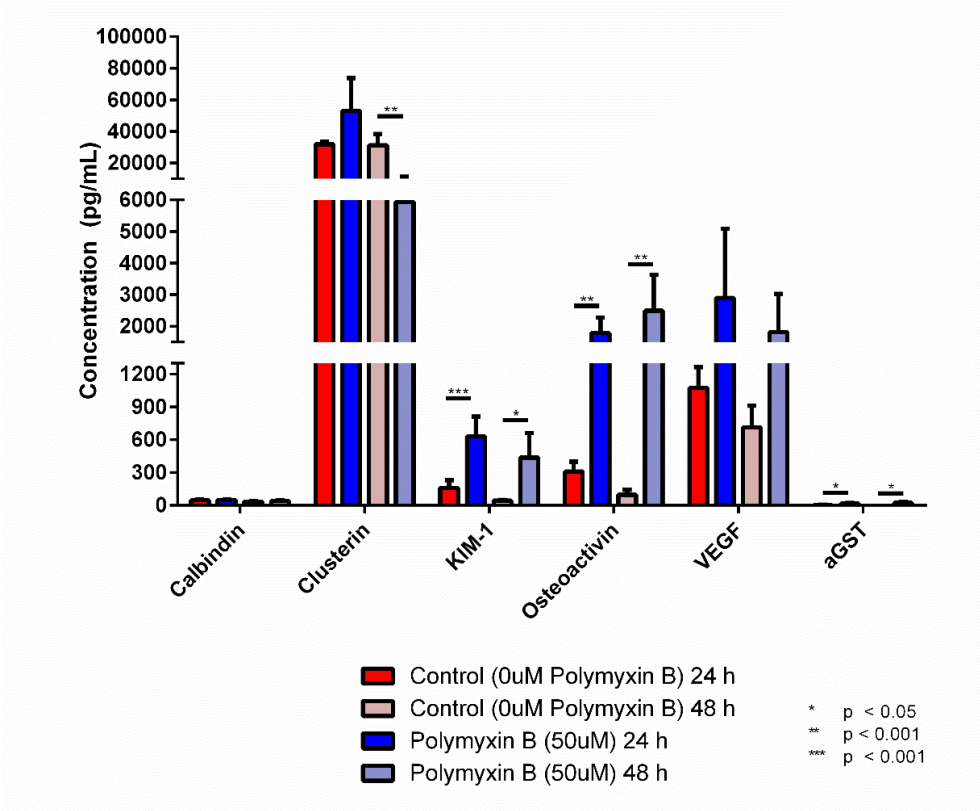

Supplemental Figure 3. 3 - Multiplex urinary-biomarker response to PMB-induced nephrotoxicity.

A multiplex approach was used to assess the concentration of multiple urinary kidney injury biomarkers (Osteoactivin, KIM-1, VEGF, and aGST) in MPS effluent. There was a significant difference between PMB treated MPS effluent and control MPS effluent for urinary biomarkers KIM-1, Osteoactivin, and aGST.

(* $P < 0.05$, ** , $P < 0.001$, ***, $P < 0.0001$, 2-tailed t-test)

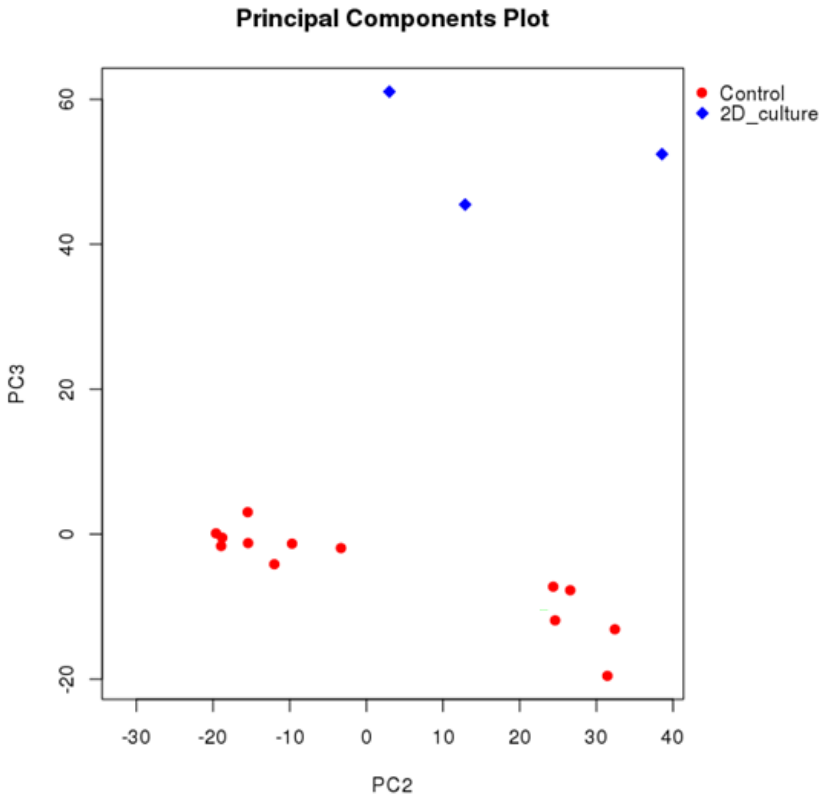

Supplemental Figure 3. 4 - PCA plot comparing PTEC culture conditions between 3D kidney MPS and 2D.

Principal component 2 (PC2) separates donors BIO11 and BIO21 from BIO26. Here we plot the second and third PCs to show that the 3D kidney MPS and 2D samples are separated on the third PC. The third principal component (PC3) clearly separated donors cultured in the 3D kidney MPS with their respective 2D cell culture indicating the significant role culture conditions play (2D versus 3D MPS).

Appendix I

Concise Review – Current and Emerging Biomarkers of Nephrotoxicity

The work presented in this chapter was published:

Current Opinion Toxicology. 2017 Jun; 4:16-21.

DOI: 10.1016/j.cotox.2017.03.002

Concise review: Current and emerging biomarkers of nephrotoxicity

Authors: Elijah J Weber[1], Jonathan Himmelfarb[2*] & Edward J Kelly[1*]

[1]Department of Pharmaceutics and [2]Kidney Research Institute, University of Washington, Seattle, WA, 98195

Keywords: Acute Kidney Injury, Biomarkers, Nephrotoxicity

*Co-Corresponding Authors

I.I Abstract

The kidney is a primary organ for filtration of the blood and elimination of drugs and xenobiotics. These active reabsorptive and secretory processes can result in acute kidney injury as a result of these concentrative properties. Classic measures of acute kidney injury are hampered by their ability to accurately assess function before irreversible damage has occurred. This review will discuss efforts to refine the clinical utility of standard biomarkers as well as the development of novel biomarkers of nephrotoxicity.

I.II Introduction

The kidneys receive approximately 25% of total cardiac blood flow and are responsible for the maintaining of circulatory fluid homeostasis while serving as a primary organ of xenobiotic elimination and detoxification. The functional filtration unit of the kidney is the renal nephron with approximately 1 million nephrons per kidney. There are three key functional components of the renal nephron: the passive filtration of the blood by the glomeruli, and both the active reabsorption and secretion of solutes via tubular epithelia. These tubular epithelia, particularly

the proximal tubule, are enriched with integral membrane proteins responsible for facilitated and active transport processes which have the potential to concentrate compounds within a cell to significantly higher levels than what is observed in circulation (*110*). Intracellular accumulation has been considered to be the primary driver behind xenobiotic-induced nephropathy leading to observable acute kidney injury (AKI), chronic kidney disease (CKD) and, with time, end-stage renal disease (ESRD) requiring the use of renal replacement therapy (RRT) as a method of disease intervention.

A current major challenge is the ability to accurately predict toxin-induced kidney injury, whether it be for existing prescription medications, clinical trials for new pharmaceuticals, or for risk assessment due to environmental exposures of xenobiotics. A particular clinical concern is for early detection of AKI. Classic criteria for the diagnosis of AKI include observing a decrease in the clearance of creatinine (detected via a rise in serum creatinine (sCr)), and/or oliguria, determined by measuring timed total urine output, and monitoring an increase in the circulation levels of blood urea nitrogen (BUN). While sCr, urine output, and BUN levels are considered a staple in the classification of kidney injury, by the time one typically observes changes in these measures, significant and potentially irreversible damage may have already occurred. In response to this concern, there has been a quest to identify new, more sensitive, biomarkers of AKI (*111*). The accuracy of predicting and identifying an early toxic event has been further improved with the discovery of novel urinary biomarkers, including measurements of miRNA and secreted proteins. The iterative improvement of nephrotoxic biomarkers will not only allow for an earlier detection of xenobiotic-induced kidney injury but also potentially reduce the likelihood of patient mortality through earlier intervention.

AKI definitions have been continually redefined over the past 10 years with an overall goal to increase the sensitivity and specificity of detection. In 2002, the Acute Dialysis Quality Initiative (ADQI) group defined the foundation of diagnosing AKI using the RIFLE (Risk, Injury, Failure, Loss, ESRD) classification, whose primary specific diagnostic biomarker of renal function was the use of sCr and BUN combined with urine output. Using a combination of these markers, severity of AKI was established by substantial increases in sCr and/or loss of urine output indicating progressive stages of sensitivity (Risk, Injury and Failure) and two clinical outcomes of specificity (Loss and End-stage renal disease) (*112, 113*). Further advancements to the definition of AKI were later made in 2005, by the AKIN (The Acute Kidney Injury Network) group, evaluating both the hydration of the patient at the time of diagnostic biomarker measurement as well as a refinement on the use of sCr determining GFR changes (*114*). Finally in 2012, KDIGO (Kidney Disease: Improving Global Outcomes) refined the definition of AKI by implementing both differences between RIFLE and AKIN into simplified stages of AKI defined as an increase in sCr ≥0.3 mg/dL (≥26.5 μmol/L) within 48 h; or an increase in sCr to ≥1.5 times baseline, which is known or presumed to have occurred within the prior 7 days or a urine volume of <0.5 mL/kg/h for 6 h (*115*). In 2014, Zeng et al. evaluated AKI incidence between the varying refinements of definitions of AKI using a retrospective cohort study. Results showed AKI incidence was highest according to the KDIGO definition (18.3%) followed by the AKIN (16.6%), and RIFLE (16.1%), definitions. Paralleled by additional studies, Zeng et al. observed AKI incidence associated with an increased rate of mortality and increased hospital costs (*116*).

In addition to defining AKI clinically, pathophysiology of drug/xenobiotic-induced AKI can be defined by measurable damage to site-specific segments of the nephron which include:

glomerular capillaries, mesangium, podocytes, parietal epithelial cells, proximal tubule, distal tubule, collecting ducts, and interstitium (*117-121*) [Figure 1]. There are a multitude of compounds that possess nephrotoxic properties which include: chemotherapeutics (cisplatin), antiretroviral therapeutics (tenofovir), analgesics (NSAIDs), contrast agents for imaging, heavy metal pollutant (cadmium), and some classes of antibiotics (aminoglycoside/polymyxin) (*122-126*).

Despite increased sensitivity to detecting clinical AKI, sCr and BUN response may be significantly delayed following kidney injury requiring the use of emerging urinary biomarkers to detect both early events of injury as well as segment-specific nephrotoxicity (*127*). In 2009, the Predictive Safety Testing Consortium (PSTC) released a biomarker qualification data submission indicating emerging urinary biomarkers, in addition to sCr and BUN, which include: urinary kidney injury molecule-1 (KIM-1), urinary beta2-microglobulin(B2M), urinary total protein, urinary albumin, urinary clusterin, urinary cystatin c (Cys C), and urinary trefoil factor 3 (TFF-3) in good laboratory practice rat toxicology studies to monitor xenobiotic-induced kidney injury (*128*). In a later report in 2014, the PSTC, with letters of support from the European Medicines Agency and Food and Drug Administration, encouraged further evaluation of emerging biomarkers including osteopontin (OPN) and neutrophil gelatinase-associated lipocalin (NGAL) (*129*).

This review will describe currently available biomarkers that are frequently used in preclinical/clinical investigations as well as emerging biomarkers of nephrotoxicity. It is important to note that, relative to the proximal tubule, segments of the renal nephron (glomerulus, distal tubule, collecting duct, etc.) are targets of xenobiotic-induced nephropathy as

well, yet their biomarker sensitivity and specificity profiles are limited and require ongoing investigations to identify traceable markers.

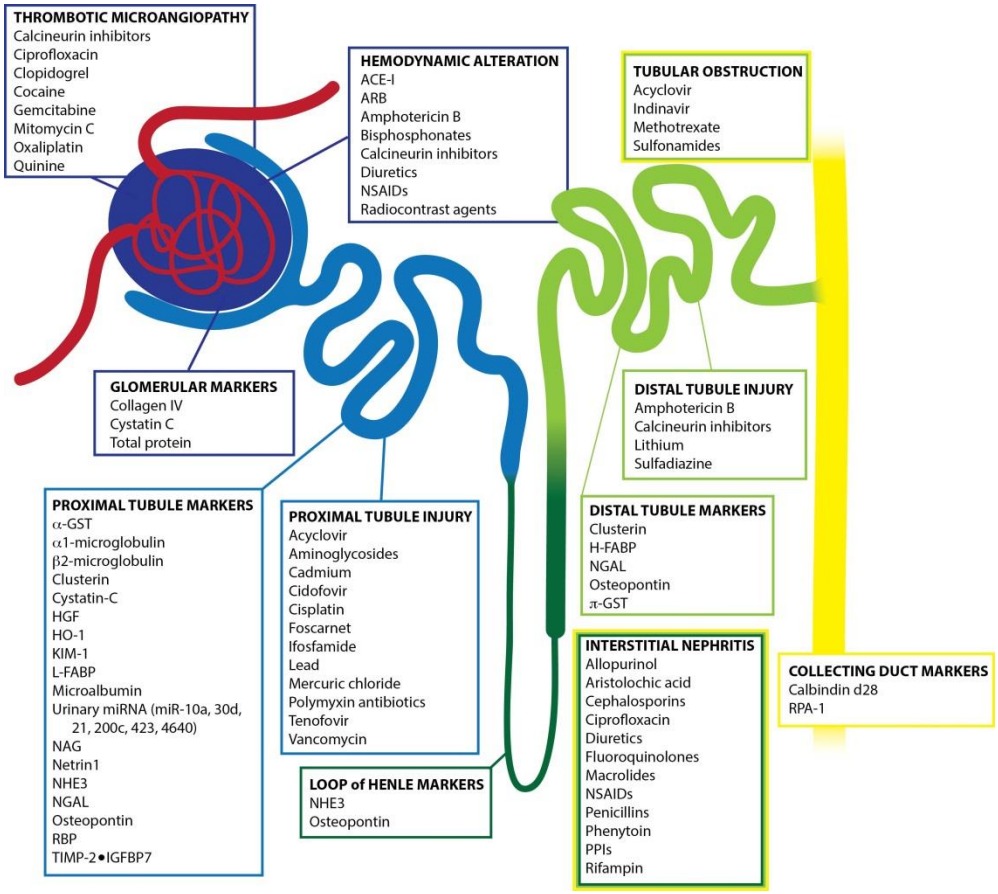

Appendix I. 1 - Diagram of renal nephron indicating toxicant, area of injury, and origin of biomarker.

A) Passive filtration is the first process achieved by the glomerulus where toxicant-induced AKI can result in thrombotic microangiopathy and/or hemodynamic alterations. B) In juxtaposition to the glomerulus, the proximal tubule is a primary location of toxicant-induced AKI resulting in proximal tubule injury and loss of integrity leading to downstream accumulation of biomarkers in the urine. C) The remaining tubule structures (Loop of Henle, Distal Tubule, Collecting Duct) are additional structures of the nephron that can become compromised upon toxicant-induced AKI resulting in interstitial nephritis and biomarker accumulation within the urine. (adapted from Casaret and Doull's Toxicology: The Basic Science of Poisons)

I.III Frequently investigated biomarkers of nephrotoxicity

I.III. a Kidney Injury Molecule-1 (KIM-1)

First discovered in rats as an upregulated protein in response to ischemia, KIM-1 is a type 1 transmembrane protein, containing immunoglobulin and mucin domains. In response to acute kidney injury, the N-terminal immunoglobulin and mucin ectodomain are cleaved from the apical surface of the proximal tubule and shed in the urine (*130*). KIM-1 is an excellent biomarker of AKI, as demonstrated in preclinical and clinical investigations, including a recent study by Pavkovic et al. evaluating KIM-1 as a urinary biomarker for drug-induced AKI in humans (*131*). Compared to healthy volunteers, Pavkovic et al. showed significant levels of KIM-1 (relative to urinary creatinine) in the urine of patients in two cohort studies who were or were not clinically diagnosed with AKI following either an overdose of acetaminophen or intraoperative cisplatin therapy, with resultant chronic interstitial nephritis (*82*). Furthermore, as demonstrated in a rat model, Luo et al. observed concentration-dependent gentamicin-induced renal injury leading to a significant induction of KIM-1 in the urine across multiple days. Additional findings showed significant differences of clinical biomarkers (BUN/sCr) only being observed at later points of collection (day 7) and at the highest concentration treated; when compared to KIM-1, these findings demonstrate the lack of early sensitivity and delayed response to detect acute kidney injury (*132*).

I.III.b Interleukin-18 (IL-18)

From the IL-1 cytokine family, interferon-γ-inducing factor (now recognized as interleukin-18, IL-18) is a proinflammatory cytokine that is activated and released upon cleavage via caspase 1. Primarily expressed in proximal tubule cells and intercalated renal cells (late distal convoluted tubule, connecting tubule, and the collecting duct), IL-18 has been shown to accumulate in the urine in response to acute kidney injury. In 2013, Zubowska et al. confirmed preclinical findings on the induction of IL-18 following nephropathy by observing a significant increase of IL-18 in the urine of children who were being treated with nephrotoxic chemotherapies (*133*). Additionally, a meta-analysis by Lin et al. analyzed 11 different studies with approximately 2800 people in total and observed a higher chance of early detection of AKI using IL-18 when compared to sCr (*134*). Furthermore, in a simulated clinical trial of AKI using data obtained from prospective cohort study of patients with at least 1 risk factor for AKI, Parikh et al. observed a potential increase in proportion of patients experiencing AKI following inclusion of urinary IL-18 monitoring (*135*).

I.III. c Neutrophil Gelatinase-associated Lipocalin (NGAL)

NGAL is a small protease-resistant secreted protein filtered by the glomerulus and extensively reabsorbed by the proximal tubule. The utility of NGAL as a predictive biomarker for AKI was first suggested from a study by Mishra et al. where increases in both transcripts and protein were observed in mice in response to renal ischemia (*136*). Tubular injury, reflecting a decrease in NGAL reabsorption and accumulation in the urine, has been demonstrated in a number of studies including cisplatin-induced nephrotoxicity in mice. Mishra et al. observed cisplatin-induced tubule cell necrosis and apoptosis in addition to rapid induction of NGAL in both tubule epithelial cells as well as an accumulation and detection of NGAL in the urine just 3 hours after

dosing (*137*). Luo et al. later confirmed the significant induction of NGAL as a nephrotoxicity biomarker in both a dose- and time-dependency with gentamicin treated rats. However, clinical examples reveal an uncertainty when using NGAL as a urinary biomarker of cyclosporine A (CsA) treatment for children with nephrotic syndrome (*132*). Gacka et al. concluded that NGAL cannot be used alone as a marker of cyclosporine A-nephrotoxicity but has potential benefits when monitoring nephrotoxicity in a chronic setting (*138*). In contrast to CsA studies, a multicenter prospective cohort study by Nickolas et al. showed that urinary NGAL was significantly better at diagnosing intrinsic AKI compared to other biomarkers (sCr, KIM-1, IL-18, FABP, CysC) and more effective in predicting increasing RIFLE classes (*139*).

I.III.d Liver-type Fatty Acid-binding Protein (L-FABP)

Primarily located in the both the convoluted and straight segments of the proximal tubules, the liver-type fatty acid-binding protein (L-FABP) binds long-chain fatty acids (LCFA) and transports them for β-oxidation (in mitochondria/peroxisomes). Using established human FABP transgenic mice, Matsui et al. observed a significant induction of L-FABP in the proximal tubules following exposure to aristolochic acid, a carcinogenic plant alkaloid with known nephrotoxicity (*140*). Significant induction of FABP was observed for both mRNA and protein, with concomitantly increased urinary levels when compared to control mice. Additional findings by Jabłonowska et al. showed statistically higher concentrations of urinary L-FABP (normalized to creatinine) in HIV-infected individuals receiving antiretroviral therapy compared to healthy controls (*141*).

I.IV. Novel Biomarkers of AKI

I.IV.a Urine Tissue Inhibitor of Metalloproteinase 2 and Insulin-like Growth Factor Binding Protein 7 [TIMP-2 - IGFBP7]

Expressed in renal tubular cells, TIMP-2 and IGFBP7 are G1 cell-cycle arrest proteins induced as a consequence of AKI. TIMP-2 is an inhibitor of matrix metalloproteinase activity while IGFBP7 is a regulator of IGF signaling. In two separate multicenter observational studies (Discovery and Validation) of critically ill patients at risk for AKI, Kashani et al. observed significantly elevated urinary IGFBP7 and TIMP-2 when stratifying AKI risk compared to other urinary biomarkers of AKI (NGAL, CysC, KIM-1, IL-18, pi-GST, FABP) (*142*). Additional clinical cohort studies by Bihorac et al. and Hoste et al. defined cutoff values of urinary [TIMP-2 ● IGFBP7] improving the identification of patients at high risk of AKI (*143, 144*).

I.IV.b Myo-inositol oxygenase (MIOX)

Expressed extensively in the proximal tubule, myo-inositol oxygenase (MIOX) catabolizes glucose intermediates (myo-inositol) which enter the pentose phosphate pathway. Additionally, MIOX plays a critical role in antioxidant and oxidant responses regulated by Nrf2 (*145*). *In vitro* studies show MIOX overexpression leads to enhanced generation of ROS in the presence of cisplatin (*146*). Dutta et al. observed, using both MIOX null and overexpressing mice, that MIOX null mice are resistant to cisplatin-induced nephrotoxicity whereas MIOX overexpressing mice displayed enhanced injury (*147*). In work by Gaut et al. investigators developed an immunoassay to detect plasma MIOX as a biomarker of AKI in both animal and human species. Plasma levels of MIOX were significantly higher and detected 54 hours earlier than creatinine in

mice experiencing AKI as well as critically ill patients diagnosed with AKI compared to patients without AKI (*148*).

I.IV.c Heme oxygenase-1 (HO-1)

Responsible for the degradation of heme via conversion to biliverdin, HO-1 is induced in the proximal tubule and exerts cytoprotective effects in response to renal injury. In similarity to MIOX, HO-1 cytoprotective antioxidant activity is also regulated by Nrf2 (*149*). Earlier reports show HO-1 to be nephro-protective as evidenced by induction in response to cisplatin-induced AKI using a rat model (*150*). Using a mouse model to assess four different models of AKI (ischemia/reperfusion, glycerol-induced rhabdomyolysis, cisplatin nephrotoxicity, and bilateral ureteral obstruction), Zager et al. observed significant increases of HO-1 gene expression and therefore increased concentrations in both the plasma and urine 4 hours later. These findings were then supported with a clinical investigation revealing patients with AKI to have significantly higher levels of both plasma and urine HO-1 compared to patients without AKI, patients with CKD, or patients with ESRD (*151*). More recently, using a high throughput approach for predictive nephrotoxicity assessment, Adler et al. screened a panel of over 40 nephrotoxicants using primary human proximal tubular epithelial cells and showed HO-1 to significantly upregulate after exposure at the mRNA and protein level (*81*).

I.IV.d Urinary miRNA

MicroRNAs are endogenous short (~22 nucleotides) RNA molecules that regulate expression primarily via inhibition of mRNA translation, with lesser effects on transcript stability. Because extracellular miRNAs are stable at room temperature and changes in pH coupled with the ability to amplify these targets with PCR, miRNAs have the potential to serve as excellent urinary

biomarkers. For example, Wang et al. observed a significant induction of urinary miR-10a and miR-30d in mice experiencing renal ischemia reperfusion or streptozotocin-induced renal injury. The investigators further evidenced the mouse model findings with a cohort of healthy individuals and patients experiencing focal segmental glomerulosclerosis (FSGS); showing FSGS patients to have significantly elevated levels of urinary miR-10a and miR-30d (*152*). Additionally, Ramachandran et al. identified 4 miRNAs (miR-21, 200c, 423, 4640) significantly different between cohort groups of patients with AKI and healthy volunteers (*153*). Furthermore, Pavkovic et al. observed statistically significant elevated concentrations in urinary miRNA (miR-21, 423, and 200c) and KIM-1 in patients who were diagnosed with AKI following either an overdose of acetaminophen or intraoperative cisplatin therapy (*82*).

I.V Concluding remarks and future directions

To achieve early diagnosis and enhanced detection of toxin-induced AKI, continual refinement of established biomarkers coupled with identification and implementation of novel biomarkers is necessary. The work of Adler et al. identified HO-1 as a better *in vitro* biomarker of AKI in primary proximal tubule epithelial cells in both traditional 2D cultures as well as within a novel 3D system that recapitulates the proximal tubule (*81*). The clinical utility of HO-1 as a biomarker of nephrotoxicity is limited however, as it is ubiquitously expressed. But, the use of 3D microphysiological models of the proximal tubule will facilitate identification of novel tubule-specific biomarkers of nephrotoxicity (*89*). While technological advancements are improving to increase both sensitivity and specificity of biomarkers, there remains a critical need for the implementation of diverse approaches that span *in vitro*, *in vivo*, and clinical investigations. In summary, early detection of AKI should be the primary goal of clinicians and drug developers,

as AKI progression to CKD is extremely costly, potentially fatal to the patient, and can halt new drug development in clinical trials unless proper diagnostic tools are available.

I.VI Acknowledgements

We would like to express our thanks to Dr. Catherine M. Lockhart for expert graphical illustration support.

References of special interest (18, 27, 34 & 44) / References of outstanding interest (6, 19 & 23)

References

1. J. L. Zhuo, X. C. Li, Proximal nephron. *Compr Physiol* **3**, 1079-1123 (2013).
2. S. Y. Chang, E. J. Weber, K. V. Ness, D. L. Eaton, E. J. Kelly, Liver and Kidney on Chips: Microphysiological Models to Understand Transporter Function. *Clinical pharmacology and therapeutics* **100**, 464-478 (2016).
3. D. Gartzke, G. Fricker, Establishment of optimized MDCK cell lines for reliable efflux transport studies. *J Pharm Sci* **103**, 1298-1304 (2014).
4. K. Kuteykin-Teplyakov, C. Luna-Tortos, K. Ambroziak, W. Loscher, Differences in the expression of endogenous efflux transporters in MDR1-transfected versus wildtype cell lines affect P-glycoprotein mediated drug transport. *Br J Pharmacol* **160**, 1453-1463 (2010).
5. M. J. Ryan *et al.*, HK-2: An immortalized proximal tubule epithelial cell line from normal adult human kidney. *Kidney International* **45**, 48-57 (1994).
6. S. E. Jenkinson *et al.*, The limitations of renal epithelial cell line HK-2 as a model of drug transporter expression and function in the proximal tubule. *Pflugers Arch* **464**, 601-611 (2012).
7. C. J. Detrisac, M. A. Sens, A. J. Garvin, S. S. Spicer, D. A. Sens, Tissue culture of human kidney epithelial cells of proximal tubule origin. *Kidney International* **25**, 383-390 (1984).
8. C. D. Brown *et al.*, Characterisation of human tubular cell monolayers as a model of proximal tubular xenobiotic handling. *Toxicology and applied pharmacology* **233**, 428-438 (2008).
9. H. D. Humes, The bioartificial renal tubule: prospects to improve supportive care in acute renal failure. *Ren Fail* **18**, 405-408 (1996).
10. S. M. MacKay, A. J. Funke, D. A. Buffington, H. D. Humes, Tissue engineering of a bioartificial renal tubule. *ASAIO J* **44**, 179-183 (1998).
11. H. D. Humes, S. M. MacKay, A. J. Funke, D. A. Buffington, Tissue engineering of a bioartificial renal tubule assist device: in vitro transport and metabolic characteristics. *Kidney international* **55**, 2502-2514 (1999).
12. H. D. Humes *et al.*, Initial clinical results of the bioartificial kidney containing human cells in ICU patients with acute renal failure. *Kidney international* **66**, 1578-1588 (2004).
13. L. B. Rice, Federal funding for the study of antimicrobial resistance in nosocomial pathogens: no ESKAPE. *J Infect Dis* **197**, 1079-1081 (2008).
14. H. W. Boucher *et al.*, 10 x '20 Progress--development of new drugs active against gram-negative bacilli: an update from the Infectious Diseases Society of America. *Clin Infect Dis* **56**, 1685-1694 (2013).
15. H. W. Boucher *et al.*, Bad bugs, no drugs: no ESKAPE! An update from the Infectious Diseases Society of America. *Clin Infect Dis* **48**, 1-12 (2009).
16. L. L. Ling *et al.*, A new antibiotic kills pathogens without detectable resistance. *Nature* **517**, 455-459 (2015).
17. C. A. Mendes, E. A. Burdmann, [Polymyxins - review with emphasis on nephrotoxicity]. *Revista da Associacao Medica Brasileira* **55**, 752-759 (2009).
18. M. Vaara, T. Vaara, Structure-activity studies on novel polymyxin derivatives that carry only three positive charges. *Peptides* **31**, 2318-2321 (2010).
19. A. C. Gales, R. N. Jones, H. S. Sader, Global assessment of the antimicrobial activity of polymyxin B against 54 731 clinical isolates of Gram-negative bacilli: report from the SENTRY antimicrobial surveillance programme (2001-2004). *Clin Microbiol Infect* **12**, 315-321 (2006).
20. J. P. Ouderkirk, J. A. Nord, G. S. Turett, J. W. Kislak, Polymyxin B Nephrotoxicity and Efficacy against Nosocomial Infections Caused by Multiresistant Gram-Negative Bacteria. *Antimicrobial Agents and Chemotherapy* **47**, 2659-2662 (2003).

21. M. M. Mostardeiro, C. A. Pereira, A. R. Marra, J. O. Pestana, L. F. Camargo, Nephrotoxicity and efficacy assessment of polymyxin use in 92 transplant patients. *Antimicrob Agents Chemother* **57**, 1442-1446 (2013).
22. L. B. Neiva *et al.*, [Nephrotoxicity of polymyxin B: experimental study in cells and implications for nursing practice]. *Revista da Escola de Enfermagem da U S P* **48**, 272-277 (2014).
23. M. A. Azad *et al.*, Polymyxin B induces apoptosis in kidney proximal tubular cells. *Antimicrob Agents Chemother*, (2013).
24. C. Dai, J. Li, S. Tang, J. Li, X. Xiao, Colistin-induced nephrotoxicity in mice involves the mitochondrial, death receptor, and endoplasmic reticulum pathways. *Antimicrob Agents Chemother* **58**, 4075-4085 (2014).
25. T. V. Magee *et al.*, Discovery of Dap-3 polymyxin analogues for the treatment of multidrug-resistant Gram-negative nosocomial infections. *J Med Chem* **56**, 5079-5093 (2013).
26. T. M. DesRochers, L. Suter, A. Roth, D. L. Kaplan, Bioengineered 3D human kidney tissue, a platform for the determination of nephrotoxicity. *PLoS One* **8**, e59219 (2013).
27. K. M. Morrissey, S. L. Stocker, M. B. Wittwer, L. Xu, K. M. Giacomini, Renal transporters in drug development. *Annual review of pharmacology and toxicology* **53**, 503-529 (2013).
28. T. Ichimura *et al.*, Kidney injury molecule-1 is a phosphatidylserine receptor that confers a phagocytic phenotype on epithelial cells. *J Clin Invest* **118**, 1657-1668 (2008).
29. A. Tourovskaia, M. Fauver, G. Kramer, S. Simonson, T. Neumann, Tissue-engineered microenvironment systems for modeling human vasculature. *Experimental biology and medicine* **239**, 1264-1271 (2014).
30. C. E. Alpers, K. L. Hudkins, P. Pritzl, R. J. Johnson, Mechanisms of clearance of immune complexes from peritubular capillaries in the rat. *Am J Pathol* **139**, 855-867 (1991).
31. Y. Itoh, A. Ezawa, K. Kikuchi, Y. Tsuruta, T. Niwa, Protein-bound uremic toxins in hemodialysis patients measured by liquid chromatography/tandem mass spectrometry and their effects on endothelial ROS production. *Anal Bioanal Chem* **403**, 1841-1850 (2012).
32. L. Liu *et al.*, Vectorial transport of enalapril by Oatp1a1/Mrp2 and OATP1B1 and OATP1B3/MRP2 in rat and human livers. *J Pharmacol Exp Ther* **318**, 395-402 (2006).
33. J. G. Blackburn, D. J. Hazen-Martin, C. J. Detrisac, D. A. Sens, Electrophysiology and ultrastructure of cultured human proximal tubule cells. *Kidney international* **33**, 508-516 (1988).
34. C. J. Lote, *Principles of renal physiology*. (Kluwer Academic, Dordrecht ; London, ed. 4th, 2000), pp. x, 203 p.
35. E. J. Kelly *et al.*, Innovations in preclinical biology: ex vivo engineering of a human kidney tissue microperfusion system. *Stem Cell Res Ther* **4 Suppl 1**, S17 (2013).
36. B. M. Brenner, F. C. Rector, *Brenner and Rector's the Kidney*. (Saunders Elsevier, 2008).
37. S. Wickham, M. B. West, P. F. Cook, M. H. Hanigan, Gamma-glutamyl compounds: substrate specificity of gamma-glutamyl transpeptidase enzymes. *Analytical biochemistry* **414**, 208-214 (2011).
38. V. Vallon *et al.*, SGLT2 mediates glucose reabsorption in the early proximal tubule. *J Am Soc Nephrol* **22**, 104-112 (2011).
39. M. G. Vander Heiden, L. C. Cantley, C. B. Thompson, Understanding the Warburg effect: the metabolic requirements of cell proliferation. *Science* **324**, 1029-1033 (2009).
40. J. L. Omdahl, H. A. Morris, B. K. May, Hydroxylase enzymes of the vitamin D pathway: expression, function, and regulation. *Annu Rev Nutr* **22**, 139-166 (2002).
41. Z. Wang *et al.*, Simultaneous measurement of plasma vitamin D(3) metabolites, including 4beta,25-dihydroxyvitamin D(3), using liquid chromatography-tandem mass spectrometry. *Analytical biochemistry* **418**, 126-133 (2011).

42. K. I. Inui, S. Masuda, H. Saito, Cellular and molecular aspects of drug transport in the kidney. *Kidney international* **58**, 944-958 (2000).
43. K. J. Jang *et al.*, Human kidney proximal tubule-on-a-chip for drug transport and nephrotoxicity assessment. *Integrative biology : quantitative biosciences from nano to macro* **5**, 1119-1129 (2013).
44. P. L. Smith, D. A. Buffington, H. D. Humes, Kidney epithelial cells. *Methods in enzymology* **419**, 194-207 (2006).
45. L. H. Lash, D. A. Putt, H. Cai, Membrane transport function in primary cultures of human proximal tubular cells. *Toxicology* **228**, 200-218 (2006).
46. J. Jansen *et al.*, Human proximal tubule epithelial cells cultured on hollow fibers: living membranes that actively transport organic cations. *Scientific reports* **5**, 16702 (2015).
47. C. M. Schophuizen *et al.*, Development of a living membrane comprising a functional human renal proximal tubule cell monolayer on polyethersulfone polymeric membrane. *Acta biomaterialia* **14**, 22-32 (2015).
48. S. Kim, S. Takayama, Organ-on-a-chip and the kidney. *Kidney research and clinical practice* **34**, 165-169 (2015).
49. A. Maeshima, H. Sakurai, S. K. Nigam, Adult kidney tubular cell population showing phenotypic plasticity, tubulogenic capacity, and integration capability into developing kidney. *J Am Soc Nephrol* **17**, 188-198 (2006).
50. E. Martinez, E. Engel, J. A. Planell, J. Samitier, Effects of artificial micro- and nano-structured surfaces on cell behaviour. *Annals of anatomy = Anatomischer Anzeiger : official organ of the Anatomische Gesellschaft* **191**, 126-135 (2009).
51. M. Thery, Micropatterning as a tool to decipher cell morphogenesis and functions. *Journal of cell science* **123**, 4201-4213 (2010).
52. D. E. Discher, P. Janmey, Y. L. Wang, Tissue cells feel and respond to the stiffness of their substrate. *Science* **310**, 1139-1143 (2005).
53. A. J. Engler, S. Sen, H. L. Sweeney, D. E. Discher, Matrix elasticity directs stem cell lineage specification. *Cell* **126**, 677-689 (2006).
54. I. Maschmeyer *et al.*, A four-organ-chip for interconnected long-term co-culture of human intestine, liver, skin and kidney equivalents. *Lab Chip* **15**, 2688-2699 (2015).
55. G. Ligresti *et al.*, A Novel Three-Dimensional Human Peritubular Microvascular System. *J Am Soc Nephrol* **27**, 2370-2381 (2016).
56. P. J. Bergen *et al.*, Polymyxin combinations: pharmacokinetics and pharmacodynamics for rationale use. *Pharmacotherapy* **35**, 34-42 (2015).
57. D. R. Storm, K. S. Rosenthal, P. E. Swanson, Polymyxin and related peptide antibiotics. *Annu Rev Biochem* **46**, 723-763 (1977).
58. T. Velkov, K. D. Roberts, R. L. Nation, P. E. Thompson, J. Li, Pharmacology of polymyxins: new insights into an 'old' class of antibiotics. *Future Microbiol* **8**, 711-724 (2013).
59. A. Clausell *et al.*, Gram-negative outer and inner membrane models: insertion of cyclic cationic lipopeptides. *J Phys Chem B* **111**, 551-563 (2007).
60. M. E. Falagas, P. I. Rafailidis, D. K. Matthaiou, Resistance to polymyxins: Mechanisms, frequency and treatment options. *Drug Resist Updat* **13**, 132-138 (2010).
61. M. E. Falagas, S. K. Kasiakou, Toxicity of polymyxins: a systematic review of the evidence from old and recent studies. *Crit Care* **10**, R27 (2006).
62. C. J. Kubin *et al.*, Incidence and predictors of acute kidney injury associated with intravenous polymyxin B therapy. *J Infect* **65**, 80-87 (2012).
63. K. Abdelraouf *et al.*, Characterization of polymyxin B-induced nephrotoxicity: implications for dosing regimen design. *Antimicrob Agents Chemother* **56**, 4625-4629 (2012).

64. B. Yun *et al.*, Imaging the distribution of polymyxins in the kidney. *J Antimicrob Chemother* **70**, 827-829 (2015).
65. A. M. Sandri *et al.*, Population pharmacokinetics of intravenous polymyxin B in critically ill patients: implications for selection of dosage regimens. *Clin Infect Dis* **57**, 524-531 (2013).
66. X. Lu *et al.*, Human oligopeptide transporter 2 (PEPT2) mediates cellular uptake of polymyxins. *J Antimicrob Chemother* **71**, 403-412 (2016).
67. P. Manchandani *et al.*, Role of Renal Drug Exposure in Polymyxin B-Induced Nephrotoxicity. *Antimicrob Agents Chemother* **61**, (2017).
68. F. E. A. Ali *et al.*, Pharmacokinetics of novel antimicrobial cationic peptides NAB 7061 and NAB 739 in rats following intravenous administration. *Journal of Antimicrobial Chemotherapy* **64**, 1067-1070 (2009).
69. M. P. Mingeot-Leclercq, P. M. Tulkens, S. Denamur, T. Vaara, M. Vaara, Novel polymyxin derivatives are less cytotoxic than polymyxin B to renal proximal tubular cells. *Peptides* **35**, 248-252 (2012).
70. M. Vaara, Novel derivatives of polymyxins. *J Antimicrob Chemother* **68**, 1213-1219 (2013).
71. M. Vaara *et al.*, Novel polymyxin derivatives carrying only three positive charges are effective antibacterial agents. *Antimicrob Agents Chemother* **52**, 3229-3236 (2008).
72. M. Vaara, H. S. Sader, P. R. Rhomberg, R. N. Jones, T. Vaara, Antimicrobial activity of the novel polymyxin derivative NAB739 tested against Gram-negative pathogens. *J Antimicrob Chemother* **68**, 636-639 (2013).
73. M. Vaara, T. Vaara, The novel polymyxin derivative NAB739 is remarkably less cytotoxic than polymyxin B and colistin to human kidney proximal tubular cells. *Int J Antimicrob Agents* **41**, 292-293 (2013).
74. C. Vingsbo Lundberg, T. Vaara, N. Frimodt-Moller, M. Vaara, Novel polymyxin derivatives are effective in treating experimental Escherichia coli peritoneal infection in mice. *J Antimicrob Chemother* **65**, 981-985 (2010).
75. J. T. Babic, P. Manchandani, K. R. Ledesma, V. H. Tam, Evaluation of Urinary KIM-1 for Prediction of Polymyxin B-Induced Nephrotoxicity. *Antimicrob Agents Chemother*, (2017).
76. V. Bailly *et al.*, Shedding of kidney injury molecule-1, a putative adhesion protein involved in renal regeneration. *J Biol Chem* **277**, 39739-39748 (2002).
77. W. K. Han, V. Bailly, R. Abichandani, R. Thadhani, J. V. Bonventre, Kidney Injury Molecule-1 (KIM-1): a novel biomarker for human renal proximal tubule injury. *Kidney Int* **62**, 237-244 (2002).
78. L. Yang *et al.*, KIM-1-mediated phagocytosis reduces acute injury to the kidney. *J Clin Invest* **125**, 1620-1636 (2015).
79. K. L. Pellegrini *et al.*, Application of small RNA sequencing to identify microRNAs in acute kidney injury and fibrosis. *Toxicol Appl Pharmacol* **312**, 42-52 (2016).
80. J. Saikumar *et al.*, Expression, circulation, and excretion profile of microRNA-21, -155, and -18a following acute kidney injury. *Toxicol Sci* **129**, 256-267 (2012).
81. M. Adler *et al.*, A Quantitative Approach to Screen for Nephrotoxic Compounds In Vitro. *J Am Soc Nephrol* **27**, 1015-1028 (2016).
82. M. Pavkovic *et al.*, Detection of Drug-Induced Acute Kidney Injury in Humans Using Urinary KIM-1, miR-21, -200c, and -423. *Toxicol Sci* **152**, 205-213 (2016).
83. M. Pavkovic, V. S. Vaidya, MicroRNAs and drug-induced kidney injury. *Pharmacol Ther* **163**, 48-57 (2016).
84. R. H. Jenkins *et al.*, miR-192 induces G2/M growth arrest in aristolochic acid nephropathy. *Am J Pathol* **184**, 996-1009 (2014).
85. H. H. Chen *et al.*, Urinary miR-16 transactivated by C/EBPbeta reduces kidney function after ischemia/reperfusion-induced injury. *Sci Rep* **6**, 27945 (2016).

86. M. Cardenas-Gonzalez *et al.*, Identification, Confirmation, and Replication of Novel Urinary MicroRNA Biomarkers in Lupus Nephritis and Diabetic Nephropathy. *Clin Chem* **63**, 1515-1526 (2017).
87. M. A. Azad *et al.*, Major pathways of polymyxin-induced apoptosis in rat kidney proximal tubular cells. *Antimicrob Agents Chemother* **59**, 2136-2143 (2015).
88. M. A. Azad *et al.*, Significant accumulation of polymyxin in single renal tubular cells: a medicinal chemistry and triple correlative microscopy approach. *Anal Chem* **87**, 1590-1595 (2015).
89. E. J. Weber *et al.*, Development of a microphysiological model of human kidney proximal tubule function. *Kidney Int* **90**, 627-637 (2016).
90. Z. Korade *et al.*, The Effect of Small Molecules on Sterol Homeostasis: Measuring 7-Dehydrocholesterol in Dhcr7-Deficient Neuro2a Cells and Human Fibroblasts. *J Med Chem* **59**, 1102-1115 (2016).
91. L. Xu *et al.*, An oxysterol biomarker for 7-dehydrocholesterol oxidation in cell/mouse models for Smith-Lemli-Opitz syndrome. *J Lipid Res* **52**, 1222-1233 (2011).
92. L. Xu, W. Liu, L. G. Sheflin, S. J. Fliesler, N. A. Porter, Novel oxysterols observed in tissues and fluids of AY9944-treated rats: a model for Smith-Lemli-Opitz syndrome. *J Lipid Res* **52**, 1810-1820 (2011).
93. L. Xu, L. G. Sheflin, N. A. Porter, S. J. Fliesler, 7-Dehydrocholesterol-derived oxysterols and retinal degeneration in a rat model of Smith-Lemli-Opitz syndrome. *Biochim Biophys Acta* **1821**, 877-883 (2012).
94. W. Liu *et al.*, A highly sensitive method for analysis of 7-dehydrocholesterol for the study of Smith-Lemli-Opitz syndrome. *J Lipid Res* **55**, 329-337 (2014).
95. G. K. Smyth, J. Michaud, H. S. Scott, Use of within-array replicate spots for assessing differential expression in microarray experiments. *Bioinformatics* **21**, 2067-2075 (2005).
96. M. D. Robinson, A. Oshlack, A scaling normalization method for differential expression analysis of RNA-seq data. *Genome Biol* **11**, R25 (2010).
97. R. Liu *et al.*, Why weight? Modelling sample and observational level variability improves power in RNA-seq analyses. *Nucleic Acids Res* **43**, e97 (2015).
98. M. E. Ritchie *et al.*, Empirical array quality weights in the analysis of microarray data. *BMC Bioinformatics* **7**, 261 (2006).
99. C. W. Law, Y. Chen, W. Shi, G. K. Smyth, voom: Precision weights unlock linear model analysis tools for RNA-seq read counts. *Genome Biol* **15**, R29 (2014).
100. C. L. Broadhead, D. Walker, R. Skinner, N. L. Simmons, Differential cytotoxicity of Ifosfamide and its metabolites in renal epithelial cell cultures. *Toxicol In Vitro* **12**, 209-217 (1998).
101. A. Khondker *et al.*, Membrane Cholesterol Reduces Polymyxin B Nephrotoxicity in Renal Membrane Analogs. *Biophys J* **113**, 2016-2028 (2017).
102. A. C. Johnson, L. B. Ware, J. Himmelfarb, R. A. Zager, HMG-CoA reductase activation and urinary pellet cholesterol elevations in acute kidney injury. *Clin J Am Soc Nephrol* **6**, 2108-2113 (2011).
103. K. Abdelraouf, K. T. Chang, T. Yin, M. Hu, V. H. Tam, Uptake of polymyxin B into renal cells. *Antimicrob Agents Chemother* **58**, 4200-4202 (2014).
104. S. K. Moestrup *et al.*, Evidence that epithelial glycoprotein 330/megalin mediates uptake of polybasic drugs. *J Clin Invest* **96**, 1404-1413 (1995).
105. N. D. Keirstead *et al.*, Early prediction of polymyxin-induced nephrotoxicity with next-generation urinary kidney injury biomarkers. *Toxicol Sci* **137**, 278-291 (2014).
106. Spero. (https://sperotherapeutics.com/pipeline/spr741-spr206-iv-potentiator-platform/).
107. M. Adler *et al.*, A Quantitative Approach to Screen for Nephrotoxic Compounds In Vitro. *J Am Soc Nephrol*, (2015).

108. S.-Y. Chang *et al.*, Human liver-kidney model elucidates the mechanisms of aristolochic acid nephrotoxicity. *JCI Insight* **2**, (2017).
109. D. Huh, G. A. Hamilton, D. E. Ingber, From 3D cell culture to organs-on-chips. *Trends Cell Biol* **21**, 745-754 (2011).
110. J. Yin, J. Wang, Renal drug transporters and their significance in drug-drug interactions. *Acta Pharm Sin B* **6**, 363-373 (2016).
111. M. A. Ferguson, V. S. Vaidya, J. V. Bonventre, Biomarkers of nephrotoxic acute kidney injury. *Toxicology* **245**, 182-193 (2008).
112. R. Bellomo, J. A. Kellum, R. Mehta, P. M. Palevsky, C. Ronco, Acute Dialysis Quality Initiative II: the Vicenza conference. *Current opinion in critical care* **8**, 505-508 (2002).
113. R. Bellomo *et al.*, Acute renal failure - definition, outcome measures, animal models, fluid therapy and information technology needs: the Second International Consensus Conference of the Acute Dialysis Quality Initiative (ADQI) Group. *Critical care* **8**, R204-212 (2004).
114. R. L. Mehta *et al.*, Acute Kidney Injury Network: report of an initiative to improve outcomes in acute kidney injury. *Critical care* **11**, R31 (2007).
115. A. Levin, P. E. Stevens, Summary of KDIGO 2012 CKD Guideline: behind the scenes, need for guidance, and a framework for moving forward. *Kidney Int* **85**, 49-61 (2014).
116. X. Zeng, G. M. McMahon, S. M. Brunelli, D. W. Bates, S. S. Waikar, Incidence, outcomes, and comparisons across definitions of AKI in hospitalized individuals. *Clin J Am Soc Nephrol* **9**, 12-20 (2014).
117. F. Fabrizi *et al.*, Acute tubular necrosis following interferon-based therapy for hepatitis C: case study with literature review. *Kidney Blood Press Res* **38**, 52-60 (2013).
118. J. K. Farry, C. D. Flombaum, S. Latcha, Long term renal toxicity of ifosfamide in adult patients--5 year data. *Eur J Cancer* **48**, 1326-1331 (2012).
119. R. Hirschberg, Renal complications from bisphosphonate treatment. *Curr Opin Support Palliat Care* **6**, 342-347 (2012).
120. M. Khan, L. M. Ortega, N. Bagwan, A. Nayer, Crystal-induced acute kidney injury due to ciprofloxacin. *J Nephropathol* **4**, 29-31 (2015).
121. S. D. Weisbord, M. Ramkumar, S. A. LaPidus, D. J. McBride, P. M. Palevsky, Functional renal artery obstruction following percutaneous kidney biopsy. *Nephrol Dial Transplant* **20**, 1274-1275 (2005).
122. A. Beebe, B. Seaworth, N. Patil, Rifampicin-induced nephrotoxicity in a tuberculosis patient. *Journal of Clinical Tuberculosis and Other Mycobacterial Diseases* **1**, 13-15 (2015).
123. S. T. Bird, M. Etminan, J. M. Brophy, A. G. Hartzema, J. A. Delaney, Risk of acute kidney injury associated with the use of fluoroquinolones. *CMAJ* **185**, E475-482 (2013).
124. A. Gupta, M. Biyani, A. Khaira, Vancomycin nephrotoxicity: myths and facts. *Neth J Med* **69**, 379-383 (2011).
125. M. H. Rigatto *et al.*, Risk factors for acute kidney injury (AKI) in patients treated with polymyxin B and influence of AKI on mortality: a multicentre prospective cohort study. *J Antimicrob Chemother* **70**, 1552-1557 (2015).
126. S. Waheed *et al.*, Proximal tubular dysfunction and kidney injury associated with tenofovir in HIV patients: a case series. *Clin Kidney J* **8**, 420-425 (2015).
127. J. V. Bonventre, V. S. Vaidya, R. Schmouder, P. Feig, F. Dieterle, Next-generation biomarkers for detecting kidney toxicity. *Nat Biotechnol* **28**, 436-440 (2010).
128. F. Dieterle *et al.*, Renal biomarker qualification submission: a dialog between the FDA-EMEA and Predictive Safety Testing Consortium. *Nat Biotechnol* **28**, 455-462 (2010).
129. J. A. Phillips *et al.*, Rat Urinary Osteopontin and Neutrophil Gelatinase-Associated Lipocalin Improve Certainty of Detecting Drug-Induced Kidney Injury. *Toxicol Sci* **151**, 214-223 (2016).

130. T. Ichimura *et al.*, Kidney injury molecule-1 (KIM-1), a putative epithelial cell adhesion molecule containing a novel immunoglobulin domain, is up-regulated in renal cells after injury. *J Biol Chem* **273**, 4135-4142 (1998).
131. V. S. Sabbisetti *et al.*, Novel assays for detection of urinary KIM-1 in mouse models of kidney injury. *Toxicol Sci* **131**, 13-25 (2013).
132. Q. H. Luo *et al.*, KIM-1 and NGAL as biomarkers of nephrotoxicity induced by gentamicin in rats. *Mol Cell Biochem* **397**, 53-60 (2014).
133. M. Zubowska, K. Wyka, W. Fendler, W. Mlynarski, B. Zalewska-Szewczyk, Interleukin 18 as a marker of chronic nephropathy in children after anticancer treatment. *Dis Markers* **35**, 811-818 (2013).
134. X. Lin, J. Yuan, Y. Zhao, Y. Zha, Urine interleukin-18 in prediction of acute kidney injury: a systemic review and meta-analysis. *J Nephrol* **28**, 7-16 (2015).
135. C. R. Parikh, D. G. Moledina, S. G. Coca, H. R. Thiessen-Philbrook, A. X. Garg, Application of new acute kidney injury biomarkers in human randomized controlled trials. *Kidney Int* **89**, 1372-1379 (2016).
136. J. Mishra, Identification of Neutrophil Gelatinase-Associated Lipocalin as a Novel Early Urinary Biomarker for Ischemic Renal Injury. *Journal of the American Society of Nephrology* **14**, 2534-2543 (2003).
137. J. Mishra *et al.*, Neutrophil gelatinase-associated lipocalin: a novel early urinary biomarker for cisplatin nephrotoxicity. *Am J Nephrol* **24**, 307-315 (2004).
138. E. Gacka, M. Zyczkowski, R. Bogacki, A. Paradysz, L. Hyla-Klekot, The Usefulness of Determining Neutrophil Gelatinase-Associated Lipocalin Concentration Excreted in the Urine in the Evaluation of Cyclosporine A Nephrotoxicity in Children with Nephrotic Syndrome. *Dis Markers* **2016**, 6872149 (2016).
139. T. L. Nickolas *et al.*, Diagnostic and prognostic stratification in the emergency department using urinary biomarkers of nephron damage: a multicenter prospective cohort study. *J Am Coll Cardiol* **59**, 246-255 (2012).
140. K. Matsui, A. Kamijo-Ikemorif, T. Sugaya, T. Yasuda, K. Kimura, Renal liver-type fatty acid binding protein (L-FABP) attenuates acute kidney injury in aristolochic acid nephrotoxicity. *Am J Pathol* **178**, 1021-1032 (2011).
141. E. Jablonowska, K. Wojcik, A. Piekarska, Urine liver-type fatty acid-binding protein and kidney injury molecule-1 in HIV-infected patients receiving combined antiretroviral treatment based on tenofovir. *AIDS Res Hum Retroviruses* **30**, 363-369 (2014).
142. K. Kashani, W. Cheungpasitporn, C. Ronco, Biomarkers of acute kidney injury: the pathway from discovery to clinical adoption. *Clin Chem Lab Med*, (2017).
143. A. Bihorac *et al.*, Validation of cell-cycle arrest biomarkers for acute kidney injury using clinical adjudication. *Am J Respir Crit Care Med* **189**, 932-939 (2014).
144. E. A. Hoste *et al.*, Derivation and validation of cutoffs for clinical use of cell cycle arrest biomarkers. *Nephrol Dial Transplant* **29**, 2054-2061 (2014).
145. B. Nayak *et al.*, Transcriptional and post-translational modulation of myo-inositol oxygenase by high glucose and related pathobiological stresses. *J Biol Chem* **286**, 27594-27611 (2011).
146. L. Sun, R. K. Dutta, P. Xie, Y. S. Kanwar, myo-Inositol Oxygenase Overexpression Accentuates Generation of Reactive Oxygen Species and Exacerbates Cellular Injury following High Glucose Ambience: A NEW MECHANISM RELEVANT TO THE PATHOGENESIS OF DIABETIC NEPHROPATHY. *J Biol Chem* **291**, 5688-5707 (2016).
147. R. K. Dutta *et al.*, Beneficial Effects of Myo-Inositol Oxygenase Deficiency in Cisplatin-Induced AKI. *J Am Soc Nephrol*, (2016).

148. J. P. Gaut *et al.*, Development of an immunoassay for the kidney-specific protein myo-inositol oxygenase, a potential biomarker of acute kidney injury. *Clin Chem* **60**, 747-757 (2014).
149. A. Loboda, M. Damulewicz, E. Pyza, A. Jozkowicz, J. Dulak, Role of Nrf2/HO-1 system in development, oxidative stress response and diseases: an evolutionarily conserved mechanism. *Cell Mol Life Sci* **73**, 3221-3247 (2016).
150. A. Agarwal, J. Balla, J. Alam, A. J. Croatt, K. A. Nath, Induction of heme oxygenase in toxic renal injury: A protective role in cisplatin nephrotoxicity in the rat. *Kidney International* **48**, 1298-1307 (1995).
151. R. A. Zager, A. C. Johnson, K. Becker, Plasma and urinary heme oxygenase-1 in AKI. *J Am Soc Nephrol* **23**, 1048-1057 (2012).
152. N. Wang *et al.*, Urinary microRNA-10a and microRNA-30d serve as novel, sensitive and specific biomarkers for kidney injury. *PLoS One* **7**, e51140 (2012).
153. K. Ramachandran *et al.*, Human miRNome profiling identifies microRNAs differentially present in the urine after kidney injury. *Clin Chem* **59**, 1742-1752 (2013).

VITAE

Elijah J. Weber was born in Albuquerque, NM. In 2012, he graduated with honors from the University of New Mexico holding a bachelors degree of Biochemistry. In 2012, he moved to Seattle, WA and entered the University of Washington – Department of Pharmaceutics Ph.D. program. He joined Dr. Edward J Kelly's lab to complete his Ph.D. and received a number of awards including various scientific conference presentation awards and the University of Washington School of Pharmacy graduate student leadership award.